CAAP Final Report

Date of Report: August 31, 2024

Recipient Organization: University of California Berkeley

Prepared for: *U.S. DOT Pipeline and Hazardous Materials Safety Administration*

Annual Period: From 9/1/2020 **to** 8/31/2024

Contract Number: 693JK32050007CAAP

Project Title: Distributed Strain Sensing for Pipeline Safety Against Fault Moving and Landslide

Prepared by: Kenichi Soga

Contact Information: soga@berkeley.edu

Contents

List of Figures

List of Tables

List of Acronyms

API	American Petroleum Institute.
BLEVE	Boiling Liquid Expanding Vapor Explosion.
BOTDR	Brillouin Optical Time Domain Reflectometry.
DFOS	Distributed Fiber Optic Sensing.
DSS	Distributed Strain Sensing.
DTS	Distributed Temperature Sensing.
FEM	Finite Element Method.
HDPE	High-Density Polyethylene.
LNG	Liquefied Natural Gas.
OSHA	Occupational Safety and Health Administration.
OTDR	Optical Time Domain Reflectometry.
PG&E	Pacific Gas and Electric Company.
PGD	Permanent Ground Deformation.
PHMSA	Pipeline and Hazardous Materials Safety Administration.
SNR	Signal-Noise Ratio.
UCB	University of California, Berkeley.

1 EXECUTIVE SUMMARY

1.1 Project Deliverables

- Task 1: Design
    - The finalized fiber optic sensor installation plan for a replaced L-shaped steel gas pipeline, including specifications for sensor type, sensor length, attachment method, and location, has been completed.
- Task 2: Laboratory Test
    - An HDPE pipe bending test was conducted in November 2020 to assess the adhesive material's efficacy for attaching fiber optic sensors to the pipeline.
    - A steel pipe four-point bending test was conducted to assess the effectiveness of the fiber optic cable type and attachment method in facilitating adequate strain transfer during pipe deformation. Additionally, the distributed strain of the pipe under given loads was studied and analyzed.
- Task 3: Field Deployment
    - In June 2022, three 400-foot-long fiber optic strain cables were installed on the replaced steel gas pipeline in Gilroy, CA using an attachment method validated by laboratory tests. Additionally, one 1000-foot-long fiber optic strain cable and one 1000-foot-long fiber optic temperature cable were installed in the trench to provide comprehensive information.
- Task 4: Field Data Analysis
    - Regular readings have been conducted by the UC Berkeley team since July 2022 to collect distributed strain data of the replaced steel gas pipeline, aiming to assess its status and integrity.
    - The collected distributed strain data was evaluated and analyzed, revealing no discernible strain resulting from potential geohazards such as fault movement or landslides for the replaced pipeline. Instead, the observed strain correlated with the thermal expansion and contraction of the steel pipeline in response to

temperature changes.

  - A guideline for long-term strain monitoring of pipeline using DSS has been proposed.

- Task 5: Numerical Simulation
  - The value of distributed strain in the pipeline under geohazards was investigated.
  - 3D continuum finite element modeling was conducted for the steel pipe four-point bending test to compare the results and to determine how boundary conditions affect the simulation outcomes.
  - 3D continuum finite element modeling was conducted for the steel gas pipeline crossing the fault zone, and the distributed strain under potential fault movements was studied.
  - 3D continuum finite element modeling was conducted for the long continuous pipeline to analyze the distributed strain under fault movements and to identify the deformation pattern. Various soil constitutive models, pipeline parameters, and fault movement patterns were studied to understand how these factors affect the distributed strain of the pipeline.
- Task 6: Commercialization Plan
  - The current global market size of Structural Health Monitoring has been identified and the market demand for DFOS has been assessed by participating in the national I-Crops program funded by the US National Science Foundation.
  - The interviews of 100+ stakeholders show that more data is not always beneficial without clear usage strategies. There is a need to develop and deploy DFOS technology in partnership with public and private agencies to enhance infrastructure management and predict life expectancy. The focus should be on providing low-cost, smart infrastructure solutions that integrate distributed sensing data for better decision-making.

- In September 2023, the research team received a commercialization project from the US National Science Foundation to develop a mass-producible, commercial-quality DFOS system for smart infrastructure monitoring. The project involves creating low-cost hardware, integrating cloud-based data processing, and demonstrating real-time engineering analysis. To support commercialization, the team will conduct workshops to engage stakeholders, compare tools, and develop training programs aimed at cultivating a skilled workforce to drive innovation in the construction and infrastructure sector.

1.2 Education Accomplishments (student engagement, outreach activities)

- Student engagement
  - Peter Hubbard (PhD., graduated in September 2022) – Performed laboratory and field tests, engaged in the planning of the field installation.
  - Andrew Yeskoo (PhD., graduated in December 2022) – Engaged in the planning of the field installation.
  - Tianchen Xu (PhD., expected to graduate in May 2025) – Engaged in the field installation and monthly data acquisition, conducted data analysis, performed finite element numerical modeling and simulations.
- PhD/Master thesis
  - Tianchen Xu (2025 expected) – Distributed strain sensing and data analysis of gas pipelines against fault moving and landslide
- Development of curriculums for university students
  - A new undergraduate/graduate course “Infrastructure Sensing and Modeling” started in Fall 2020. This course teaches the fundamentals of various sensing and modeling tools used for infrastructure engineering and present case studies. The trend in entrepreneurship for emerging technologies in infrastructure and smart cities industry is discussed.
- Training provided to personnel working on pipeline safety
  - The people involved in the new construction of a gas pipeline in Gilroy CA experienced the actual field deployment of distributed fiber optic strain and temperature sensors.

- Technology readiness level: list the projects students worked on that ended up commercialized and utilized in the industry and/or have advanced on the technology readiness level or transferred to the Core Research Program for demonstration and deployment.
    - Dr. Peter Hubbard works for FiberSense, which is an emerging company that utilize distributed fiber optic sensing technologies to deliver insights from object and event detection in noisy environments at massive scale. It provides comprehensive strike prevention for critical infrastructure, leading to more resilient and reliable utilities.
    - Dr. Andrew Yeskoo works for GeoComp, which is an established geotechnical instrumentation company. He is leading company's effort to provide distributed fiber optic sensing services.

1.3 Publications

- Journal/conference publications
    - None
- Conference presentations/posters/invited talks, etc.
    - Northern California Pipe Users Group (PUG) Annual Sharing Technologies Seminar, California, Keynote, Feb 2024
    - Fiber Optic Seismology USGS Powell Center Workshop, Fort Collins, CO, March 2024
    - Annual Fiber Optic Sensing Association (FOSA) meeting, Austin, TX, June 2023
    - Geo-Congress 2022, Charlotte, North Carolina, State of the art lecture, ASCE Geo-Institute, March 2022
    - The 27th International Conference on Optical Fiber Sensors, Alexandria, VA, Keynote lecture, August 2022

2 INTRODUCTION/BACKGROUND AND OBJECTIVES

2.1 Introduction

Many pipeline systems spread over large geographical areas, and they are typically buried underground to gain protection and support from the soil. However, these advantages are not without drawbacks. Since they traverse for hundreds of miles over terrain with varied environmental and geotechnical characteristics, it is not always possible to avoid passing through zones where permanent ground deformation (PGD) is likely to happen. Permanent ground-induced actions due to fault movements, landslides, or liquefaction-induced lateral spreading are responsible for the majority of earthquake-induced damages to oil and gas buried steel pipelines. Those deformations are applied to the pipeline in a quasi-static manner and are not necessarily associated with severe seismic shaking. The pipeline may be seriously deformed in a plastic manner, which in turn may lead to pipeline wall fracture and loss of containment.

O'Rourke et al. (1995) reported that the most probable failure modes for modern steel pipelines are due to PGD. The damage mechanism refers to non-recoverable soil movements that are caused by fault movements, lateral and upward ground movements, soil liquefaction-induced soil movements and landslide. Each source of ground movement will directly produce high lateral soil stresses to pipelines by excessive soil restraint. If the ground movement is sufficiently large, the stresses can cause a wide variety of failure mechanisms, including tensile failure, buckling, wrinkling and joint failure, as shown in Figure 1. Differential ground movements can instigate deformations that may impact serviceability requirements or prompt failure mechanisms that may exceed limit states.

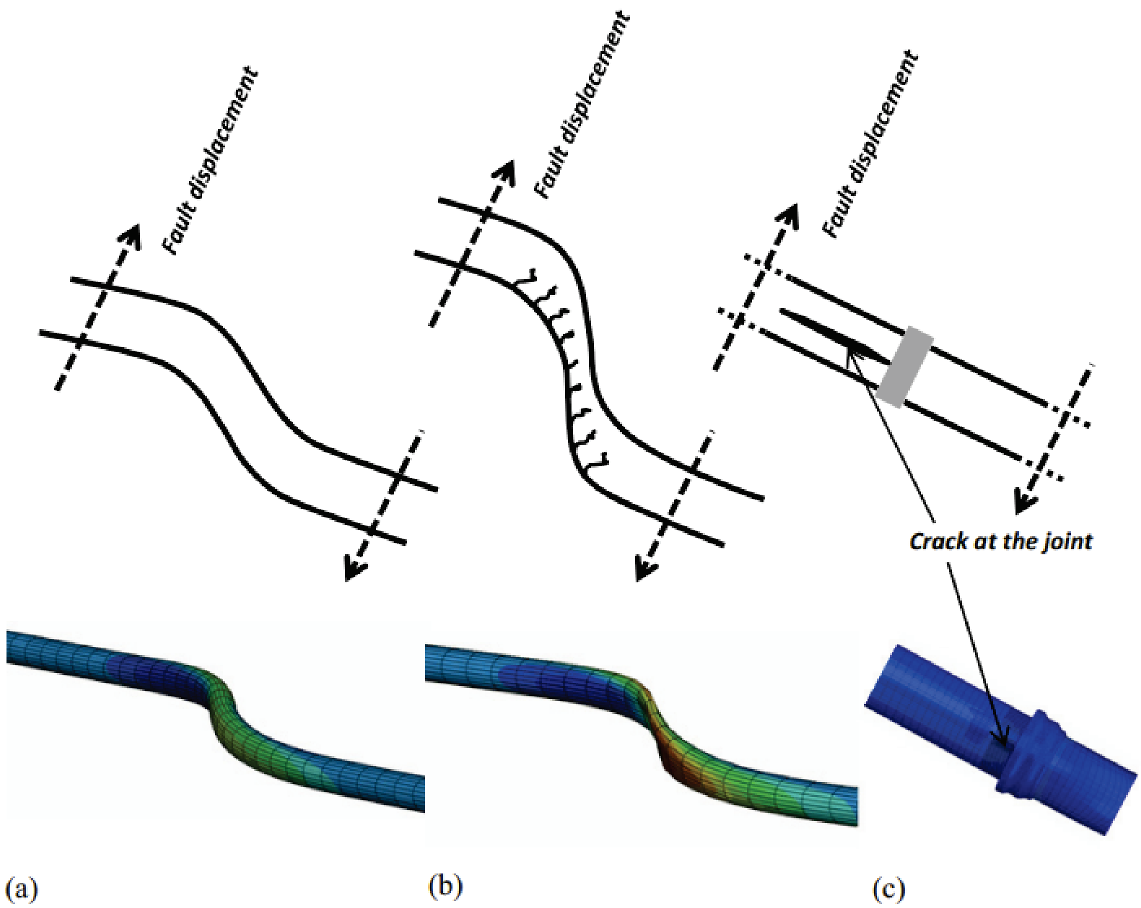

Figure 1: Failure modes of pipelines crossing a fault: (a) buckling failure; (b) wrinkling; (c) joint failure

The damage to pipelines caused by earthquake-induced fault movement can be disastrous. Examples of damage to the pipelines are shown in Figure 2. Damage to even a minor part of a pipeline can terminate the service of the entire pipeline. Figure 3 shows the route of gas transmission pipeline crossing the San Andreas fault at Cajon pass in Southern California, US. The fault movement can induce a failure of the pipeline causing an explosion when the overhead power transmission lines catch fire. An irrecoverable ecological disaster may also occur from the possible leakages of environmentally hazardous materials such as natural gas, fuel, or liquid waste that are conveyed by these pipelines. Severe distortions or ruptures of the pipeline will cause secondary impacts such as loss of serviceability and even cause severe problems to society, and particularly the pipeline operating companies, as vast amounts of money are lost due to the high repair costs and clean-up operations. Therefore, it is essential to evaluate the interaction forces between the pipeline and surrounding soils in order to prevent any failure or breakage of the pipeline.

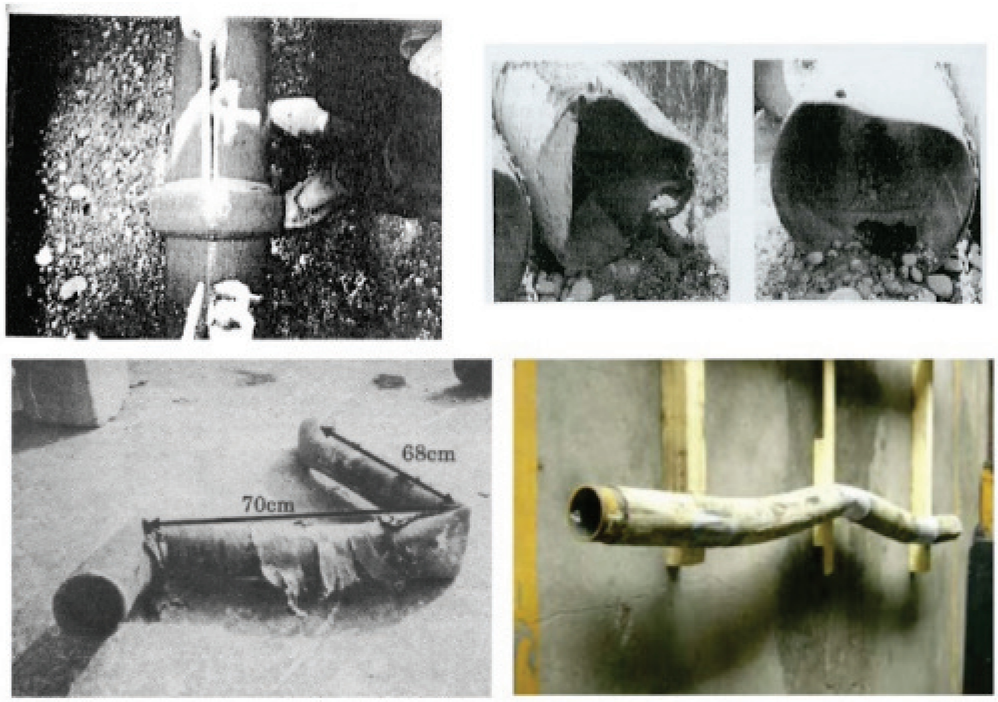

Figure 2: Failures of steel pipes crossing active faults from 1994 Sanriku Earthquake, Japan (Koseki et al., 1998), 1999 Chi-Chi Earthquake, Taiwan (Takada et al., 2001; Tokyo Gas), 2007 Niigataken Chuetsu-oki Earthquake, Japan (Tokyo Gas)

Figure 3: Pipelines crossing at San Andreas fault (Source: MMI Engineering Inc)

2.1.1 Distributed Fiber Optics Strain Sensing (DSS) Technology

Distributed fiber optic sensing (DFOS) is well adopted by the civil engineering and, oil and gas industry for strain, temperature and acoustic monitoring applications, as it is one of the emerging technologies that take measurements at the meter-to-kilometer scale (e.g. Bao & Chen, 2012; Soga et al., 2017; Soga & Luo, 2018). As shown in Figure 4(a), when a light wave travels through an optical fiber, it interacts with the constituent atoms and molecules, and the light is forced to deviate from a straight trajectory due to their non-uniformity. This deviation creates backscattering that brings a very small portion of the beam to go back to the source. When a fiber experiences a strain/temperature/vibration change, there is density fluctuation, which in turn changes the characteristics of the back-scattered beam. DFOS technologies use these changes in the recovered beam to quantify strain, temperature or vibration occurring along the standard optical fiber cable.

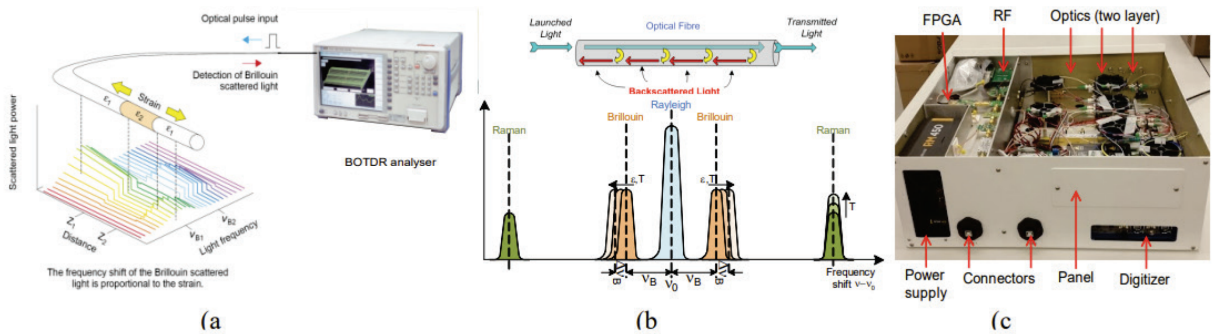

Figure 4: (a) Frequency-distance spectrum data recorded by a DFOS interrogator, (b) three scattering processes at a given point of a fiber. The changes are related to strain/temperature/vibration, (c) in-house built DFOS interrogator by UCB

There are three scattering processes: (i) Rayleigh, (ii) Brillouin, and (iii) Raman scattering, as shown in Figure 4(b). Rayleigh scattering propagates at the same frequency as the incident light and is mainly used for vibration monitoring (Zhang & Bao, 2008). Raman scattering has spectrum power levels that vary according to temperature changes (Darkin et al., 1985). Brillouin scattering is temperature and strain-dependent and the frequency shift of the Brillouin spectrum varies with longitudinal strain and temperature in a fiber (Ohno et al., 2001). The photon may lose energy and create phonon (Stokes mode) or gain energy by absorbing phonon (anti-Stokes mode). This leads to the frequency change of the scattered light, i.e. Brillouin scattering frequency shift. The distributed fiber optic strain sensing (DSS) technology utilizes the fact that the shift in Brillouin scattering frequency is proportional to the strain and temperature change:

$$\Delta v_b = K_\varepsilon^v \Delta\varepsilon + K_T^v \Delta T$$

where K_ε^v and K_T^v are the scattering frequency coefficient for strain and temperature changes, respectively.

The frequency change can be detected by reading the scattered spectrum at the launch end of the optical fiber. The spectrum is given by:

$$\int_{-\infty}^{+\infty} P_p(f) \frac{g_b(z)(\frac{\Delta v_b}{2})^2}{[v-(f-S_B(z))]^2+\frac{\Delta v_b}{2}^2} df$$

where S_B is the Brillouin frequency shift (around 11 GHz) and $S_B(z) = f - v_B(z)$, g_b is the Brillouin gain coefficient, Δv_b is the linewidth of the Brillouin scattering light and P_p is the power of the launched pulse light.

The novel aspect of this new Brillouin scattering based DSS technology (Brillouin Optical Time Domain Analyzer (BOTDA) or Brillouin Optical Time Domain Reflectometer (BOTDR)) lies in the fact that standard optical fiber becomes the sensor, and tens of miles of fiber can be sensed at once for continuous distributed measurement of the conditions around the optical fiber. The current state of the art DSS systems provide data in the micro-strain range with a spatial resolution (strain is averaged over a specified gauge length) of 0.2 m or less and a data interval of 0.02 m. This means that it is possible to have thousands of "strain gauges" along a single cable attached to the measurement object. Typical resolutions are 10 $\mu\varepsilon$ for strain. The cost of a standard optical fiber ($1-5/meter) is potentially very low compared to point measurement sensors.

With a conventional DSS interrogator, the measuring time to capture the strain/temperature profile is about 3 to 15 minutes, and therefore only the static change can be measured. One of the reasons is because conventional DSS systems use a frequency scanning method to obtain the Brillouin scattering frequency shift. The frequency scanning method moves the filter to detect the power in each frequency by searching the peak power frequency in the scattering spectrum. This operation makes the measurement progress slow. Another reason is the poor signal-noise ratio (SNR) of the Brillouin scattering signal. The poor SNR limits the dynamic performance of the DSS system. The newly developed DSS system by the PI research group can detect strain and temperature change dynamically by using small-gain Brillouin scattering to increase SNR and full spectrum analysis to save the frequency scanning time. 2 cm read-out, 2 m spatial resolution, 20 $\mu\varepsilon$ accuracy, and 23 Hz dynamic sampling rate can be achieved.

2.1.2 Laboratory Investigation of DSS Application to Pipeline Monitoring

The PI Soga and his research team have 15-years of experience using this DSS technology for infrastructure monitoring. Recent examples (Figure 5) include: (1) bridge foundation monitoring (Caltrans), (2) river levee monitoring (US Army Corps of Engineers), (3) construction induced ground settlement monitoring in San Francisco, and (4) gas well monitoring (LBNL/PGE). The team conducted DFOS installation on pipelines affected by fault crossings in collaboration with the East Bay Municipal Utility District in San Francisco Bay Area.

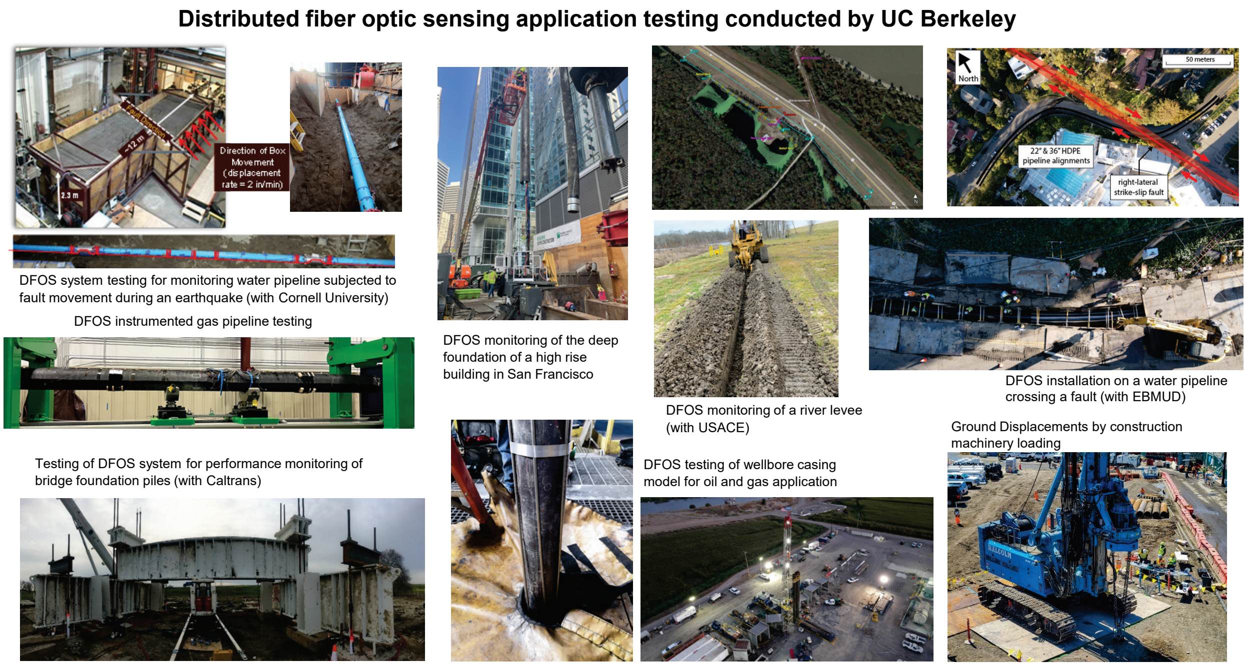

Figure 5: Examples of DSS field implementation by the PI Soga's research group

In 2016, the research team conducted a trial of DSS on pipeline subjected to fault rupture at Cornell University's Large-Scale Lifelines Testing Facility. The Full-scale rupture test included measurements of soil-pipeline interaction at various levels of rupture so that the performance of the water pipeline system, including the pipe and its hazard-resistant joints, can be evaluated under actual failure conditions. As shown in Figure 6(A), the pipeline test specimen consisted of three segments of polyvinylchloride thin-walled pipe that were connected by two bell-and-spigot joints spaced 6.1 m apart. The middle section was centered about the fault crossing. The ends of the north and south segments of the pipeline were fixed to test basin, representing worst-case boundary conditions. The pipe was buried in partially saturated sand that was compacted to give a strength similar to that of a medium dense to dense granular backfill. The instrumentation included: (a) metal foil strain gages, (b) fiber optic sensors, (c) string potentiometer to measure the opening of the joints, and (d) digital transducers to measure internal water pressure. A distributed fiber cable was installed along the spring-line and looped around the pipe to monitor the circumferential strains using the DSS system.

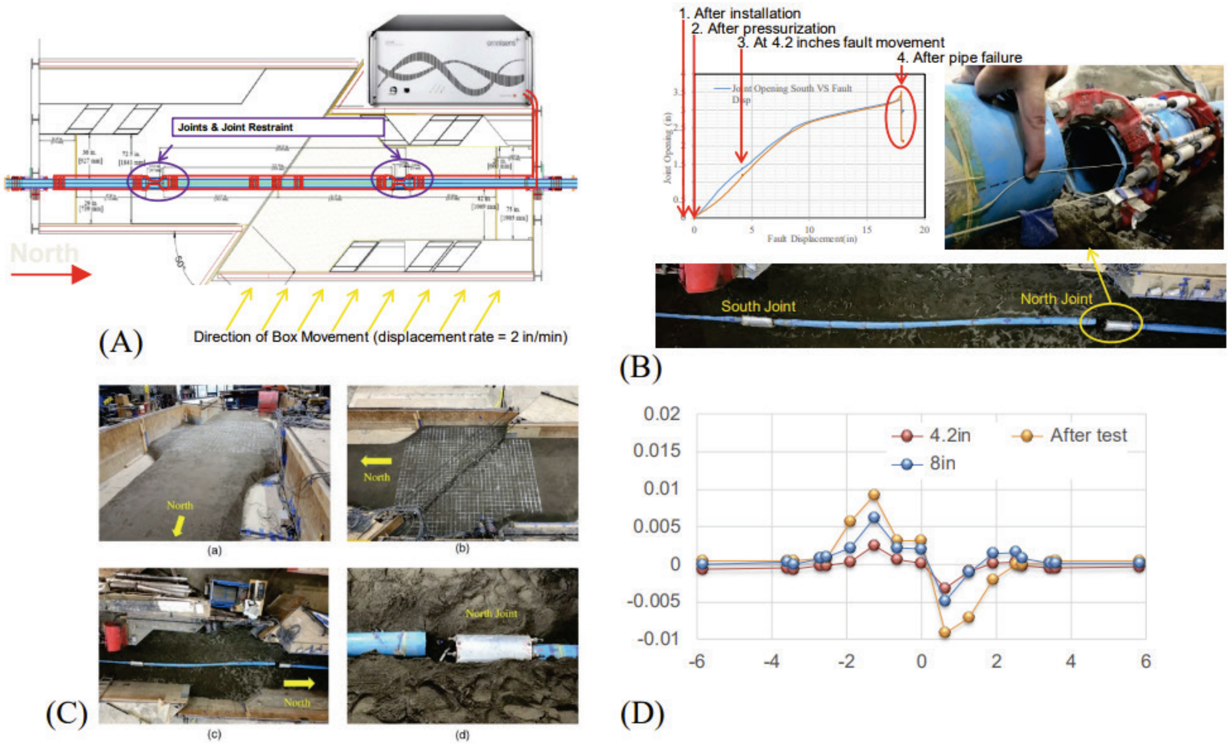

Figure 6: Trial testing of DSS on water pipeline affected by fault rupture in the soil tank

During the test, the southern part of the basin remained stationary while the northern section was displaced to the north and west by four large-stroke actuators to cause soil rupture and slippage at the interface between the basin's two parts. As shown in Figure 6(B), the soil rupture was representative of a left lateral strike-slip fault rupture, the most severe ground deformation that occurs along the margins of liquefaction-induced lateral spreads and landslides. Figure 6(C-a) shows the surface of the test basin before the test commenced. The north box was then displaced at a rate of 50 mm/min. At 455 mm of fault displacement, an audible pop sound was heard, the pipeline depressurized, and the test was stopped (Figure 6(C-b)). Figure 6(C-c) shows the deformed pipe as excavated following the test, along with breakage at its north joint. Figure 6(C-d) is a close-up of the north joint showing the protective joint shield and pipe rupture. Displacements of about 8.5 cm were measured at each joint just prior to a pipeline rupture. At a fault displacement of approximately 45 cm, i.e., when pipe failure occurred, all joint movements showed an abrupt jump in displacement due to elastic rebound. The north joint failure at its south restraint by circumferential rupture caused by the combination of elevated localized stress imposed by the restraint locking segments and the development of fault rupture–induced axial and bending strains along the pipe. As shown in the fiber optics strain data (Figure 6(D)), the pipeline reached strain levels near 1% prior to failure, and the response was consistent with performance observed during preliminary tension and bending tests (Wham et al., 2017).

2.1.3 Pipeline-Soil Interaction Analysis

Design methods to evaluate the soil forces imposed on buried pipelines when subjected to large ground movements are available (e.g., ASCE 1984). They rely on the work of various researchers (e.g., Hansen, 1961; Oversen, 1964; Audibert & Nyman, 1977; Rowe and Davis, 1982; Trautmann & O'Rourke, 1983&1985; Dickin, 1988), including the work of the PI Soga (Yimsiri et al., 2004; Cheung et al., 2011; Robert et al., 2016). Several researchers have proposed methodologies for analyzing a pipeline subjected to fault movements. Pioneering work was carried out by Newmark & Hall (1975), who proposed an approximate method for considering an underground pipeline that deforms in extension as a result of strike-slip fault displacement. This work was extended by Kennedy et al. (1977), who considered pipeline bending at constant curvature and nonuniform friction between the pipe and the surrounding soils. Several numerical studies have been performed in the past decade to investigate the effects of large soil deformation on the performance of buried pipes. Liu et al. (2008) and Vazouras et al. (2010) conducted numerical simulations to investigate pipeline responses under fault movements. Bryden et al. (2014) studied the soil–structure interaction of flexible pipes by using three-dimensional (3D) FE analysis and centrifuge tests, showing that pipe responses can be different from those in the avail-able analytical solutions. Design guidelines (e.g., ASCE 1984) recommend analyses of soil–pipe interactions by discrete springs specified in three directions (axial, horizontal, and vertical). However, the actual 3D soil-pipe interaction around the fault zone is more complicated than a simple spring–pipe interaction, in which the soil-spring model parameters at each direction are usually defined for two-dimensional (2D) conditions.

The PI Soga has 20-year experience in conducting 2D and 3D FE analyses of a soil-pipeline system to obtain the stress state and deformation of the pipe due to permanent ground deformation. For example, Figure 7(A) shows a numerical model of the large-scale soil–pipe interaction experiments carried out at Cornell University (O'Rourke et al., 2008). Isotropic 3D shell elements

(S4R) were used to model the pipe, whereas the soil was modeled with 3D solid continuum elements (C3D8R). The mesh density adopted for the soil box can be referred to as the intermediate mesh, in which finer meshes were concentrated at the pipeline locations; there are 2,160 elements for the pipe and approximately 35,000 elements for the soil. A critical state-based unsaturated Nor-Sand model developed by PI Soga (Fern et al., 2016) was adopted to model the soil behavior.

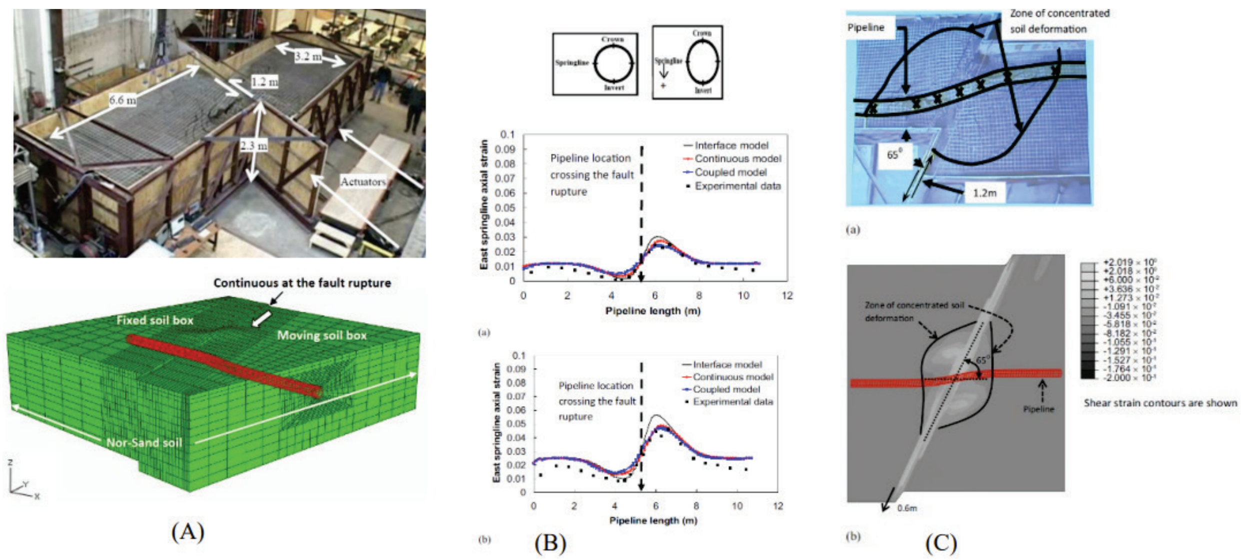

Figure 7: 3D FE modeling of soil-pipeline interaction during fault movement (Robert et al., 2016)

The computed axial strains at the east spring line are compared for the finite element simulations and the large-scale experimental results given in Figure 7(B) at different fault displacements. Figure 7(C) shows a schematic of the deformed shape of the test pipe, including the positioning directions. As the fault displacement increases, the pipe becomes elongated and bent, creating a spatial variation in strain. The maximum strain increases from the pipe end toward the center and peaks at the location of the ground ruptures.

To investigate the effect of pipe–fault-rupture inclination on the behavior of pipes, a series of parametric study simulations was also performed for dry soil and wet soil conditions. The analyses were performed on HDPE pipes (D=114.6 mm) buried at H/D (H is the burial depth) values of 2.0, 4.0, 5.74, 8.5, and 11.5, crossing lateral fault movements at inclinations (α) of 30°, 65°, and 90°. The values of nondimensional slope $\Delta\varepsilon/\Delta(d/D)$ (d is the fault displacement) are plotted against the fault-rupture inclinations in Figure 8(A). The results show that the dimensionless slope decreases with the increase in α for all H/D conditions because lower α leads to pipe stretching more in the axial direction to accommodate a given fault displacement. This is illustrated in Figure 8(B), which shows the plan view of ground deformations at two different fault inclinations. The same fault displacement, d, can cause more axial deformation of pipe in the α_2 model than in the α_2 model (i.e., $d \times \cos \alpha_2 \ > \ d \times \cos \alpha_1$ as $\alpha_1 > \alpha_2$). Hence, the α_2 model case is more critical than the α_1 model case. The results also show that pipes buried in wet soils are subjected to larger strain increases for rupture inclinations of $< 90°$ than those in dry sands, which is a result of the additional suction loading in wet sands. The deformed shapes of the pipelines are plotted in Figure 8(B) and show that a lower value leads to more localized strain induced by the soil deformation.

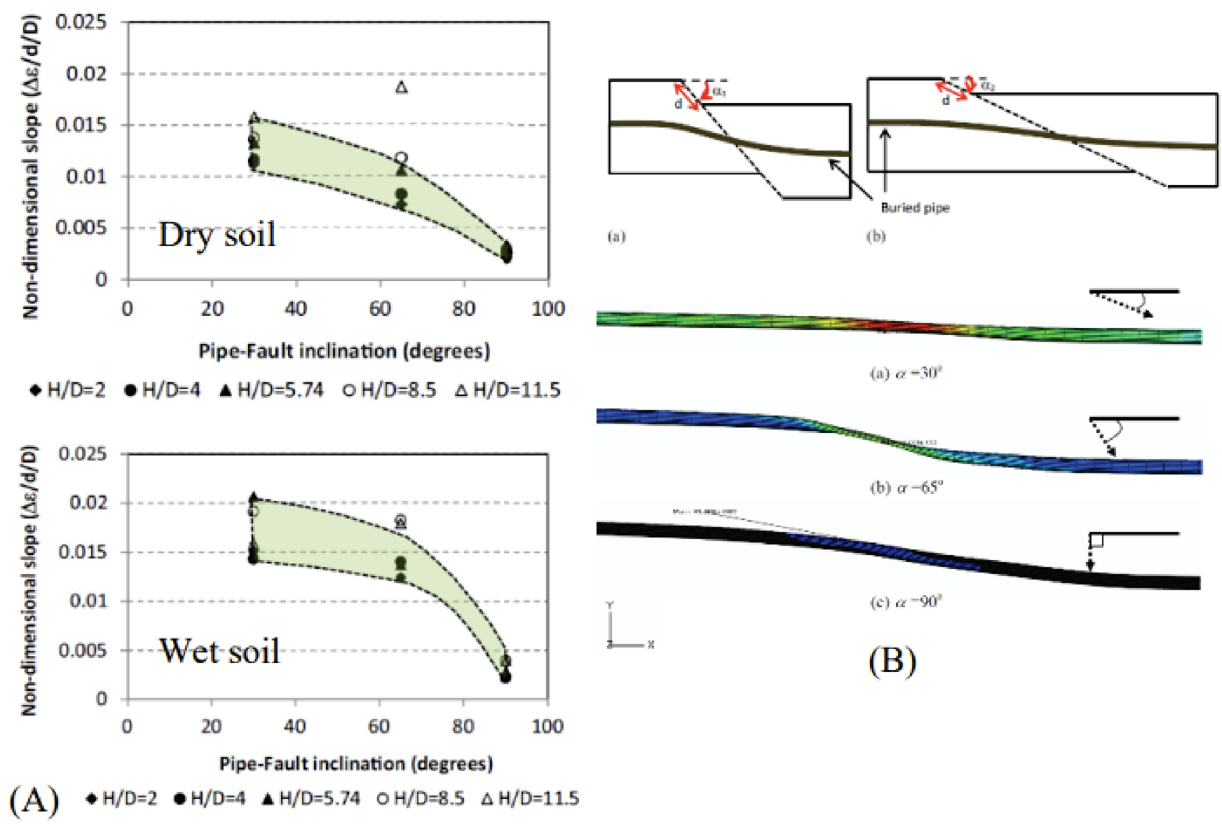

Figure 8: Normalized strain changes due to fault displacement and pipe deformation mechanisms for different fault angles (Robert et al., 2016)

2.2 Objectives

The general aim of the project is to examine the feasibility of a DSS system for long-term monitoring of buried gas pipelines that are potentially vulnerable to ground deformation across faults and landslides. Fiber optic material itself (silica-based) is relatively inert. Still, there is no currently available solution to ensure that the cable is firmly attached to a pipe for long-term pipe strain monitoring. Furthermore, the attachment of fiber optic cable to pipe is time-consuming. The specific objectives of the research are the following.

- To examine different fiber optic cable attachment methods for monitoring strain development within buried pipelines that are subjected to permanent ground movements. Laboratory experiments will be conducted and the applicability of the methods that satisfy PG&E's requirements will be investigated.
- To install fiber optic cables in the field to a pipeline that has potential for ground movements and conduct long-term monitoring of pipe strain development.
- To conduct 3D FE numerical modeling of the field problem in order to assess the strain values that are expected from ground movements and to compare them with field measurements.
- To examine the commercial value of the DSS system for monitoring pipelines that have permanent ground displacement risk.

3 EXPERIMENTAL PROGRAM

3.1 Laboratory Testing - Steel Pipe Four-Point Bending Test

The proposed fiber optic distributed strain sensing (DSS) system was tested for its ability to measure strain associated with pressurized steel pipeline bending by a full-scale laboratory test at ADV Integrity in Waller, TX. The purpose of the test was to evaluate the fiber optic cable type and attachment method for adequate strain transfer during pipe deformation.

The pipe was a 20-foot long, 12.75-inch diameter pipe made of grade X52 steel, with a wall thickness of 0.188 inches. The pipe had 6-inch-long steel caps welded on both ends to allow for pressurization. The pipe was instrumented with NZS-DSS-002 fiber optic cables manufactured by NANZEE Sensing Technologies. This cable consists of a fiber optic core surrounded by a tight buffer and wrapped within six helically wound steel braids. The cable has been used extensively in the civil engineering industry and has been proven to be robust enough to survive embedment into reinforced concrete, compacted soil, and even vibro-compacted hot-mix asphalt. The cable cross-section can be seen in Figure 9. The cables were oriented approximately 28° above and below the neutral axis, which in this case is the centerline of the pipe when viewed from the side.

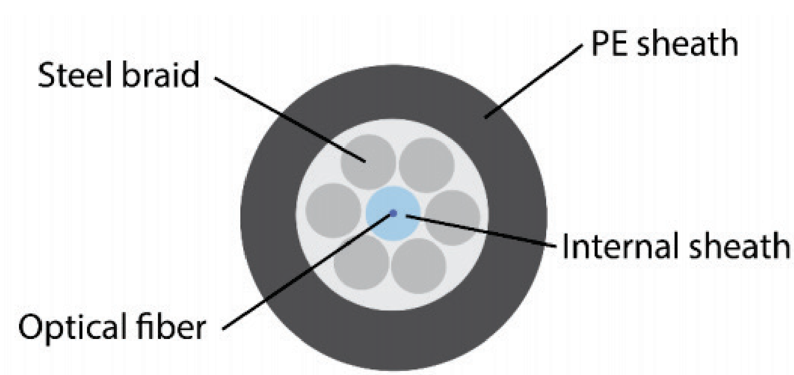

Figure 9: Cross-section of NZS-DSS-002 fiber optic cable

The cables were attached to the pipe using a three-stage process. First, the cables were epoxied to the pipe using 3M DP8010 structural plastic adhesive. The adhesive was applied using a pump applicator that laid a bead of adhesive adjacent to each sensing cable. Next, the adhesive was manually spread along the cable length to fill the meniscal space between the cable sheath and the pipe surface. The epoxy set for 10 minutes. Next, the pipe was wrapped helically with Trenton

Wax-Tape. This product provides an anti-corrosion barrier to the pipe and is a layer of protection for the fiber optic cable. The tape was applied by wrapping around the pipe and overlapping each successive pass by 1 inch. Finally, Trenton MCO outer wrap was applied on top of the Wax-Tape. This outer wrap was applied as specified by the manufacturer, with a 50% overlap of each successive pass. The wrap reacts to moisture in the air and cures into a hard shell surrounding the pipe and fiber optic cables. The fully instrumented pipe is shown in Figure 10.

Figure 10: Instrumented pipe in four-point bending apparatus

3.2 Field Testing

3.2.1 Pipeline Replacement Project

An L-shaped portion of the gas pipeline crosses a strand of faults in northern California, as shown in Figure 11. The company plans to replace the pipeline using a pipe with a larger thickness of 0.505 inches and 5L Grade X65 steel. As marked by the blue line, the re-routed segment, about 1300 ft, will cross the fault and pass through an active landslide zone. The east side and the west side of the pipeline are both hills where potential landslides would happen. The elevation of the hill on the east side is about 650 feet, and the elevation of the hill on the west side is 520 feet. The fault is in the direction of north to south. The 3D elbow section, as shown in Figure 12, will use API 5L Grade X60. A short transition section (shown in Figure 13) between the existing 0.344-

inch wall pipeline and the new 0.505-inch wall section will have an API 5L Grade X60 pipeline with a wall thickness of 0.406 inches.

The pipeline is exposed to some geohazard risks. These include (i) landslides and (ii) fault movements. The layout of the new pipeline and the potential fault movement zone as well as the landslide zone are shown Figure 11. The pipeline is surrounded by two major potential active landslide zones. The active landslide zone 1 may have a landslide from southwest to northeast. Regarding active landslide zone 2, potential landslides are expected from northeast to southwest. The fault crossing the east-west pipeline part may lead to a significant ground movement in the north-south direction.

Much of the information specific to the installation geometry, exact location, and geohazards is covered by NDAs between UCB and PG&E. However, items specific to the installation procedures planned by UCB may be disclosed to PHMSA.

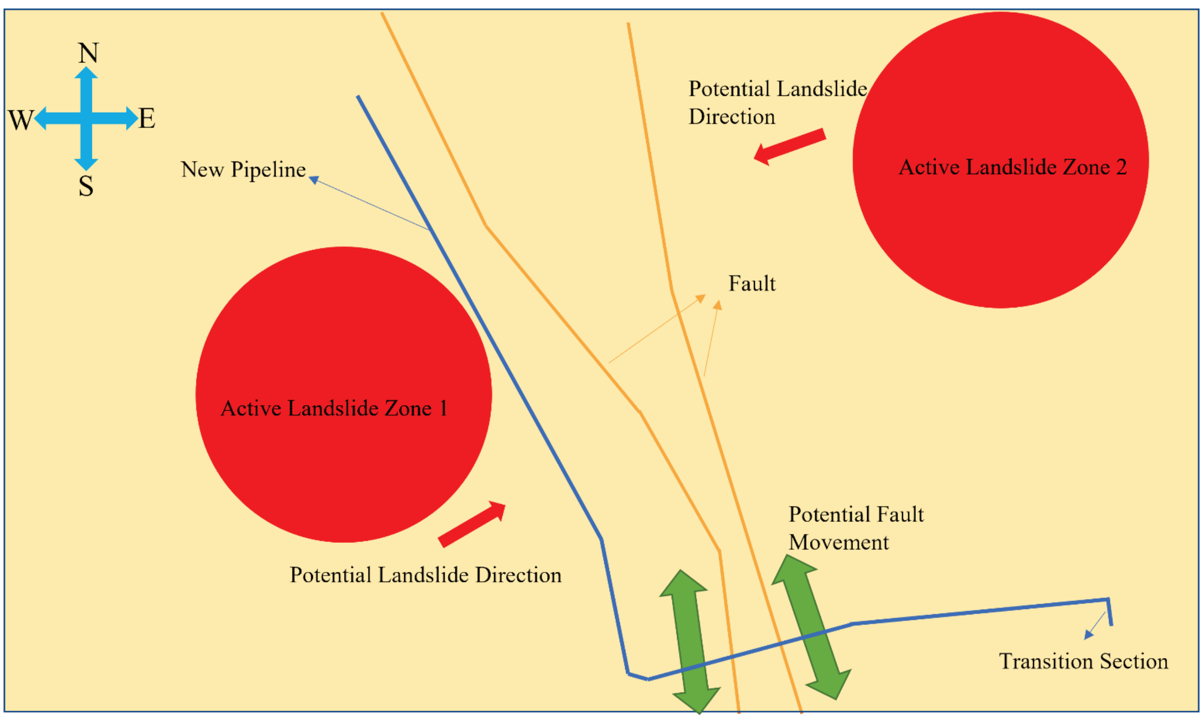

Figure 11: The layout plan of the new pipeline

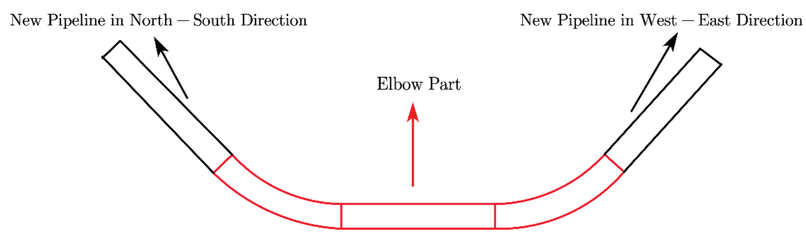

Figure 12: Elbow section of the new pipeline

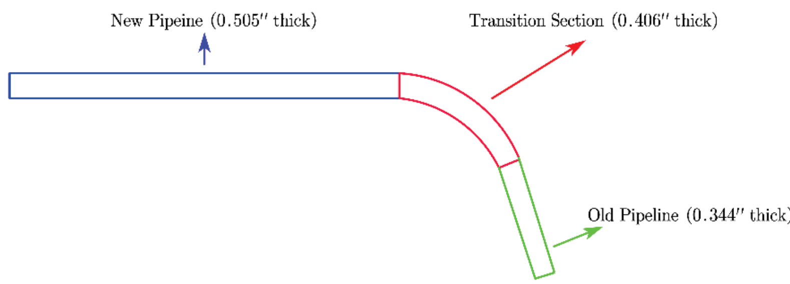

Figure 13: Short transition section of the pipeline

3.2.2 Task 1.1: Regular Meetings and Site Investigation

From 2020 to 2023, before the final installation of the fiber optic sensors, regular meetings were held between the UC Berkeley team, PG&E and the contractor. In the meetings, PG&E emphasized its requirement on the gas pipeline replacement work and contractor would update its replacement procedure. With this information, the UC Berkeley team kept modifying the installation design and plan to find the best way to install all the needed sensors without causing any potential issues which may bring safety issues. On November 3, 2021, the UC Berkeley team visited the site with the PG&E Team to discuss the installation plan with the landowner (shown in Figure 14). The locations and sizes of all the junction boxes, which are the above-ground part of the fiber optic monitoring systems for reading data, were confirmed with the landowner, and received approval. PG&E and the landowner also authorized access to this site for future periodical measurement. The working area is shown in Figure 14. The trees will be used as markers for instrumentation access boxes.

Figure 14: Photos of the site investigation

3.2.3 Task 1.2: Fiber Optic Sensor Selection

Based on the laboratory test results, it was decided to use NZS-DSS-C02 from NANZEE Sensing Inc. for the strain sensing cable, as shown in Figure 15. Adoption of metal funicular structure and sensing fiber high-strength metal reinforcement greatly improves the tensile strength of sensing fiber. The thread structure of the sensor makes good adhesion and deformation coordination.

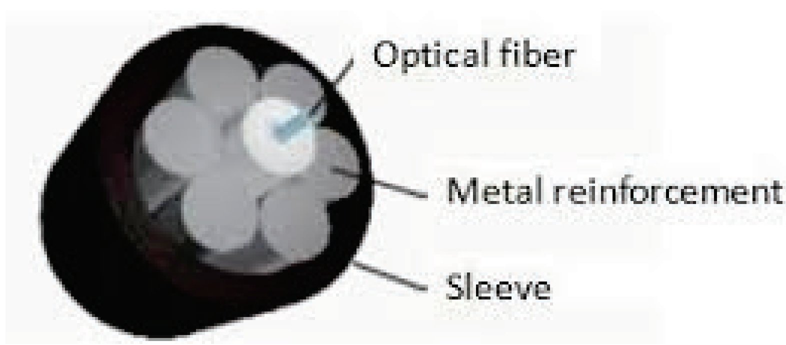

Figure 15: NANZEE strain cable

The temperature sensing cable would be BELDEN FSSC002N0 from Belden Inc., as shown in Figure 16. A polyethylene jacket is used to protect the center optical fiber, and gel is filled in the gaps to block water. The operation temperature of the Belden cable ranges from -40 ℃ to +70 ℃.

Figure 16: BELDEN temperature cable

3.2.4 Task 1.3 & Task 1.4: Fiber Optic Sensor Attachment and Installation Plan

The chosen method for attaching fiber optic sensors to pipelines involves the following steps.

Initially, duct tape is used to secure the fiber optic cables to the pipeline, with fixation points every 24 inches. Subsequently, adhesive (3M Scotch-Weld Acrylic Structural Plastic Adhesive DP8010 Blue) is continuously injected at the contact points between the fiber optic cables and the pipeline. The adhesive is then spread evenly using fingers to ensure thorough coverage. It is important to note that no aging tests were conducted to assess the long-term durability of the selected adhesive for extended monitoring purposes.

Once the adhesive has cured, the duct tape initially used for fixation is removed. Wax tapes (Trenton Wax Tape #2, 4" by 9', Anticorrosion wrap red) are then employed to further secure and protect the cable. To ensure a seamless transition from the wax tape to the pipeline, the edges of the wax tape are folded in.

The final step involves wrapping the pipeline with MCO outer wrap for additional protection. These wraps must be soaked in water prior to application to ensure maximum efficiency, and it is crucial to maintain an overlap rate exceeding 40% to guarantee optimal functionality.

This attachment method was not compared with other potential methods previously proposed. Due to the owner's safety regulations for field deployment, there was no other alternative option. It was initially tested in a laboratory setting (steel pipe four-point bending test) and demonstrated satisfactory deformation coordination results, leading to its subsequent use in field deployments.

The cables buried in the trench (marked in red in Figure 17) crossed both the fault zone and the potential landslide zone. The cross-section view of the updated fiber optic sensor installation plan is shown in Figure 18. Three 400-feet-long strain cables (marked in purple in Figure 17) were installed directly on the pipeline elbow section which crossed the fault zone to monitor the pipeline response under the fault movement. Two strain fiber optic cables and one temperature fiber optic cable were buried in the trench close to the new pipeline. To accurately measure strain, three strain cables were placed at specific angles along the pipeline - the crown, as well as at angles of +45° and -45° (see Figure 18). Each strain cable had a length of 400 feet. There are two welded locations along the monitored section: one at 220 ft and the other at 280 ft. At the 220 ft location, the sensing cable runs in the longitudinal direction, and the distributed strain data at this location, as well as the neighboring locations, will be useful for examining the performance of the welding during ground movement events. At the 280 ft location, two cables are spliced, so the measured data may not be of good quality compared to the data from the other location. In the designated trench, a single strain cable and a single temperature cable were laid, with each cable spanning 1000 feet. Four pull boxes were installed to connect all the fiber optic cables.

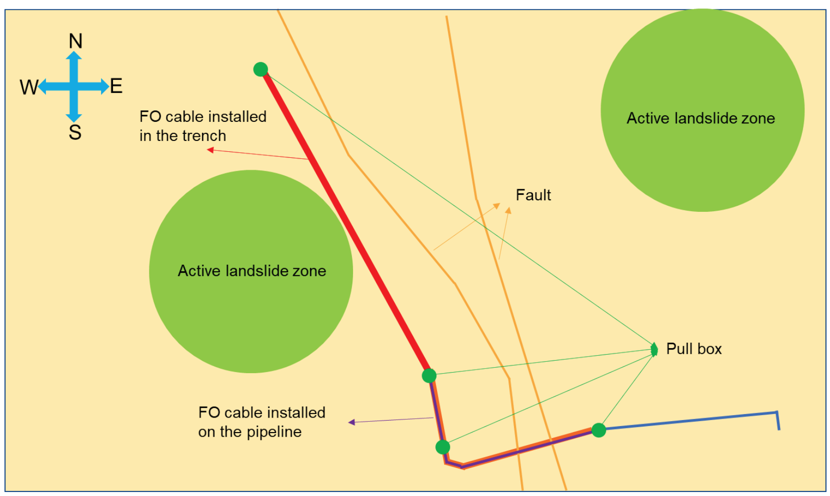

Figure 17: Fiber optic sensor installation plan

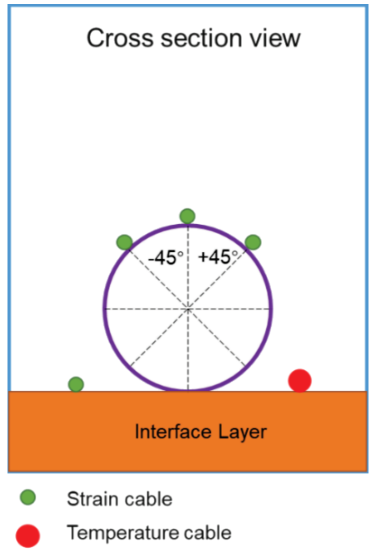

Figure 18: Cross-section view of UCB fiber optic sensor installation plan

3.2.5 Task 1.5: Fiber Optic Sensor Repair Strategies

To ensure the integrity of fiber optic sensors, we routinely employ Optical Time Domain Reflectometry (OTDR). Upon detecting any damage in the fiber optic cable, we utilize the length of the intact section indicated by the OTDR, along with the overall length of the fiber optic cable, to pinpoint the damaged area and proceed with the necessary repairs.

The most vulnerable component of the distributed fiber optic sensor is typically the splice points, where fiber optic cables are joined. As previously mentioned, these splicing points are housed in special protective boxes due to their fragility. We often include extra lengths of fiber optic cable at these points to facilitate future splicing. In the event of damage at these locations, we utilize the reserved extra length to create a new connection and restore the cable. If the damage involves the patch cable connecting the fiber optic cable to the analyzer, we replace the original patch cable with a new one by splicing it to the fiber optic cable to establish a new termination.

When the damage is not located at the ends, indicating that the fiber optic sensors installed along the pipeline are compromised, excavation of the corresponding buried section is required for further repair. If there is no visible damage to the outer protective layer of the cable, signal loss at a specific location may be attributed to high stress concentration. To alleviate this stress, we carefully manipulate the optical fiber or apply localized heat using a lighter or similar tool. If these methods fail or if there is visible damage to the cable, we cut out the damaged section and splice a new segment of fiber optic cable in its place.

After connecting both ends of the new cable segment to the original pipeline cable and ensuring that signal transmission is restored without significant loss, the repair is considered complete. We then apply protective measures to the repaired section, consistent with those used for other parts of the cable, and re-bury the cable.

By adhering to these procedures, we maintain the operational integrity and reliability of distributed fiber optic sensors.

4 RESULTS AND DISCUSSIONS

4.1 Task 2: Steel Pipe Four-Point Bending Test

After all attachment materials were applied and allowed to fully cure, the pipe was pressurized to 1106 psi and deformed by four-point bending. The apparatus is also shown in Figure 10. The test was strain-controlled, with foil strain gauges at the middle crown of the pipe being used for reference. The pipe was strained to a target level and then held there for 20 minutes so several DSS readings could be taken. The strain increments applied were 0.05%, 0.1%, 0.15%, 0.2%, 0.25%, 0.3%, 0.4%, 0.5%, 0.6%, 0.7%, 0.75%, 0.8%, 0.8%, 0.9%, and 1%. The pipe failed by local buckling at the north actuator. The final pipe condition is shown in Figure 19.

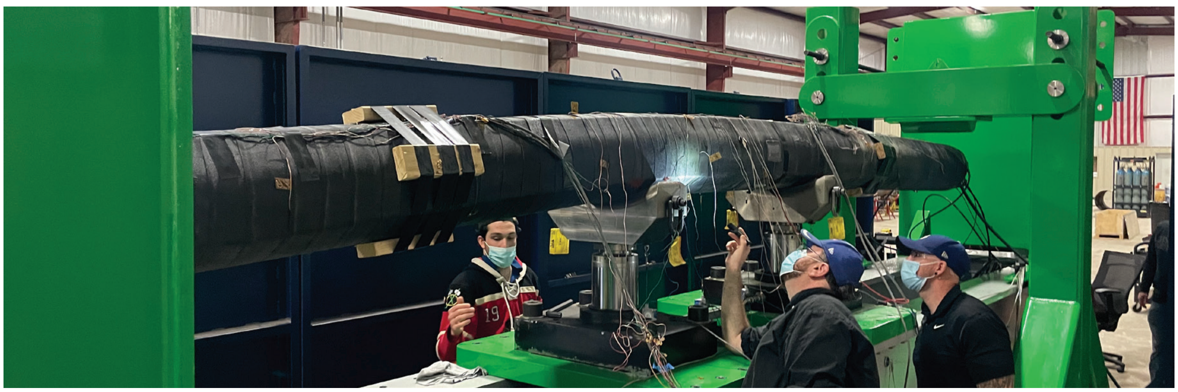

Figure 19: Deformed pipe after bending with North end showed in near field

The DSS system, cable selection and attachment method all behaved exceptionally well, for both the pressurization process and the bending test. Figure 20 and Figure 21 show the distributed strain data associated with the pressurization process and bending process, respectively. The pressurization process resulted in a consistent tensile strain increasing from zero to ~300 $\mu\varepsilon$ as measured with DSS. This agreed with the strain gauges observed on site. The strain measurements taken during the bending process show the behavior very comprehensively, including the local buckling at the north support. The strain values shown in Figure 21 are not equivalent to the control strain (listed in the legend) because the cables were not oriented at the extreme axis of bending. DSS measured approximately 50% of the expected strain when the pipe was behaving elastically (up to 0.15% control strain) which is expected for 28° offset from the neutral axis. As the pipe plasticized, the strains localized at yield locations. Eventually a wrinkle appeared at the north support. The DSS data shows an increase in tensile strain above the north support, and a decrease in compressive strain below it, which is indicative of buckling behavior.

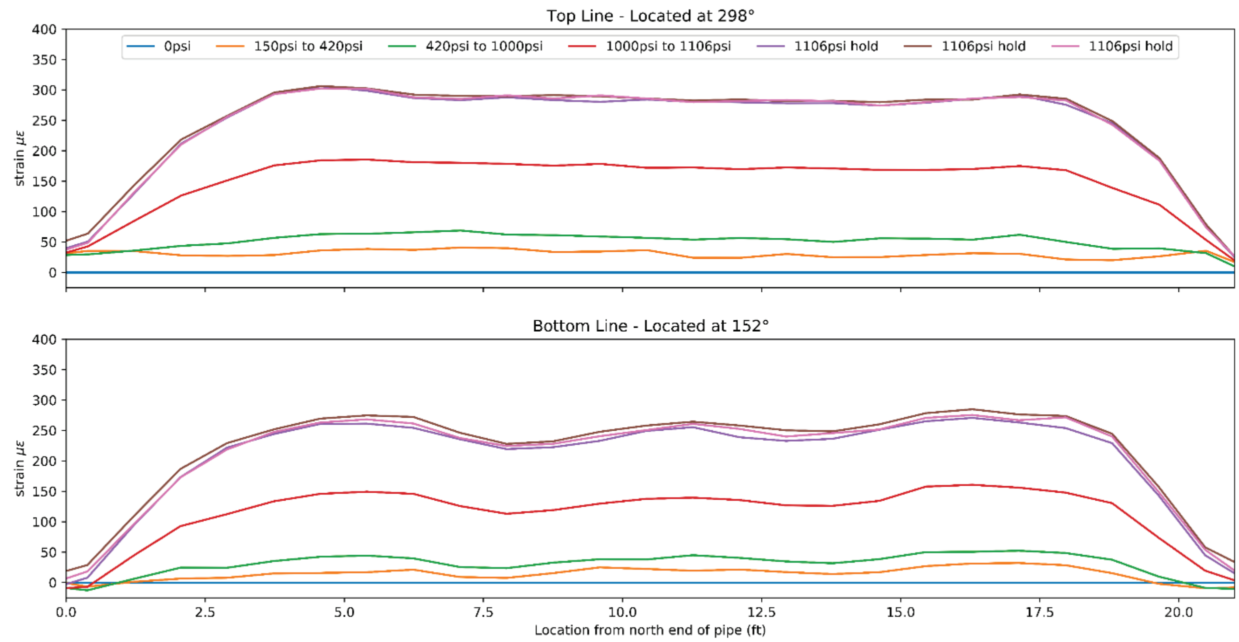

Figure 20: Strain profiles measured during pressurization to 1106 psi

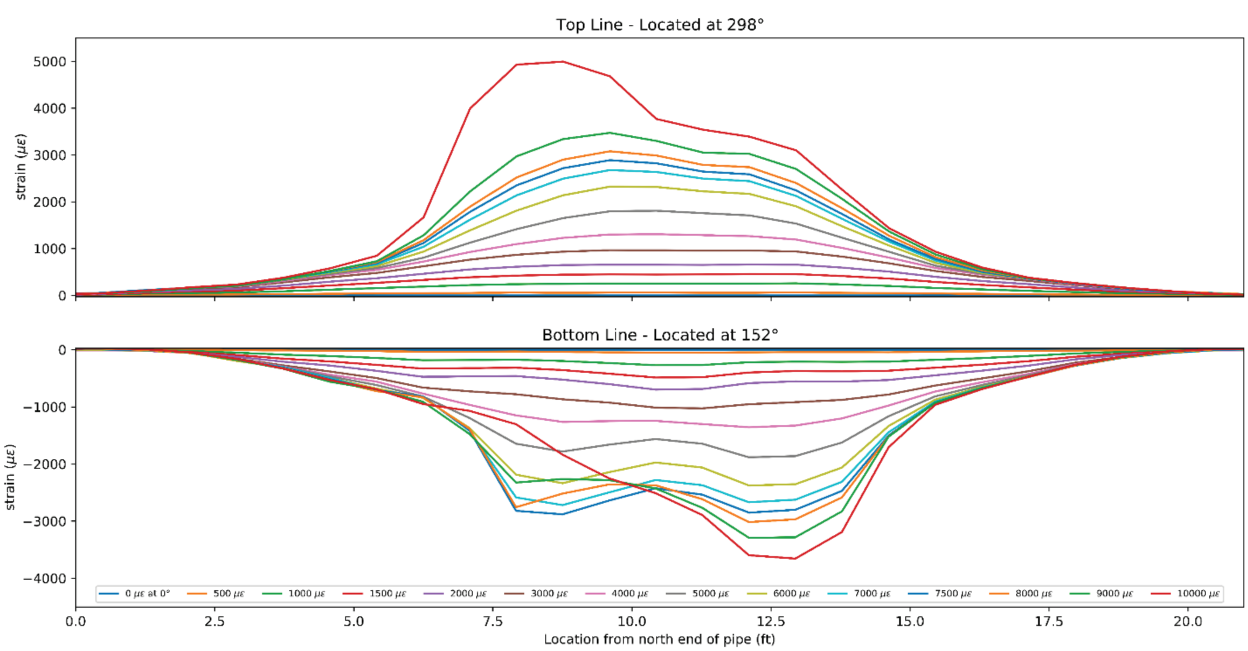

Figure 21: Strain profiles measured during bending

4.2 Task 3: Field Deployment

4.2.1 Fiber Optic Sensor Installation

4.2.1.1 Fiber Optic Sensor Installation inside Trench

As shown in Figure 22, the excavation of the new pipeline trench resulted in the installation of fiber optic cables within it, instead of being concealed as intended. The strain cable was installed on the -45° side, which is closer to the landslide location, while the fiber optic temperature cable was installed on the +45° side. To optimize the installation process, the cables were simultaneously installed from both ends of the trench. The contractor conducted regular inspections to check if the optical cable was aligned or had drifted from its designated position and adjusted using an elongated rod.

Figure 22: Fiber optic sensor installation in the trench

4.2.1.2 Fiber Optic Sensor Installation on Pipeline

Three different segments of the new gas pipeline were designated for the installation of fiber optic strain sensors. These segments included a 220-foot-long straight section from the east to west, a 60-foot-long elbow section, and a 120-foot-long straight section from the south to north (as shown in Figure 23). Following the pipeline welding and installation plan, the fiber optic cable for the first 220-foot-long segment was attached above ground prior to the segment's placement in the trench. After welding the segments and placing them in the trench, the attachment of the fiber optic cable to the elbow segment and the final 120-foot-long segment was completed below ground level.

To allow for future splicing, an additional 20 feet of length was added to both ends of each segment.

Figure 23: Photos of (a) 220-foot-long straight segment; (b) 60-foot-long elbow segment

The pipes scuffed with fine grain sandpaper before attaching the fiber optic cable. After that, the pipeline was cleansed with alcohol. To attach the cable, the crown and -45° and 45° positions along the length of the pipeline were marked. The 3M Scotch-Weld Acrylic Structural Plastic Adhesive DP8010 Blue was used to fix the fiber optic cables to the steel pipeline. Initially, the adhesive was applied onto the surface using the adhesive gun, then the fiber was positioned onto the adhesive. The cable was temporarily fixed every 24 inches with ductile tapes until the adhesive cured. Finally, the adhesive was evenly distributed by manual application using hands. Figure 24 shows how the contactor applied the adhesive to the surface of the pipeline.

Figure 24: Adhesive material application

After the adhesive had cured (usually about 2 hours after being sealed in), wax tapes (specifically, Trenton Wax Tape #2, 4" by 9', Anticorrosion wrap red) were used for fixation and protection. The ductile tapes were removed first before the wax tape was applied. To achieve a more seamless transition from the wax tape to the pipeline, the margins of the wax tape were folded in, as shown in Figure 25. Figure 26 shows the installation process of the wax tape including the folded shape.

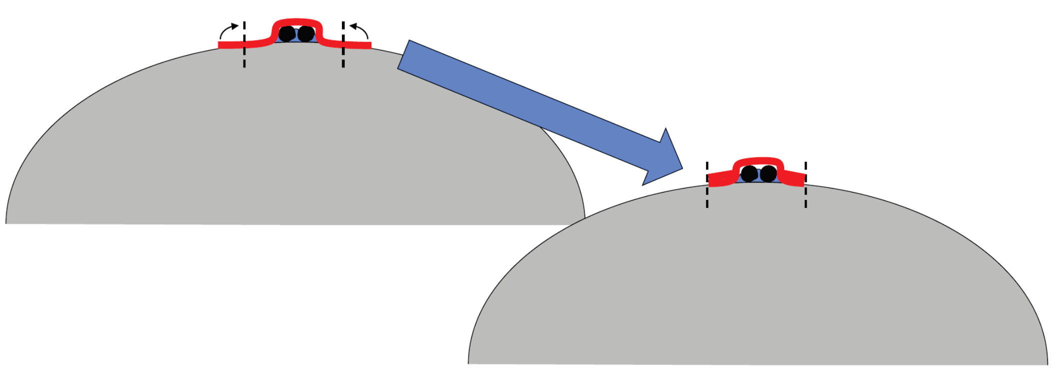

Figure 25: Wax tape folding process

Figure 26: Wax tape application

After applying wax tapes, the MCO outer wrap was wrapped around the pipe. Before the application, the wraps were soaked in water to ensure maximum efficiency. It was important to note that the overlap rate must exceed 40% to guarantee optimal functionality. However, in certain areas of the pipeline, the wrap could not be applied due to the support provided underneath them, as shown in Figure 27. Therefore, the contractor had to elevate the entire pipeline to secure the wrap in those specific areas once the wrap was completed in all other locations. After the necessary tasks were completed, the entire pipeline was carefully repositioned within the trench.

Figure 27: Outer wrap application

After completing all the required attachment tasks, the contractor verified that the pipeline was placed correctly underground. Once the fiber optic sensors were installed in the trench, the entire area underwent backfilling and compaction.

4.2.1.3 Pull Box Installation and Splicing

On July 16, 2023, four pull boxes were installed to splice concrete following backfilling and compaction. Two of the pull boxes located at Location +400 and Location +675 utilized the Coyote In-Line Runt Closure, which is hermetically sealed, to safeguard the splicing component due to the intersection of both fiber optic cables present in the trench and on the pipeline at this specific location. Plastic tubes were used to protect the splicing component in the final two pull boxes situated at Location +800 and Location +1400 due to the reduced number of cables present. By splicing the fiber optic cables, a single loop was formed, with the sequence consisting of the following: the strain cable at an angle of +45°, the strain cable at the crown, the strain the cable at an angle of -45°, the strain cable in the trench, and the temperature cable in the trench. Figure 28 and Figure 29 show illustrations of the process.

Figure 28: Pull box installation

Figure 29: Splicing in the enclosure

Upon completion of the splicing tasks, as shown in Figure 30, three steel plates were affixed as protective covers for each pull box, effectively safeguarding the entirety of the above-ground fiber optic cables.

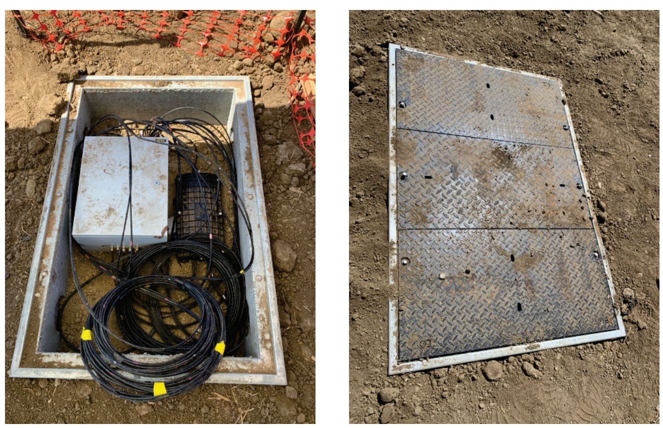

Figure 30: Pull box after all work is completed

4.2.2 Measurement Activity

The UCB team initiated the baseline reading on July 26, 2023. Following this, on August 16, 2023, they conducted another measurement to ascertain the fluctuation in strain and temperature over the specified period to carry out the precision error analysis. Subsequently, starting from October 2023, monthly readings were consistently taken to compile strain and temperature data of the monitored pipeline, facilitating ongoing assessment of its condition. The dates corresponding to all these readings are shown in Table 1.

Table 1: Summary of reading activities

Reading	Date
1	07/26/2023
2	08/16/2023
3	10/10/2023
4	11/22/2023
5	01/11/2024
6	02/15/2024
7	03/14/2024
8	04/10/2024
9	05/15/2024

All the readings were taken at noon using the BOTDR analyzer developed by the research group. To ensure accurate measurement readings, it is customary to cover the instrument with a tent or house it under a vehicle to reduce the impact of elevated temperatures on the instrument's measurement capabilities. The analyzer and the setup of all the instruments during the data collection is shown in Figure 31.

Figure 31: Data collection using self-developed instruments

4.3 Task 4: Field Data Analysis

4.3.1 Precision Error Evaluation

The precision error of BOTDR/BOTDA systems has a significant impact on the measurement repeatability of strain and temperature magnitude, as well as their corresponding locations. Precision error is the statistical variance of multiple repeatability measurements taken at each measured site along the sensing cable. To ensure accurate measurements, readings are obtained using the same instrument and operator, with consistent loading circumstances. The calculation involves determining the standard deviation of a set of numerous readings, often ranging from 30 to 100 readings. It is also possible to determine the spatial distribution of the standard deviation along the sensor fiber.

On August 16, 2023, the UCB team conducted a total of twelve readings over a period of two hours to obtain the necessary data for conducting a precision error evaluation. Despite the limited readings, the subsequent data illustrates the successful implementation of strain sensing cables on the pipeline, as shown in Figure 32. It is evident that the precision error for sensing cables put at the crown, at +45° and -45° positions, exhibits a range of approximately 5-10 $\mu\varepsilon$ across the entirety of the cable's length in most spots. Nevertheless, certain points on the crown cable exhibit a notable accuracy mistake ranging from 20 to 30 $\mu\varepsilon$. As shown in Figure 33, it is evident from the preceding analysis that these particular spots represent locations characterized by sudden changes in strain, indicating that the strain gradients at these spots are quite substantial. The aforementioned factor significantly influences the precision of the produced measurements.

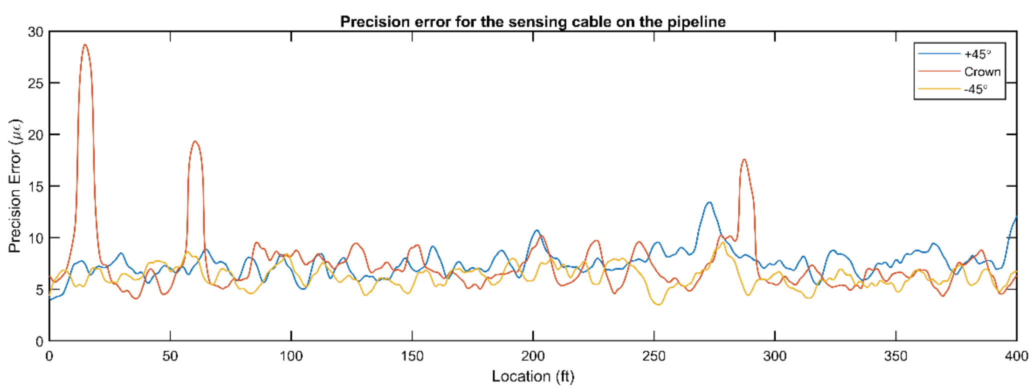

Figure 32: Precision error of the pipeline measurement

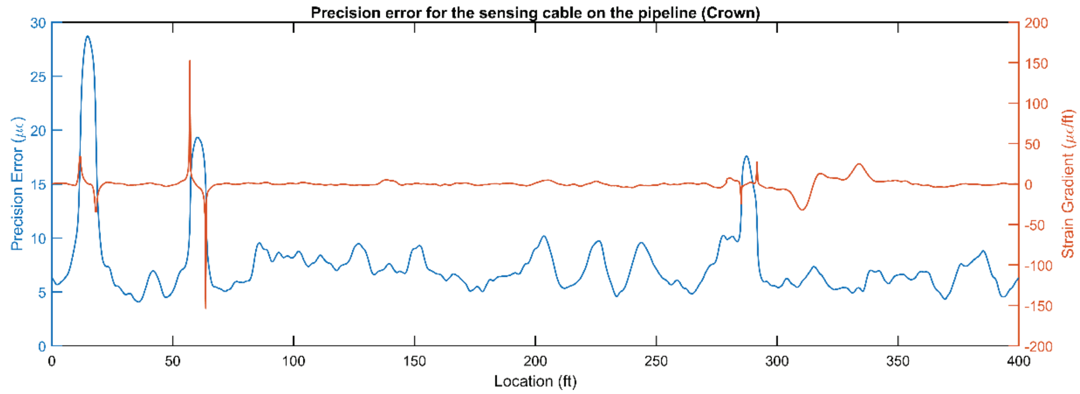

Figure 33: Precision error and strain gradient along the pipeline crown

The identical investigation was likewise conducted on the sensing fiber located within the trench. As depicted in Figure 34, the precision error of the measurements falls within the range of 6 to 10 $\mu\varepsilon$. The upper limit of precision error is around 16 $\mu\varepsilon$.

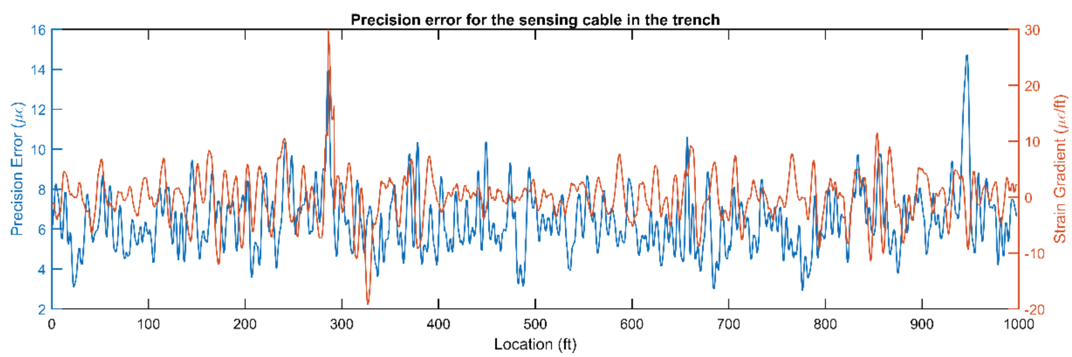

Figure 34: Precision error and strain gradient in the trench

4.3.2 Temperature Change in the Trench

The measured temperature changes from the fiber optic sensor buried in the trench are shown in Figure 35. As indicated, the temperature change distribution between each pair of readings exhibits relatively small fluctuations, with differences usually less than 4°F along the 1000-foot length. However, at specific locations, such as at 300 feet and 700 feet, there are significant temperature changes.

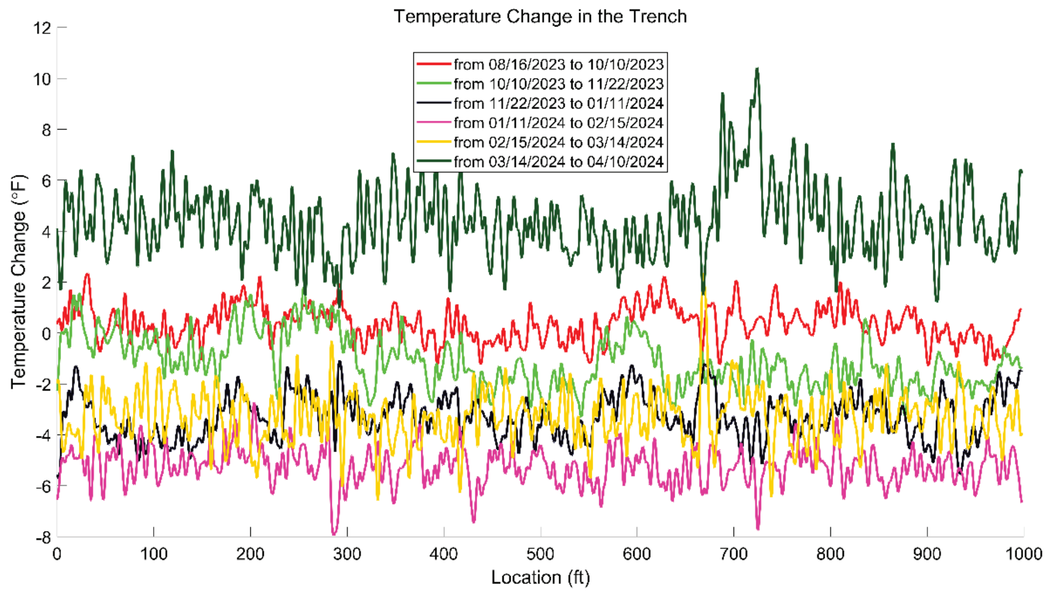

Figure 35: Temperature change in the trench

The average temperature change along the 1000-foot length is compared with the Gilroy weather data, as shown in Table 2. The table reveals a consistent trend: when the meteorological temperature decreases, the soil temperature also decreases, and when the meteorological temperature increases, the soil temperature similarly rises. However, the magnitude of temperature change in the soil is typically smaller than that observed in the air data.

From January to February 2024, significant rainfall occurred, which also affected the temperature inside the soil. Additionally, vegetation can make a considerable difference. During and immediately after construction, the soil was exposed and had better contact with sunlight, influencing its temperature. Starting in March 2024, as plants began to grow, they provided effective shading, which reduced temperature fluctuations within the trench.

Table 2: Temperature change comparison

Time	Measured Temperature Change (°F)	Temperature Change from Weather Data (°F)
from 08/16/2023 to 10/10/2023	0.4	-4
from 10/10/2023 to 11/22/2023	-1.1	-1

from 11/22/2023 to 01/11/2024	-3.3	-8
from 01/11/2024 to 02/15/2024	-5.2	-6
from 02/15/2024 to 03/14/2024	-3.3	3
from 03/14/2024 to 04/10/2024	4.4	9

It is worth noting that this temperature fiber is not installed directly on the pipeline but is instead buried in the soil. Due to the differing thermal properties of soil and the pipeline, the measured temperature changes may slightly deviate from those of the pipeline itself. Additionally, the absence of direct installation on the pipeline means that no direct comparative data is available.

The primary benefit of installing the temperature fiber directly in the soil is cost savings. Since the use of adhesive, wax tape, and outer wrap materials is relatively expensive, installing the fiber in the soil only incurs labor costs. This approach can significantly reduce expenses for monitoring long-distance pipelines.

4.3.3 Strain Change of the Pipeline at the +45° Location

Figure 36 shows the variation in strain change between successive readings at the +45° location of the gas pipeline. Figure 37 illustrates the cumulative strain changes observed from August 2023 onwards. Month-to-month strain changes are small, typically within 100 $\mu\varepsilon$. A decrease in temperature corresponds to compressive strain in the pipeline, presumably attributed to the contraction of the steel material. However, despite a significant temperature drop in the soil from January 2024 to February 2024, the resultant strain change is marginally smaller compared to previous months. Additionally, certain locations exhibit minor tensile strain.

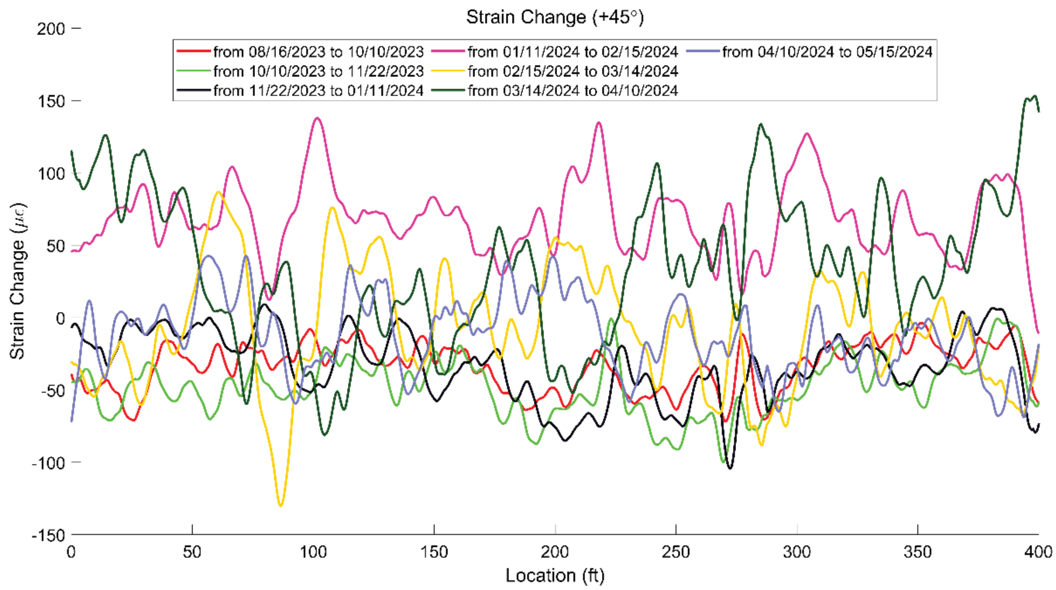

Figure 36: Strain change between each reading (+45°)

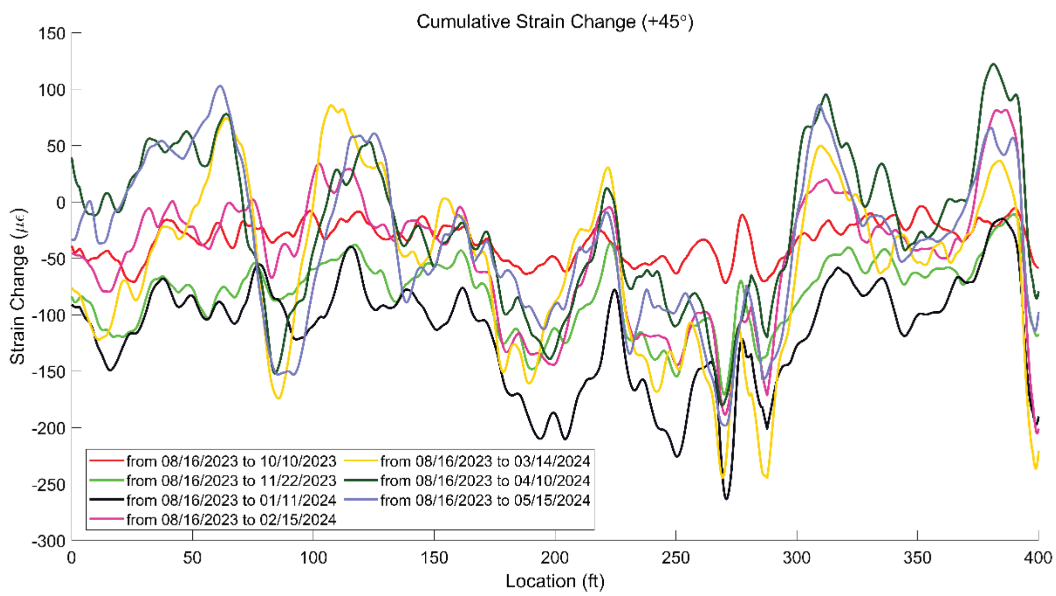

Figure 37: Cumulative strain change (+45°)

While the temperature decline typically induces steel pipeline contraction, the occurrence of rainfall during this period saturates the soil, increasing hydrostatic forces. Consequently, the soil exerts additional pressure on the pipeline, potentially leading to lateral forces and elongation in the pipeline axial direction. This dual influence of thermal contraction and soil saturation potentially manifests in a strain distribution characterized by predominantly compressive strain with isolated instances of minor tension.

4.3.4 Strain Change of the Pipeline at the Crown Location

Figure 38 illustrates a similar pattern in terms of the monthly strain changes observed at the crown of the gas pipeline. Figure 39 shows the cumulative strain change at this particular position. Unlike the readings preceding January 2024, which primarily indicated small compressive strain in the pipeline, measurements from January 2024 to February 2024 reveal both compressive and tensile strain. Despite a more pronounced temperature drop in the soil during this period, the level of compressive strain remains comparable to that of the preceding months. This suggests that thermal contraction may not be the sole dominant factor influencing pipeline strain, implicating the role of rainfall-induced soil saturation. The gradual saturation of the soil by rainfall during this period emerges as a significant contributor to pipeline strain. Compared to the +45° location, there is a larger strain fluctuation at the crown. Along the 400-foot length, the strain difference ranges from 50 $\mu\varepsilon$ to 100 $\mu\varepsilon$. This indicates that the crown experiences more significant strain variations, highlighting the need for careful monitoring and analysis at this critical point in the trench.

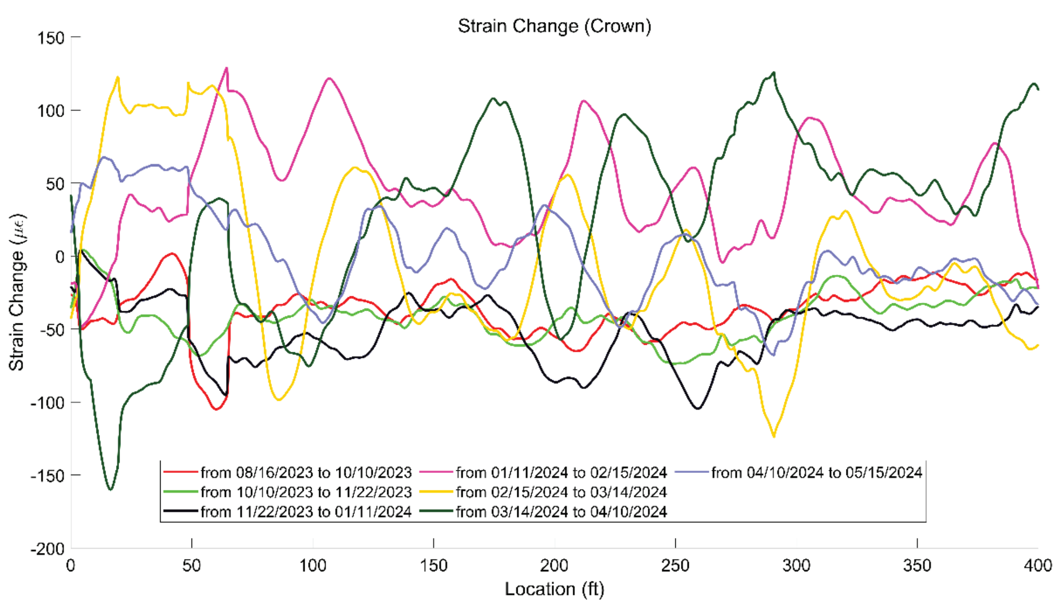

Figure 38: Strain change between each reading (crown)

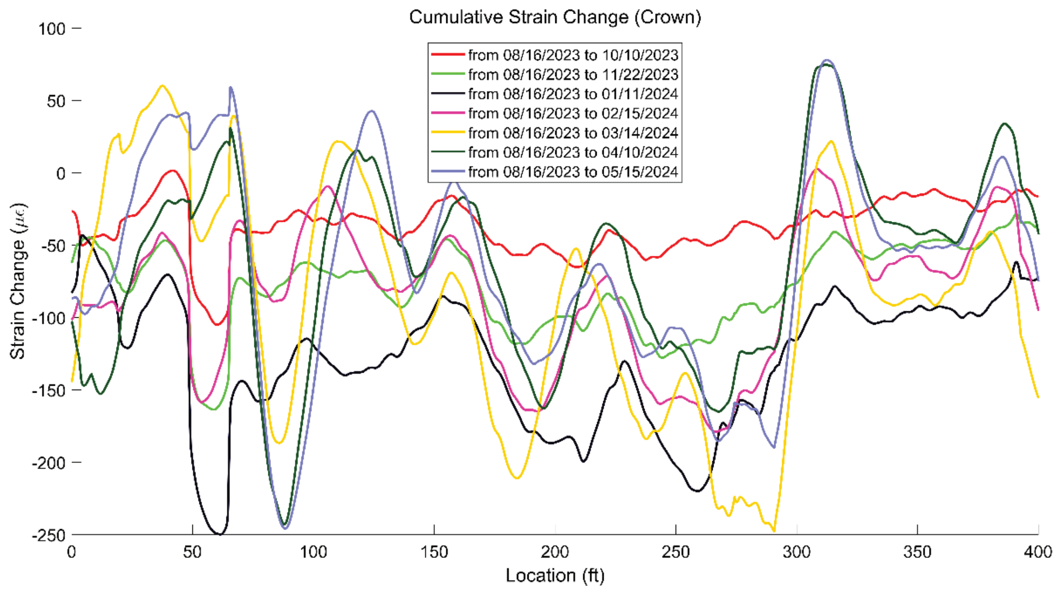

Figure 39: Cumulative strain change (crown)

4.3.5 Strain Change of the Pipeline at the -45° Location

Figure 40 and Figure 41 show the strain change at -45° of the pipe for each month and the cumulative strain change, respectively. It is evident that the findings closely resemble those observed at the other two locations. That is to say, an increase in ambient temperature causes the pipeline to elongate, while a decrease in ambient temperature leads to the pipeline contracting. The overall strain values measured are not significant, with monthly variations staying within 100 $\mu\varepsilon$. Notably, from January 2024 to February 2024, the tensile strain in the pipe begins to exhibit significance. In most time periods, the fluctuation range of strain is relatively small, typically between 50 and 100 $\mu\varepsilon$. Data obtained between February 2024 and March 2024 exhibit larger fluctuations compared to other measurements.

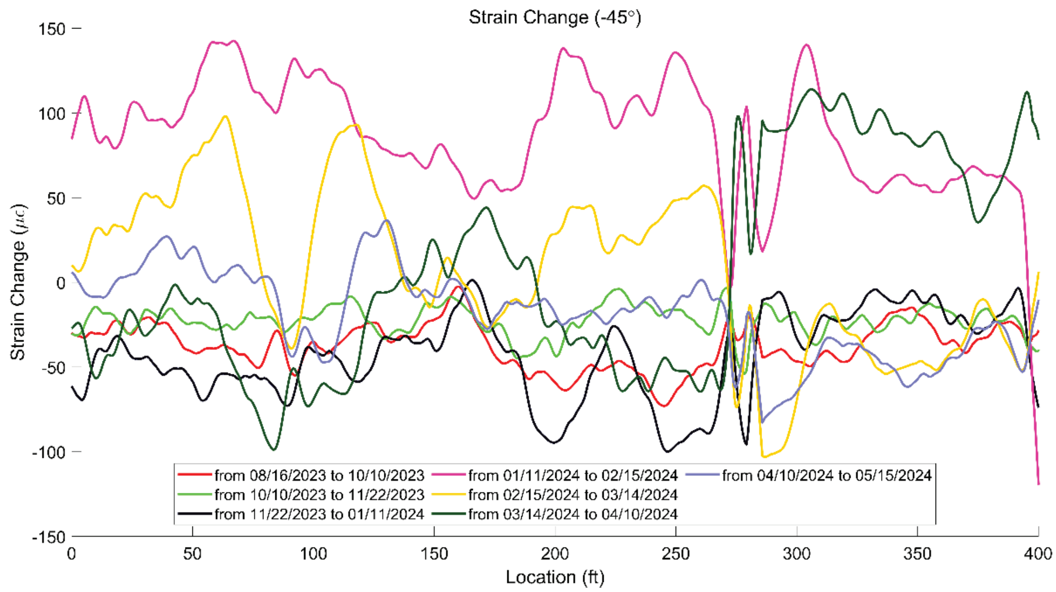

Figure 40: Strain change between each reading (-45°)

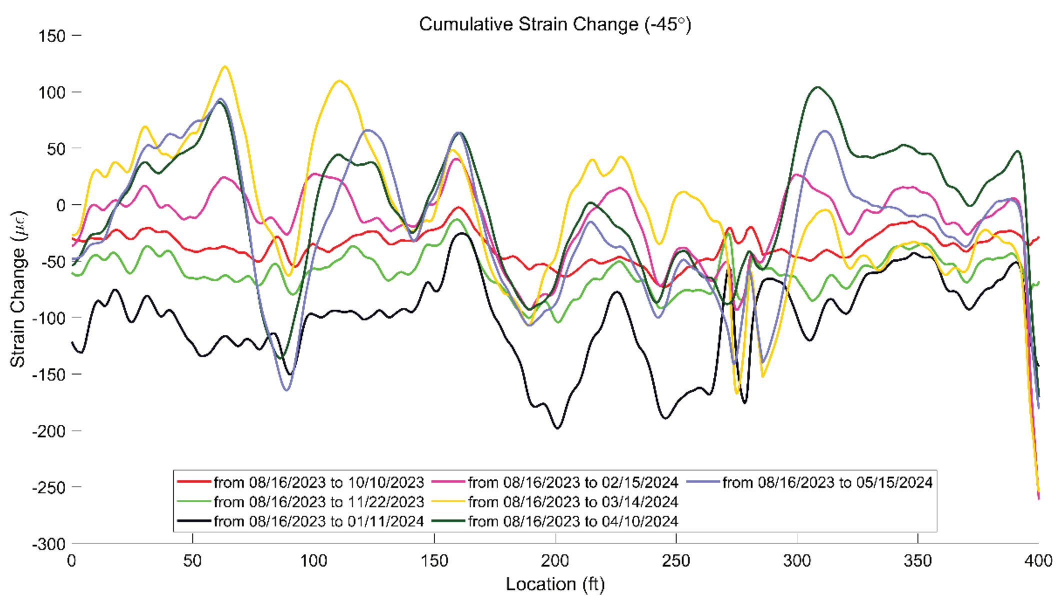

Figure 41: Cumulative strain change (-45°)

4.3.6 Strain Change in the Trench

The measured strain changes in the trench are shown in Figure 42, and the cumulative strain changes from August 2023 are presented in Figure 43. Between each month's readings, the strain change is generally small, typically less than 100 $\mu\varepsilon$. However, certain positions, such as at 400 feet, 650 feet, and 700 feet, exhibit relatively large strain changes. The overall strain change pattern in the trench corresponds with the temperature change trend, where increased temperatures lead to tensile strain and decreased temperatures result in compressive strain.

From January 2024 to February 2024, the data indicates tensile strain, suggesting soil swelling. This phenomenon may be associated with the significant rainfall events during this period, as soil tends to swell when absorbing water due to moisture absorption by its particles. The swelling can cause an increase in tensile strain within the soil.

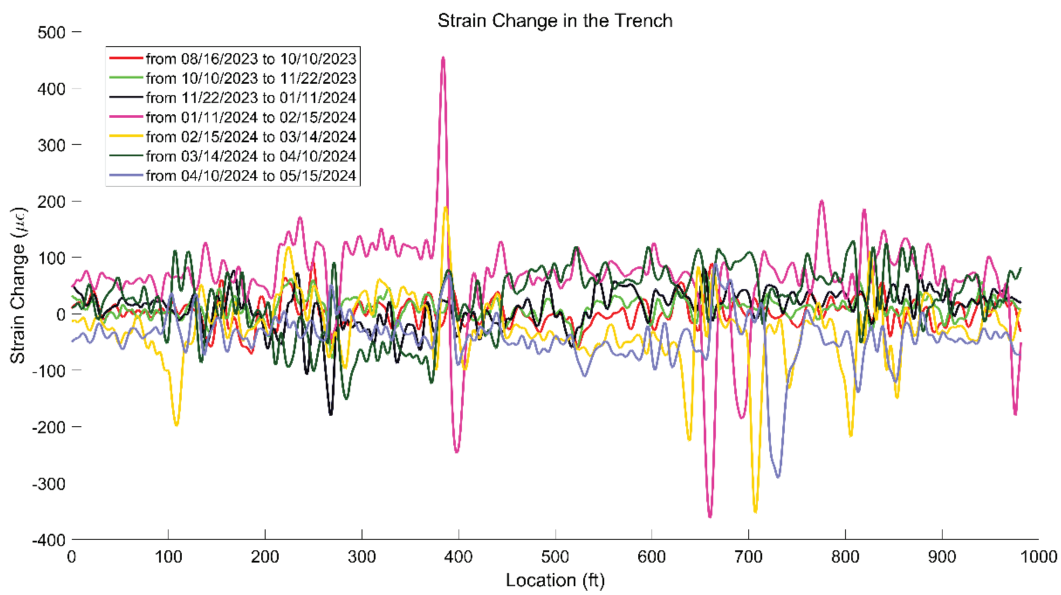

Figure 42: Strain change between each reading (trench)

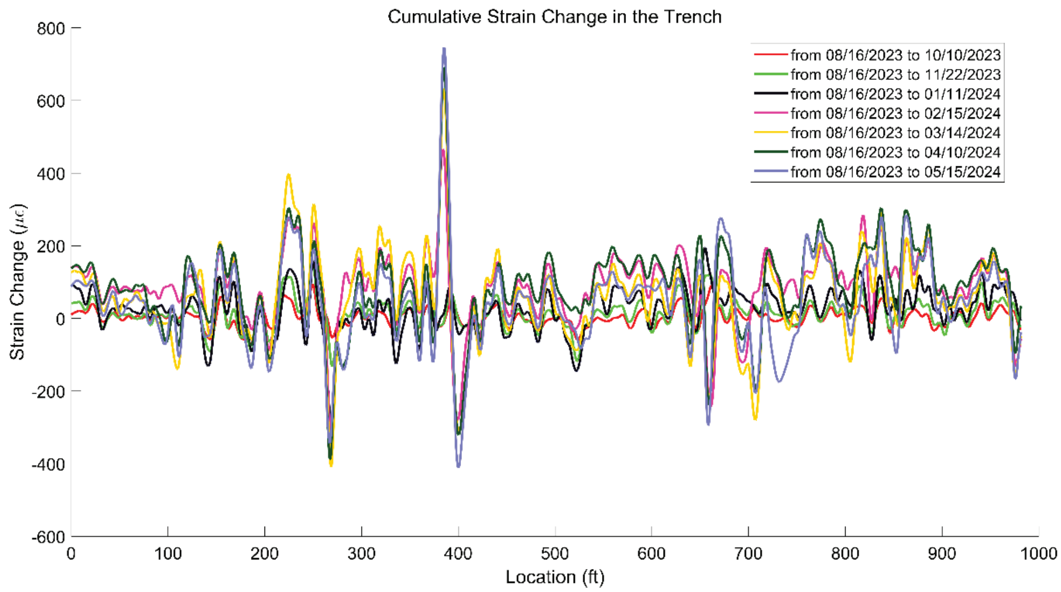

Figure 43: Cumulative strain change (trench)

For the strain optical fiber buried in the soil, it is positioned on the same side as the optical fiber at a -45° angle relative to the pipeline. When comparing the strain change results measured by this buried optical fiber with those on the pipeline, we observe that both reflect the same trend: tensile strain during temperature increases and compressive strain during temperature decreases. Within the current measurement cycle, which is less than one year, neither set of measurements has clearly indicated strain changes caused by fault movement.

However, unlike the optical fiber installed on the pipeline, the results measured by the optical fiber buried in the soil exhibit greater fluctuations and large strain changes at specific locations. To more accurately capture the strain changes of the pipeline, it may be more effective to install the strain optical fiber directly on the pipeline.

4.3.7 Guideline for Long-Term Strain Monitoring of Pipelines Using Distributed Strain Sensing

4.3.7.1 Introduction

Distributed Strain Sensing (DSS) is a sophisticated technique that provides continuous and real-time monitoring of strain along the length of pipelines. This guideline outlines the procedures and best practices for deploying and utilizing DSS for long-term strain monitoring.

4.3.7.2 Objectives

- To provide a structured approach for the deployment and use of DSS in pipeline monitoring.
- To ensure the acquisition of accurate and reliable long-term strain data.
- To offer guidelines for data interpretation, maintenance, and corrective actions.

4.3.7.3 Pre-Installation Considerations

Site Survey:

- Conduct a detailed survey of the pipeline route to identify potential areas of high strain concentration, such as bends, joints, and fault zones.
- Assess environmental conditions including soil type, temperature variations, and accessibility for maintenance.
- Document existing pipeline conditions for future reference.

Fiber Optic Sensor Selection:

- Choose fiber optic sensors that are specifically designed for strain sensing and are capable of withstanding harsh environmental conditions.
- Ensure the cables have a suitable strain range and sensitivity for the expected strain levels in the pipeline.

Sensor Placement Planning:

- Determine optimal sensor placement to ensure comprehensive strain coverage.
- Focus on critical areas such as welds, corrosion-prone sections, and geotechnically unstable zones.
- Plan for redundant sensor placement in high-risk areas to ensure data reliability.

4.3.7.4 Installation Procedure

Surface Preparation:

- Clean the pipeline surface thoroughly to remove any dirt, rust, or coatings that could interfere with sensor attachment.
- Use appropriate solvents and cleaning tools to prepare the surface for adhesive bonding.

Cable Attachment:

- Buried Installation:
    - In cases where direct attachment is impractical, bury the fiber optic cables in the soil near the pipeline.
    - Ensure the cables are placed at a consistent depth and are protected from potential mechanical damage.
- Direct Attachment:
    - Use high-quality adhesives to bond the fiber optic cables to the pipeline.
    - Apply adhesive continuously along the contact points and spread evenly using appropriate tools or fingers to ensure thorough coverage.
    - Secure the cables with duct tape at certain intervals during the curing process.
- Protective Measures:
    - Apply wax tapes to further secure and protect the cables after adhesive curing.
    - Fold the edges of the wax tape for a seamless transition to the pipeline.
    - Use outer wrap for additional protection, ensuring the wraps are soaked in water before application and maintaining an overlap rate of at least 40%.

Calibration:

- Perform initial calibration by applying known strains and recording the sensor responses.

- Establish a baseline data set to serve as a reference for future strain measurements.

4.3.7.5 Data Collection and Transmission

Data Acquisition:

- Install data acquisition units capable of capturing continuous strain data from the fiber optic sensors.
- Ensure the units are configured for real-time data logging and are capable of handling the expected data volume.

Data Transmission:

- Set up reliable data transmission systems to send collected data to a central monitoring station.
- Use redundant communication channels (e.g., cellular, satellite) to prevent data loss.

Backup Systems:

- Implement data backup systems to store collected data securely.
- Schedule regular data backups to prevent loss of critical information.

4.3.7.6 Data Analysis and Interpretation

Baseline Data:

- Establish a comprehensive baseline strain data set during the initial monitoring period.
- Use this baseline for comparison with future data to identify deviations and trends.

Trend Analysis:

- Regularly analyze strain data to identify trends, such as:
    - Temperature Effects: Separate strain changes caused by temperature fluctuations from those caused by external forces.

    - Anomalies Detection: Identify significant deviations from baseline data that may indicate potential issues, such as fault movements or structural weaknesses.

- Use advanced data analysis techniques, including statistical analysis and machine learning, to enhance trend detection.

Reporting:

- Generate regular reports summarizing strain data, trends, and identified anomalies.
- Include graphical representations of strain trends and any significant findings.
- Provide actionable recommendations based on the analysis.

4.3.7.7 Maintenance and Calibration

Regular Inspections:

- Conduct periodic physical inspections of the fiber optic cables and monitoring equipment to ensure they remain in good condition.
- Check for signs of wear, damage, or environmental degradation.

Calibration Checks:

- Perform regular calibration checks to maintain the accuracy of the DSS system.
- Recalibrate sensors as needed to account for any changes in environmental conditions or sensor performance.

Repairs and Replacements:

- Promptly repair or replace any damaged components to ensure continuous monitoring capability.
- Keep an inventory of spare parts and materials for quick replacement.

4.3.7.8 Summary

Implementing a robust DSS-based strain monitoring system provides valuable insights into the structural integrity of pipelines. By following these detailed guidelines, operators can achieve accurate, reliable, and long-term strain monitoring, thereby enhancing the safety and maintenance of pipeline infrastructure. This proactive approach enables early detection of potential issues, allowing for timely interventions and reducing the risk of catastrophic failures.

4.4 Task 5: Numerical Simulation

4.4.1 Task 5.1: Simulation of the Laboratory Four-Point Bending Test

The steel pipe four-point bending test conducted in the laboratory was simulated by the finite element method (FEM) to study the deformation and failure behavior. The FEM results were compared with the data measured by distributed fiber optic strain data to back-analysis the "most probable parameter" of the model. With the continuing updated parameter, the FEM simulation can be a predictable tool to assess the behavior of the pipe with the early-stage measurements and prevent failure in advance, which is meaningful in a realistic engineering project. Developing a reasonable and accurate model that can be used to check the real performance of the pipeline using distributed fiber optic sensor is crucial for finding "most probably parameter" and then predicting the failure behavior. In this section, a FEM of the experiment is built, optimized, and validated with available test results.

4.4.1.1 Finite Element Model Description

The industry-leading explicit simulation software, Ansys LS-DYNA, is chosen as the FEM tool to simulate this case.

Element type of the pipe: The whole pipe is a cylinder enclosed with two objects at both ends. It allows the pipe pressurized at 7.63 MPa from inside. Compared with the length, the thickness is neglectable, so that a shell assumption is acceptable here, which can save computational cost.

Material properties: The hardening elastic-plastic material type is employed in this case. The hardening tangential modulus is considered an unknown parameter that will need back-analysis to determine the value, and 10% of the elastic modulus is used in the current simulation.

Loading: The loading procedure in the FEM simulation is also separated into two main stages. In stage 1, the internal pressure is linearly increased from 0 MPa to 7.63 MPa. In stage 2, the pipe is pushed up at the inner actuator support locations (A1 and A2) also linearly with a displacementcontrolled mechanism.

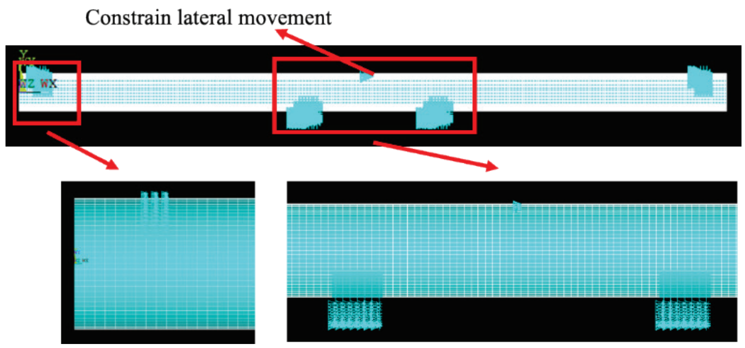

Figure 44: FEM discretization and boundary conditions

Boundary conditions: For the inner two supports with actuators A1 and A2, two boundary condition cases are considered. The first case pushes the nodes in the support domain directly so that all the nodes move up as a rigid body along Y-axis. The second case, which is adopted here, attaches a spring to each node (as shown in Figure 44) and pushes up at another side, not directly at the node on the pipe. This allows modeling of imperfections at the two inner supports. For the two outer supports, two cases are also considered. In the first case, the supports have fixed nodes. In the second case, the supports are connected to high stiffness springs to each corresponding node, similar to the inner actuator support boundaries. Furthermore, the movements along the X-axis of some nodes located at the middle of the pipe are limited to avoid rigid lateral movements of the pipe.

4.4.1.2 Results

The results shown below are mainly qualitative and used to compare the deformation pattern with the experiment. Quantitative results are still undergoing to determine "the most probable parameter" of the model. It is also noted that the strains discussed here are those in the longitudinal direction, which were what the distributed fiber optic strain system recorded.

Strain gage SG0: The strain at the center top of the pipe is used to control the magnitude of displacement in the experiment and used here to correspond to the time of the experiment and calculation one by one. As shown in Figure 45, at Stage 1, the axial strain increased linearly with the linearly increasing internal pressure and was kept almost constant during a time interval between the two stages. After the time interval, it increased again with displacement applied by the two actuators.

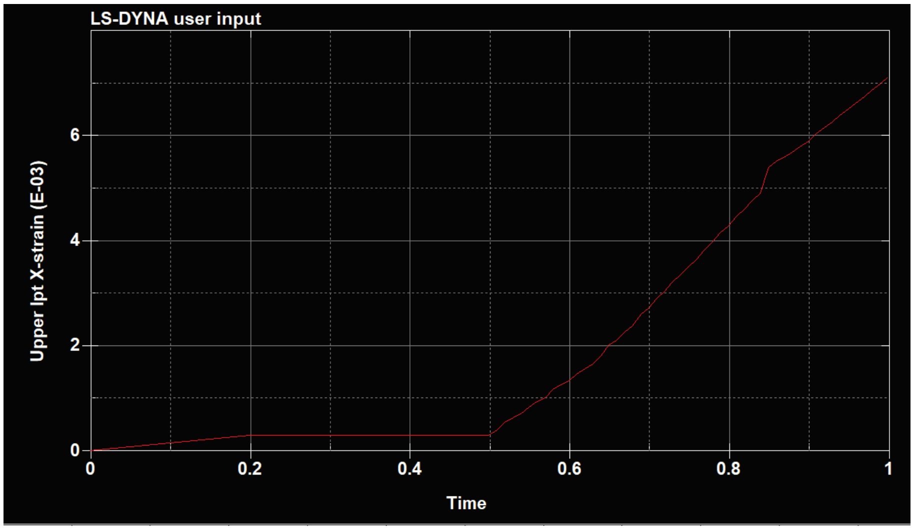

Figure 45: Strain profile of the cell at strain gage SG0

Figure 46 shows the strain distribution at the end of Stage 1 at the two sensing locations, S-NA-28° and S-NA+152°. The measured axial strain along the pipe with the applied pressure is almost constant and equal to about 280 $\mu\varepsilon$ for both the cables S-NA+152° and S-NA-28°. The strain profile predicted by the FEM analysis matches quite well with the experiment results. A small fluctuation in the predicted strain (within 10 $\mu\varepsilon$) can be observed near the actuators. Modeling the gravity loading (although the strains from it are almost negligible) causes a slight discrepancy with the experiment results.

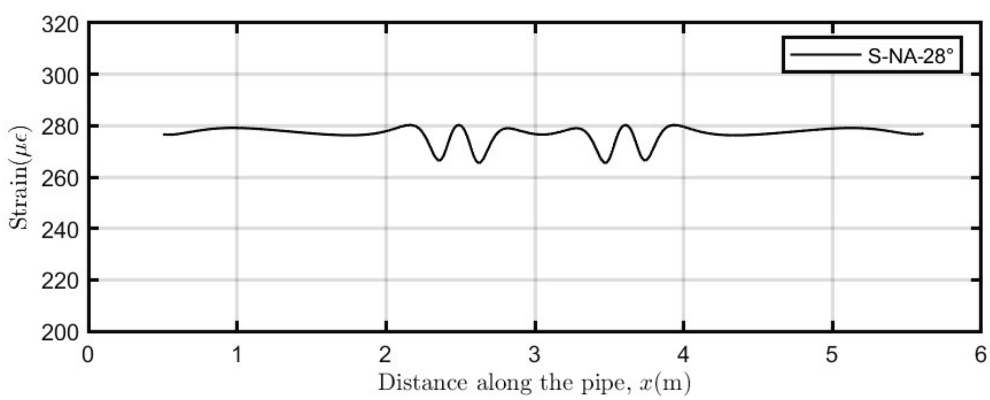

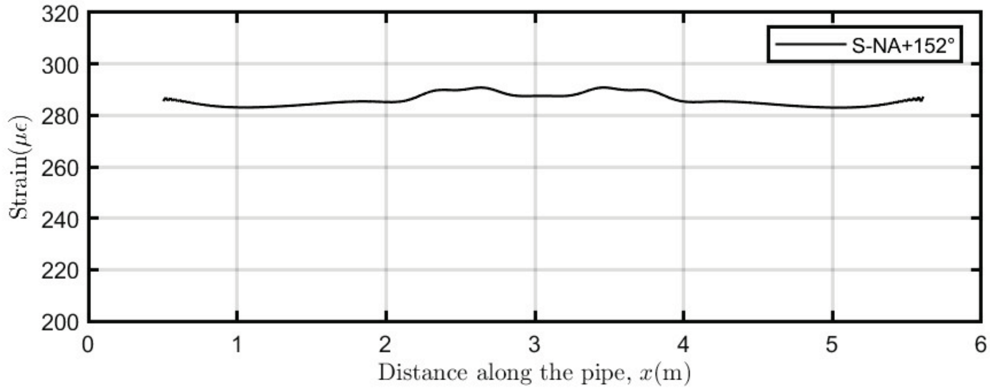

Figure 46: Axial strain distribution at the two sensing locations S-NA-28° and S-NA+152° from the numerical modeling at the end of Stage 1 (gravity and pressure loading)

Linear Elastic Response: The expected total strain at which the pipe material would first yield is about 2000 $\mu\varepsilon$. Figure 47 shows the distributed strain profile along the pipe at that stage. The numerical results agree well with the measured data, except for some expected differences near the actuator locations. For the S-NA+152° location, the numerical strain values near the actuator location are slightly larger. While for the S-NA-28° location, as expected, the strain values close to the actuator location oscillate around the measured data.

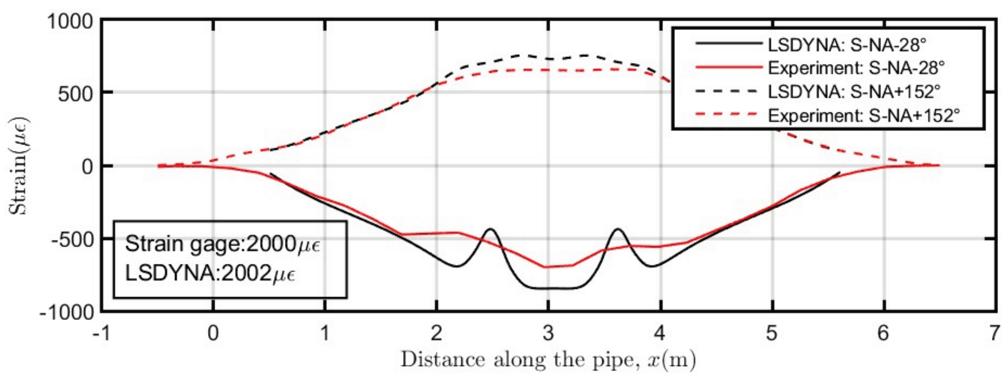

Figure 47: Comparison of the axial strain distribution at the two sensing locations, S-NA-28° and S-NA+152°, from the numerical modeling with the experimental data during Stage 2 for strain in the SG0 sensor equal to 2000 $\mu\varepsilon$

Elastic-Plastic Response: Plastic deformation occurs in the pipe after strain in SG0 > 2000 $\mu\varepsilon$. Figures 48 and 49 show the strain distributions in the pipe for a strain range of 5000 $\mu\varepsilon$ and 8000 $\mu\varepsilon$, respectively, at the SG0 location. The strain distribution is approximately symmetric in all the simulation results, indicating that the plastic deformation is symmetric. Figure 48 and Figure 49 show that the results from the numerical model agree well with the experimental observations. However, similar to the linear elastic response, outside of the loading region, such as near the actuator locations, there are some minor differences with the experimental data.

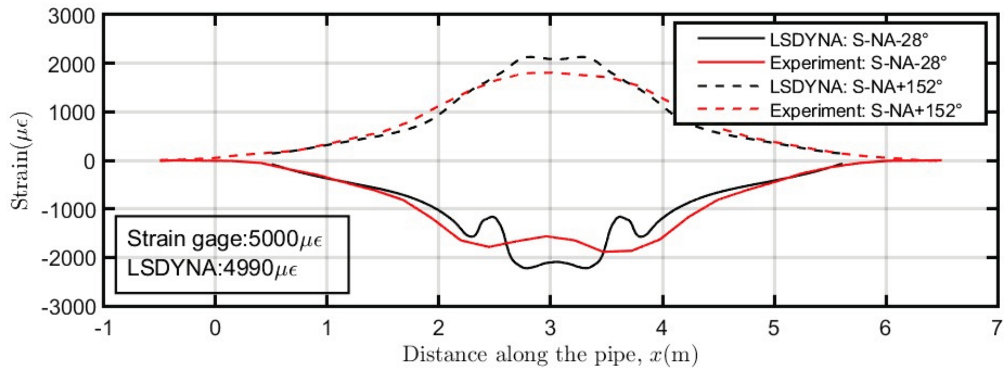

Figure 48: Comparison of the axial strain distribution at the two sensing locations, S-NA-28° and S-NA+152°, from the numerical modeling with the experimental data during Stage 2 for strain in the SG0 sensor equal to 5000 $\mu\varepsilon$

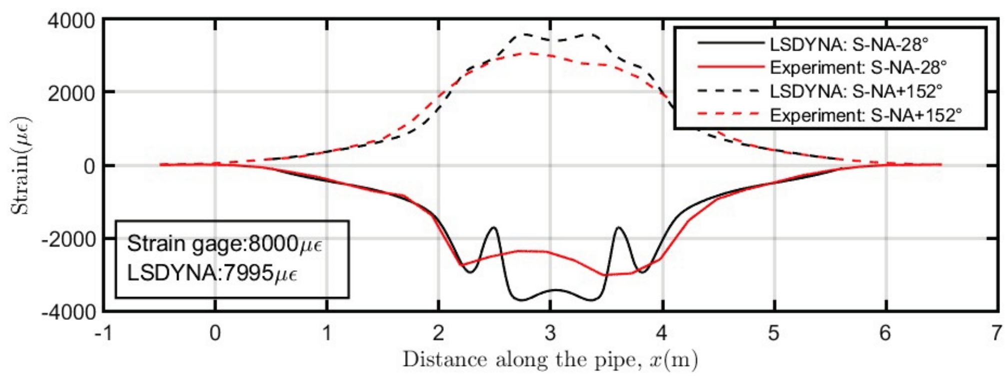

Figure 49: Comparison of the axial strain distribution at the two sensing locations, S-NA-28° and S-NA+152°, from the numerical modeling with the experimental data during Stage 2 for strain in the SG0 sensor equal to 8000 $\mu\varepsilon$

Failure Response: Figure 50 shows the strain distribution at the end of the loading when the failure occurred. The experimental data shows an obvious asymmetricity, while numerical results remain symmetric. Since the numerical simulation did not model any defect, it resulted in symmetricity. Figure 51 shows the deformed view of the pipe after the bending test. It can be observed that the material on the left side of the actuator A1 already failed, resulting in asymmetric behavior.

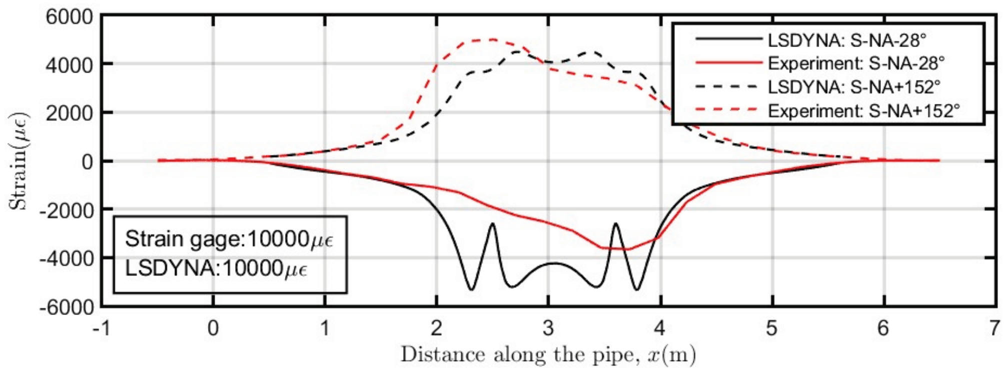

Figure 50: Comparison of the axial strain distribution at the two sensing locations, S-NA-28° and S-NA+152°, from the numerical modeling with the experimental data during Stage 2 for strain in the SG0 sensor equal to 10000 $\mu\varepsilon$.

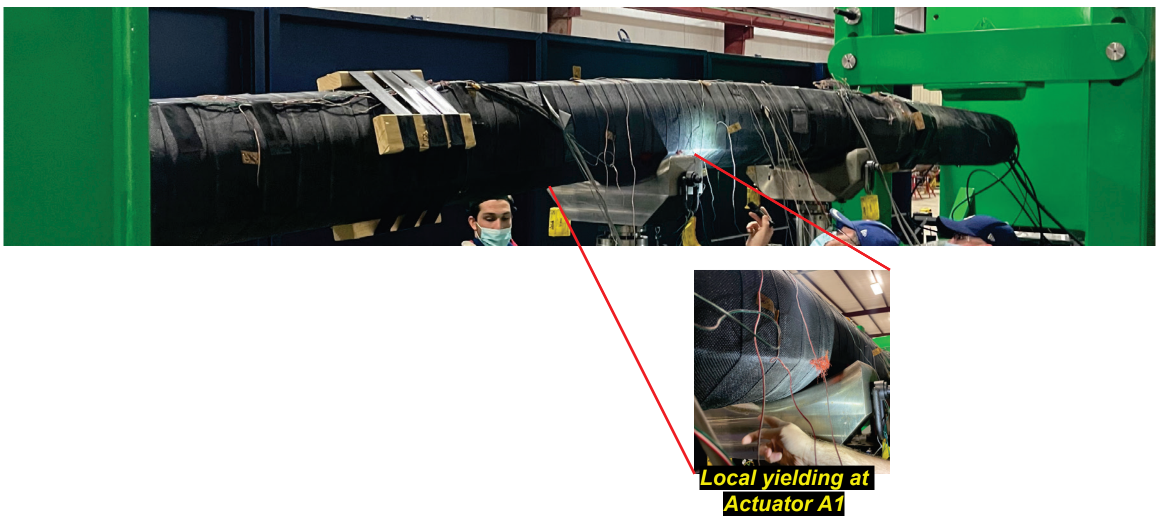

Figure 51: View of the deformed pipe at the end of the bending test

Influence of the boundary conditions: Figure 52 shows the effective plastic strain around the actuators when they are pushed upwards directly at nodes in the support domain. Several hardening values are simulated, and the maximum effective plastic strain always occurs between the actuators A1 and A2. By adopting multiple springs strategy for modeling the supports and adjusting the parameter, plastic strain can occur at the expected regions where the experiment showed (see Figure 53). The case with fixed boundary conditions at the two end supports always generate a narrow distribution of strain profile, which indicates stronger constraints are applied. Using springs instead of fixing the nodes, the simulation shows a better agreement with the measured data.

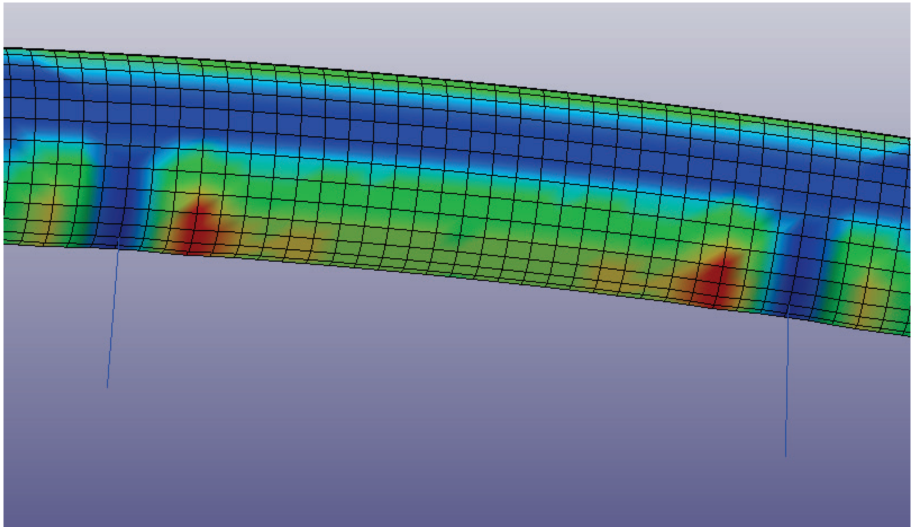

Figure 52: Effective plastic strain distribution around the actuators

Asymmetric stiffness at actuators: The experiment showed failure at the left side of the actuator A1. To reproduce this failure process, different stiffness values are applied to generate asymmetric deformation. As shown in Figure 53, the maximum effective plastic strain can be reproduced in the region where the experiment exhibited plastic failure.

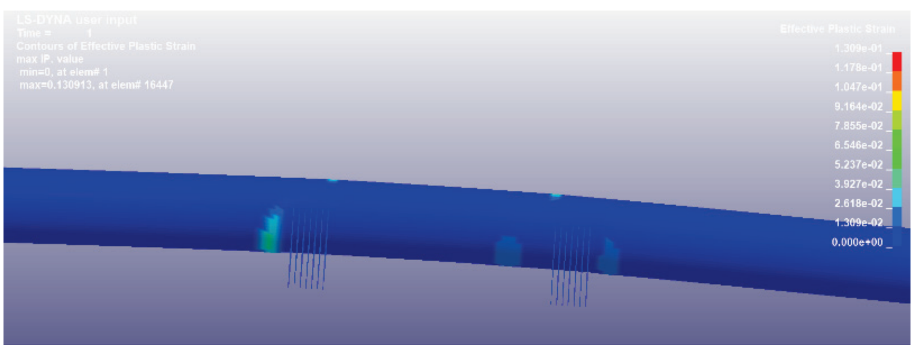

Figure 53: Failure at the left side of the actuator A1

4.4.1.3 Model Parameter Updating using the probabilistic Bayesian Estimation Method

In the FEM simulation presented above, the tangential hardening modulus of the steel was considered an unknown parameter, which was initially assumed to be equal to 20 GPa, i.e., the 10% of the initial young modules. In this section, the estimation of the tangential hardening modulus was improved by using the probabilistic Bayesian estimation method so that the FEM model can better predict the deformation for future loading conditions. In the Bayesian model, the hardening modulus of the pipe is chosen as the unknown parameter, ranging between (0%, 20%)

times the Young's modulus of steel. Since the hardening modulus affects the elastic-plastic response of the pipe, measured strains at X = 1, 1.25, 1.5, … 6 m along the cable location S-NA+152° for the case of $\mathrm{SG0} = 5000\ \mu\varepsilon$ are used as the observations. The updated hardening modulus obtained from $\mathrm{SG0} = 5000\ \mu\varepsilon$ is used to predict the deformation for the next stage, i.e., $\mathrm{SG0} = 6000\ \mu\varepsilon$. A uniform distribution is used as the initial prior for the unknown parameter. Figure 54 plots the posterior of the hardening modulus with the information observed in the experiment for $\mathrm{SG0} = 5000\ \mu\varepsilon$ using the Bayesian inference. The posterior has the highest probability at the value of 0.15.

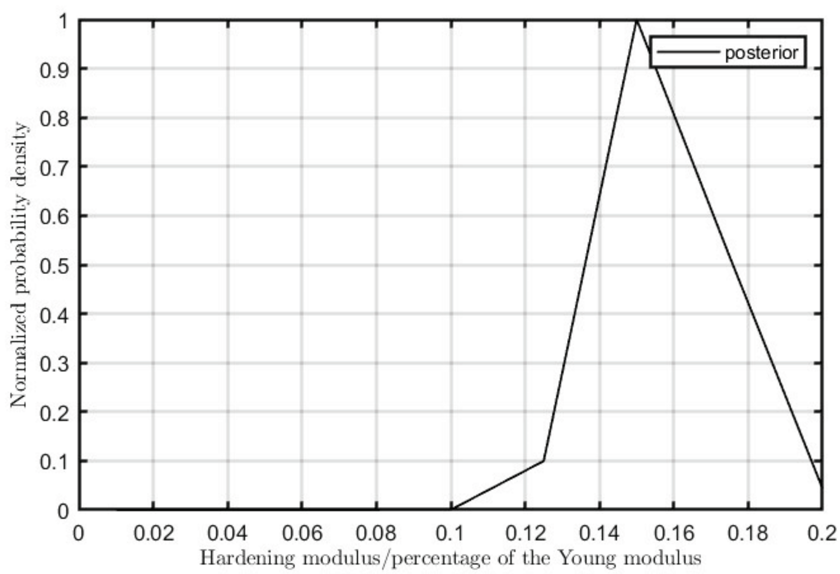

Figure 54: Posterior of the unknown parameter (i.e., the hardening modulus)

To validate the correctness of the Bayesian inference, the FEM model is repeatedly conducted with different hardening parameters to predict the deformation of the pipe at the next stage $\mathrm{SG0} = 6000\ \mu\varepsilon$. The quality of the model prediction is evaluated by calculating the Absolute Percentage Error (APE) defined as:

$$\mathrm{APE} = \frac{1}{n}\sum_{t=1}^{n}\frac{|\varepsilon_{\mathrm{i}} - \varepsilon_{\mathrm{i}}'|}{|\varepsilon_{\mathrm{i}}'|} \times 100\%$$

where n is the number of total observed data, ε_{i} and $\varepsilon_{\mathrm{i}}'$ is the i^{th} observation and its predicted value.

Figure 55 shows the Absolute Percentage Error (APE) distribution along the pipe for different values of the hardening modulus. The figure shows that the APE is the smallest for the case of hardening modulus equal to 0.15 times the Young's modulus of steel. The analysis results indicate that the most probable parameter value of the Hardening modulus can be taken as 0.15 times the Young's modulus of steel.

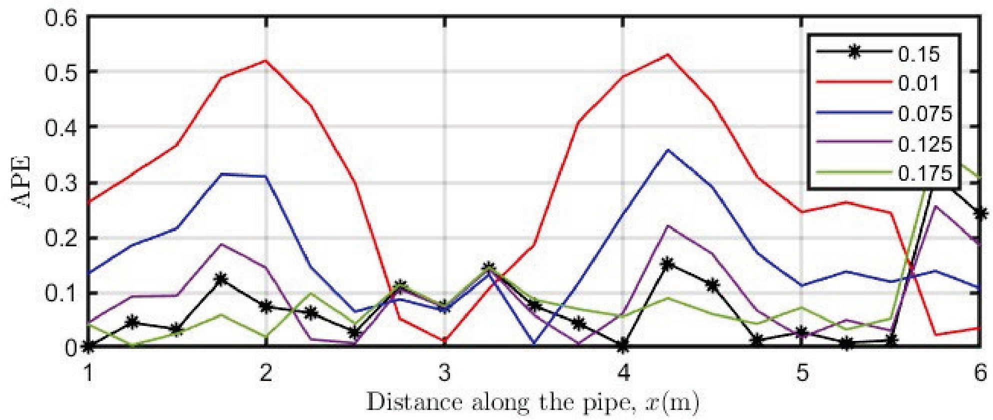

Figure 55: Absolute Percentage Error (APE) of the predicted distributed strain along the pipe with the measured strain for $SG0 = 6000\ \mu\varepsilon$

4.4.1.4 Discussion

The results from this FEM study demonstrate that the boundary conditions set in the simulation influence the pattern of the deformation significantly. With the boundary conditions normally used in practice (e.g., perfect conditions with fixed nodes at the four supports), the FEM model exhibits very different behavior compared to the experiment no matter what parameters are used in the simulation. However, by placing multiple springs to represent imperfect boundary conditions, the FEM model was able to capture the measured strain behavior, especially in the later stage when more plastic deformation and failure behavior are observed.

4.4.2 Task 5.2: Simulation of the Field Test Site

4.4.2.1 Finite Element Model Description

A finite element analysis using ABAQUS/EXPLICIT was conducted to examine the possible performance of the pipeline with fiber optic sensors in response to potential fault movement activities. The numerical model results will be compared with the monitoring data. The new pipeline was simplified in the model as two straight parts connecting by an elbow section. As shown in Figure 56, the longer section of the pipeline model was 200 m long, whereas the shorter section was 50 m long.

Figure 56: The finite element model of the pipeline

The modeled pipeline was embedded in the soil body according to the local topography provided in the design report, as shown in Figure 57. The complex topography was simplified to a polygon cross-section. The soil body in the model was relatively big, with a length of 300 m and a width of 230 m and had a maximum elevation of 100 m. The pipeline's burial location in the soil body is marked in red in Figure 58. The burial depth was about 1.2 m.

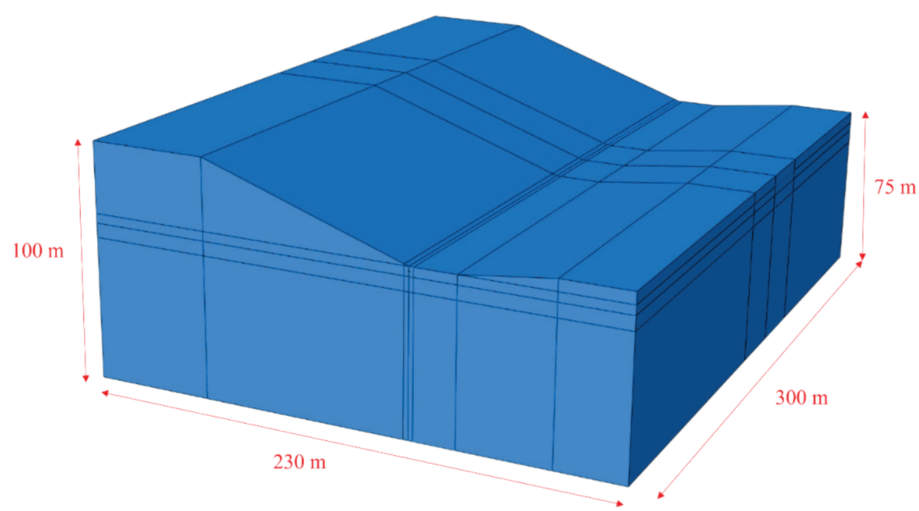

Figure 57: Geometry of soil body in the finite element model

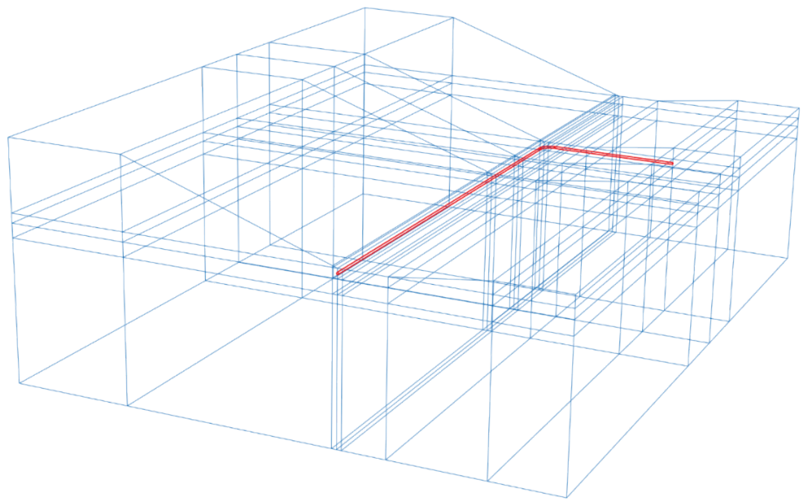

Figure 58: Location of the pipeline model (red part) inside the soil model

Solid elements (C3D10M: A 10-node modified quadratic tetrahedron) were used for the soil model. Although tetrahedron elements take a longer computation time than block elements, it is used to generate the mesh around the elbow region more accurately. The average element size was 3 m. Finer mesh was applied to the soil elements near the pipeline. In total, 819,369 elements were generated for the soil model, as shown in Figure 59. The soil model parameters were based on the design report. The soil above the pipeline is a moderately dense sand backfill with a friction angle of 35°. The soil underneath the pipeline was assumed to have a friction angle of 42°. And the dilation angle was 3°. The Young's Modulus was 30 MPa, whereas the Poisson's Ratio was 0.3. Total unit weight of 18.4 kN/m^3 (115 pcf) is used.

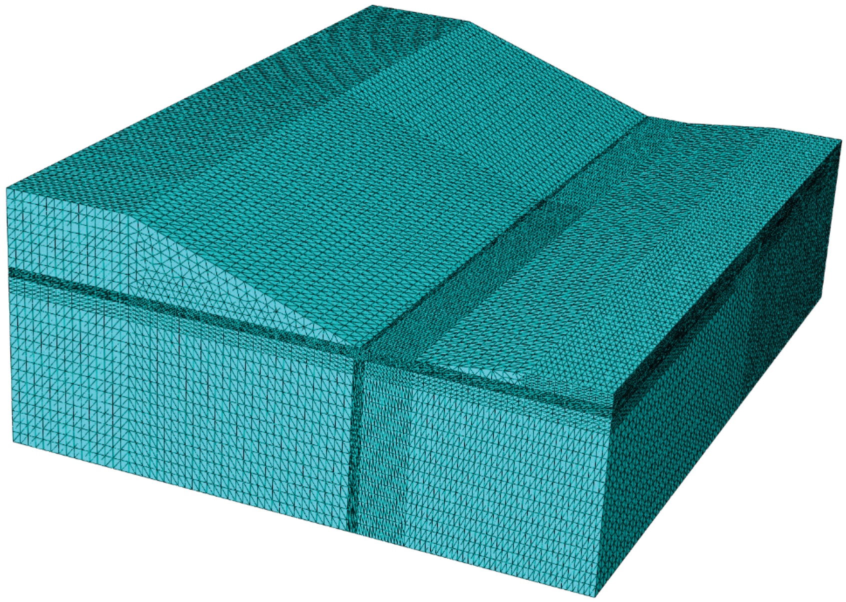

Figure 59: Mesh for the soil model

The replaced pipeline had an outer diameter of 0.86 m (34 inches) and a wall thickness of 1.28 cm (0.505 inches). Shell elements (S4R: A 4-node doubly curved thin shell with reduced integration, hourglass control, and finite membrane strains) with five thickness integration points are used for the pipeline. In the radial direction, the cross-section of the pipeline was divided into 24 parts. In total, 54,984 elements were used to model the pipeline, as shown in Figure 60. The new pipeline was API 5L Grade X65 steel, whereas the 3D elbow section is API 5L Grade X60. In this analysis, the pipeline materials were represented by piecewise-linear stress versus engineering strain curve based upon a generic Ramberg-Osgood formulation suggested by Walker and Williams (1995), as shown in Figure 61. Young's modulus was assumed to be 200 GPa, whereas Poisson's Ratio was set to be 0.3. For the interaction between the soil and the pipeline, the normal behavior was set to behave as the hard contact model in ABAQUS, and the tangential behavior was modeled using a friction coefficient of 0.8.

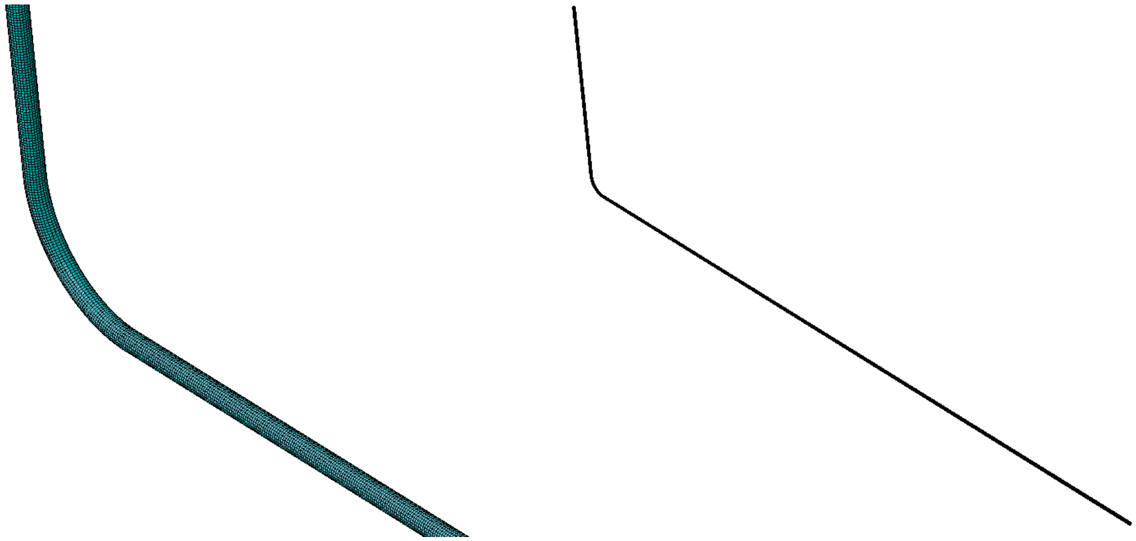

Figure 60: Mesh for the pipeline model

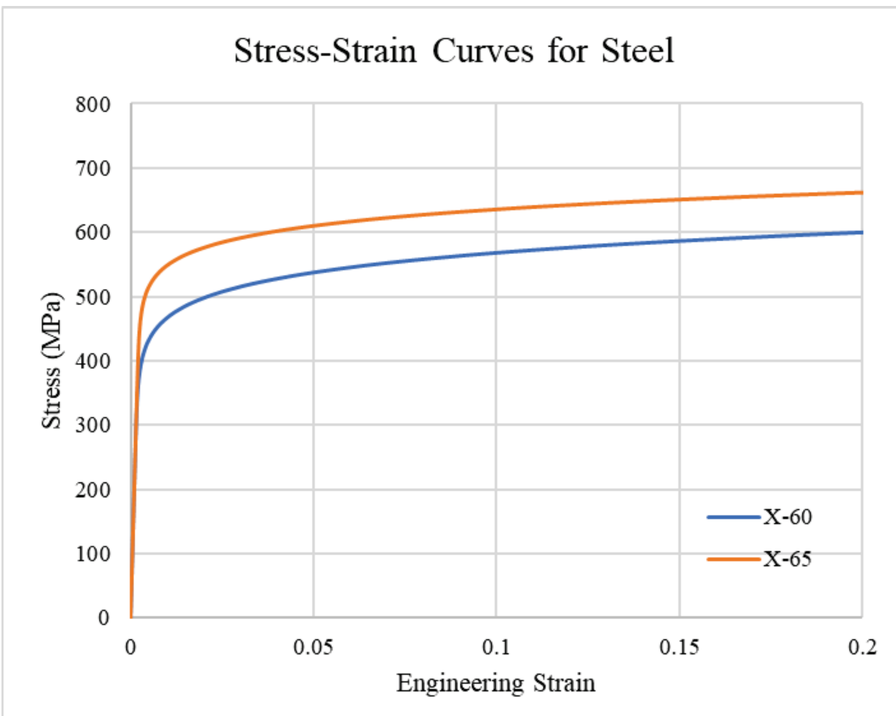

Figure 61: Stress-strain curves for steel

4.4.2.2 Imposed Fault Movement

A geological study of the field site was completed in 2017. At this crossing location, the width of the fault zone was estimated to be 70 m (230 feet). The variability in strike angle was estimated to be 340° ±5°. The geological study estimated an average right-lateral strike-slip rate of 0.35 to 0.79

in/yr. This slip rate estimate is within the High to Very High Slip Rate category as applied to the owner's consequence-hazard matrix for fault displacement. The required fault displacements are the 50th and 84th percentile displacement estimates, 0.85 m (2.8 feet) and 2.5 m (8.3 feet), respectively. The vertical displacement is assumed to be 10% of the horizontal displacement. The analysis included two cases that assumed the fault to be located either at the eastbound or the westbound of the fault uncertainty zone with a strike angle of 340°. The key parameters of the fault zone used in the analysis are shown in Table 3.

Table 3: Key fault zone parameters

Parameter		Value
Fault Strike		340°
50th Percentile Displacement	Horizontal displacement (m)	0.85
	Vertical Displacement (m)	0.085
84th Percentile Displacement	Horizontal Displacement (m)	2.5
	Vertical displacement (m)	0.25
Location	West Bound	30 m away from the elbow region
	East Bound	60 m away from the elbow region

4.4.2.3 Displacement

When the horizontal displacement reaches 2.5 m, and the vertical displacement reaches 0.25 m, the pipeline has the following deformed shapes for the two scenarios:

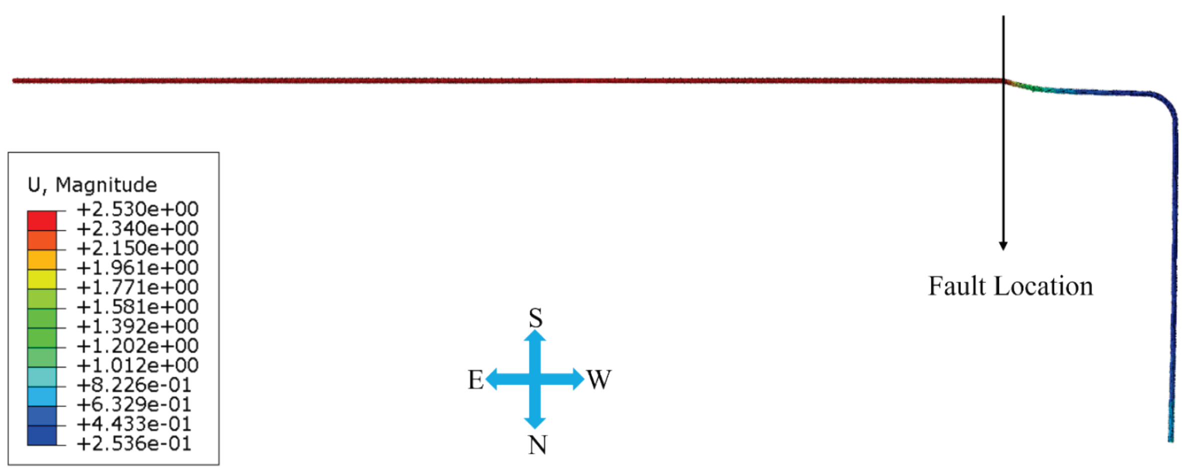

Figure 62: Pipeline deformed shape for the westbound case

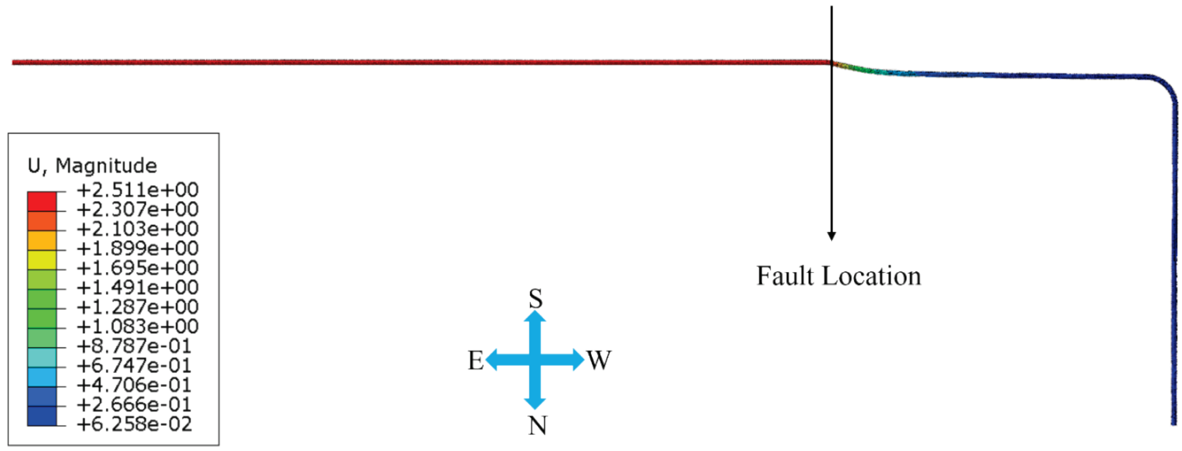

Figure 63: Pipeline deformed shape for the eastbound case

As shown in Figure 62, for the westbound case, the section on the east side of the fault plane moves uniformly with a magnitude of approximately 2.5 m. And then, there is a transition from the east to the west of the fault location where the displacement gradually decreases. The displacement of the elbow area is not very large compared to the fault displacement we applied. The north-south section of the pipeline has almost 0 displacements.

Figure 63 also shows that the eastbound case would have a trend similar to the one found in the westbound case. The section on the east side of the fault plane moves uniformly with a magnitude of around 2.5 m as the soil body does. And the displacement would get smaller from the east side of the pipeline to the west side. No obvious large deformation happens to the elbow part. The north-south section has relatively very small displacement as well.

4.4.2.4 Strain

The results of maximum tensile strain and maximum compressive strain under different percentile displacements of the side for both cases are summarized in Table 4. The fault movement in the westbound case causes a larger strain in the pipeline than in the eastbound case. The westbound case in which the fault plane is close to the elbow zone is a more critical case for the new pipeline.

Table 4: The Maximum longitudinal strain for different cases

Analysis Case	50th Percentile Displacement		84th Percentile Displacement	
	Maximum Tensile Strain	Maximum Compressive Strain	Maximum Tensile Strain	Maximum Compressive Strain
West Bound	1.99%	-1.37%	4.72%	-1.86%
East Bound	1.43%	-0.75%	3.50%	-1.52%

When the fault movement reaches the 84th Percentile Displacement Value, the strain distribution alongside the spring-line of the new pipeline on both sides is shown in Figure 64 and Figure 65 for the westbound and eastbound cases, respectively. Most of the pipeline has relatively very small longitudinal strains. There is a noticeable strain change within the 20-m section around the fault plane, implying a significant plastic deformation of this pipeline section.

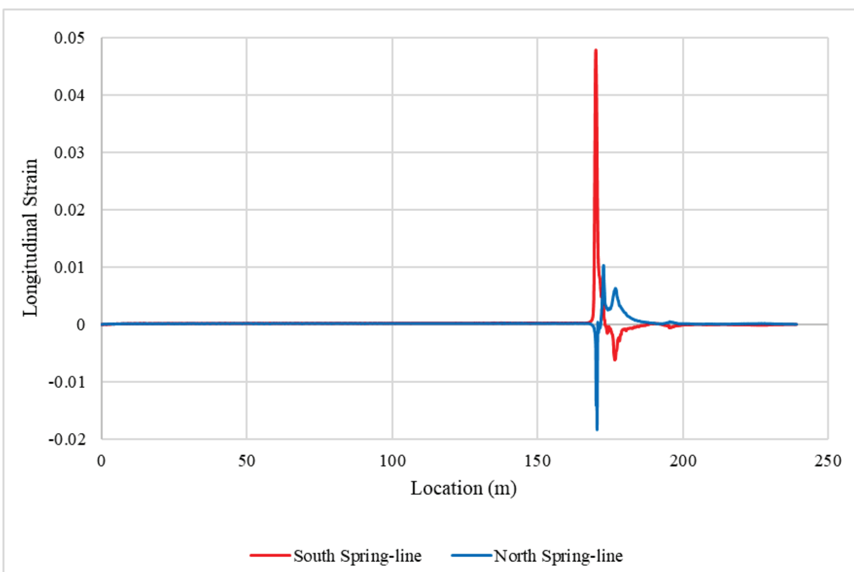

Figure 64: Longitudinal strain distribution of the pipeline for the westbound case

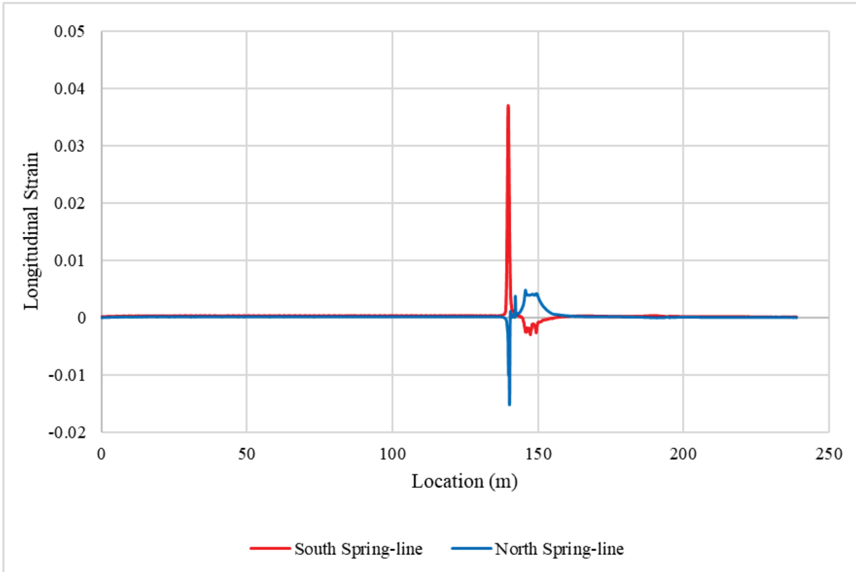

Figure 65: Longitudinal strain distribution of the pipeline for the eastbound case

The actual DSS data can be compared with these distribution patterns if a real fault movement with a similar displacement value happens to see how accurate this model is. By observing the distributed strain change data regularly, we aim to locate where a potential fault is happening or if any other kind of ground deformation is sabotaging the pipeline.

Figure 66 and Figure 67 show the development of maximum tensile longitudinal strain and maximum compressive longitudinal strain with fault displacement for the two cases. The maximum tensile longitudinal strain develops faster than the maximum compressive longitudinal strain in both cases. This also means that the maximum tensile strain would be larger at the final stage than the maximum compressive strain. As the fault moves, one end of the pipeline remains almost still, and the other end moves the same amount as the soil. The pipeline is elongated. During the movement, one side of the pipeline is subjected to active earth pressure due to the movement of the soil. In contrast, the other side of the pipeline is subjected to passive earth pressure as it is pushing the soil behind it. For the same soil, the value of passive earth pressure is usually larger than that of active earth pressure. The side where the tensile strain occurs in the pipeline moving section receives a more significant resistant force from the soil, making the stress and the strain larger on this side. The active earth pressure on the side where the compressive strain occurs is smaller compared to the other side. This leads to the stress and strain on this side are smaller than those on the other side. Therefore, at every step, the longitudinal tensile strain is greater than the longitudinal compressive strain, making the tensile strain grow faster than the compressive strain. And the tensile part gets a larger final value as well.

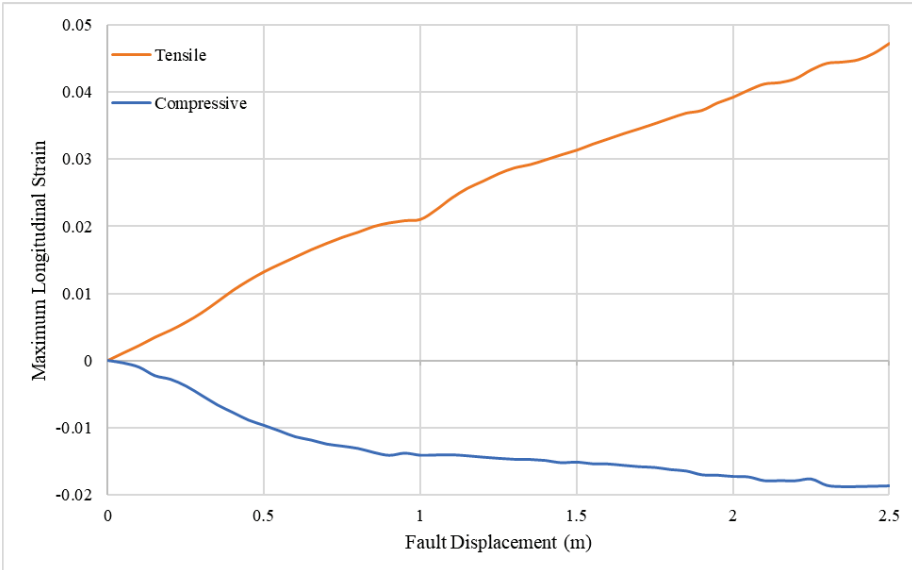

Figure 66: Maximum longitudinal strain with fault displacement for the westbound case

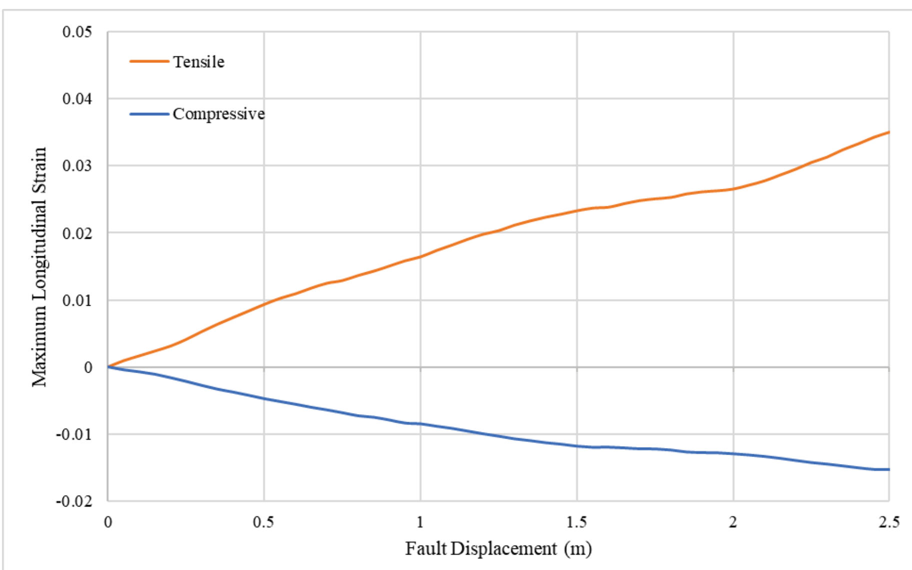

Figure 67: Maximum longitudinal strain with fault displacement for the eastbound case

4.4.2.5 Stress

The stresses in the longitudinal direction (mainly for the 200-meter part where the fault crosses) are plotted in Figure 68 and Figure 69 for the two cases. In the westbound case, the largest tensile stress is about 680 MPa, whereas the largest compressive stress is about 630 MPa. In the eastbound case, the largest tensile stress is about 630 MPa, whereas the largest compressive stress is about 580 MPa. As discussed above, X-65 has a yield stress of 483 MPa and both the largest tensile stress and the compressive stress are observed beyond the yield stress, which means this part of the pipeline is at the plastic deformation stage.

Figure 68: Longitudinal stress of the pipeline for the westbound case

Figure 69: Longitudinal stress of the pipeline for the eastbound case

The results show that the westbound case would result in larger stresses compared to the eastbound case. In the westbound case, the fault movement occurs closer to the elbow area than in the east case. Also, the length of the pipeline where the large displacement occurs is longer. As the pipeline section in the north-south direction needs to remain static, the transition area between the moving section and the stationary section is relatively shorter in the westbound case, making the displacement and the strain of the pipeline change more dramatically. In addition, in the westbound case, the elbow area is more affected by the fault movement since the fault plane is closer to the elbow area. The elbow area uses a material (X-60) that is not as strong as the other parts (X-65), which not only produces more strain during the whole ground movement process but also causes the pipeline section between the elbow region and the fault to bear greater stresses.

4.4.3 Task 5.3: The Role of Distributed Strain Data for Pipeline Assessment

Many past studies (analytical, numerical, and experimental) on pipeline behavior under fault movement focus on the "maximum" or "peak" tensile or compressive strain that may occur in the pipeline under a given fault angle and displacement. By adopting this peak-strain-based design approach, engineers can ensure that pipelines are designed to withstand the maximum anticipated loads and strains, providing a higher level of safety and reliability. However, this approach hypothesizes that the "idealized" assumed mechanism of soil-pipeline interaction used to determine the location of the peak strain is correct. This research instead proposes to use distributed fiber optic strain data either (i) to confirm that the idealized mechanism is correct and hence the design was appropriate or (ii) to revise the soil-pipeline interaction mechanism based on the rich dataset obtained from the DSS system. It is proposed that this performance-based approach reduces the risk of pipeline failure and potentially provides pre-warning to failure so that proactive mitigation actions can be made.

Previous assessment on existing analytical solutions or finite element analysis only focuses on the maximum tensile strain or maximum compressive strain itself, without much consideration of its axial and circumferential positions in the pipeline. According to the results of 3D FE continuum model results (see later), the position of the peak strain shift during the fault displacement process. For example, Figure 70 and Figure 71 show how the peak tensile/compressive strain location changes with the fault movement based on the results from Vazouras et al. (2010). The location of the maximum tensile strain gradually changes as the fault displacement increases. On the other hand, the location of the maximum compressive strain remains relatively unchanged during the whole fault movement process.

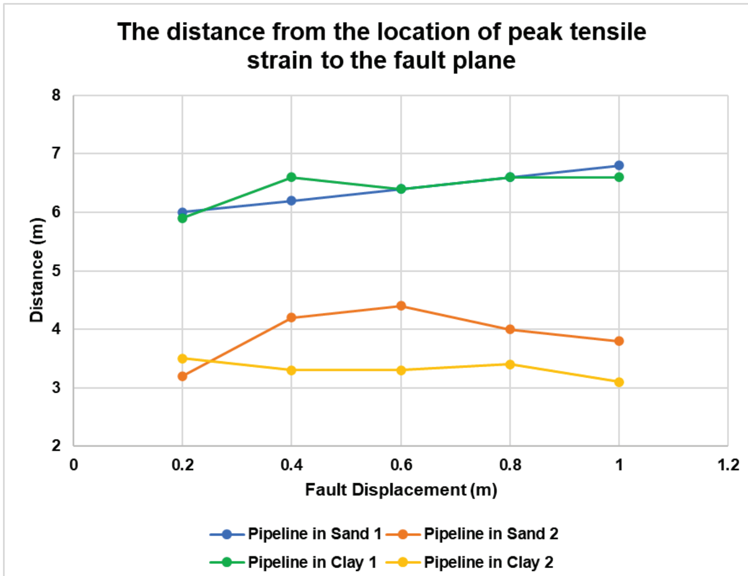

Figure 70: Peak tensile strain location from the Vazouras et al. (2010) model

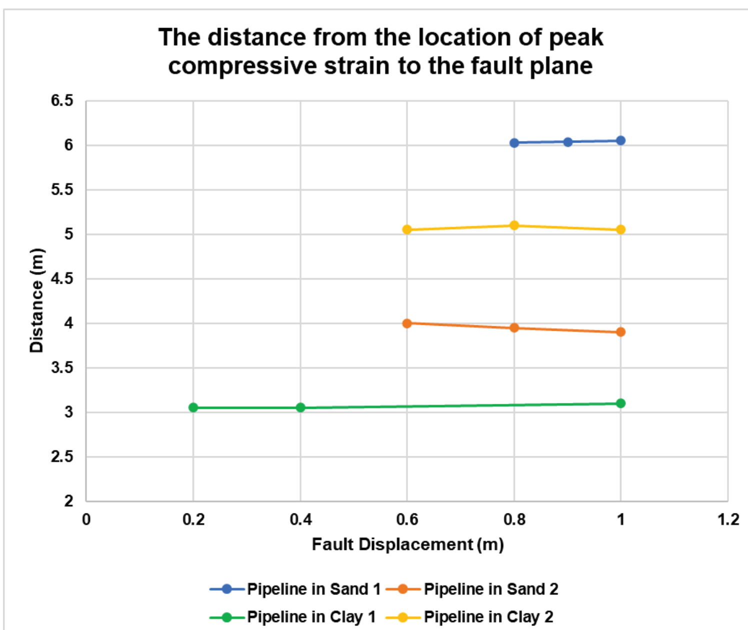

Figure 71: Peak compressive strain location from the Vazouras et al. (2010) model

It is also important to note that different analytical models currently used for soil-pipeline interaction analysis provide different "estimated" strain distribution due to differences in the mechanism assumed to develop the models. To illustrate the difference in strain distributions, a specific case is used here. The pipeline material is assumed as APL X65. It has an outer diameter of 0.9144 m (36 inches) and a wall thickness of 0.027 m (0.5 inches). Its burial depth (to the top of the pipeline) is 1.3 m. The surrounding soil has a unit weight of 18 kN/m^3 and an internal friction angle of 36°. The coating dependent factor to determine the friction between the soil and pipeline is 0.9. The fault displacement is 2.7 m (which is triple the pipeline diameter), and the crossing angle is 60°. Figure 72 shows the axial strain distributions in the longitudinal direction of the modeled pipeline evaluated from three different analytical solutions, whereas Figure 73 shows the axial strain distributions along the circumferential direction evaluated from two analytical solutions.

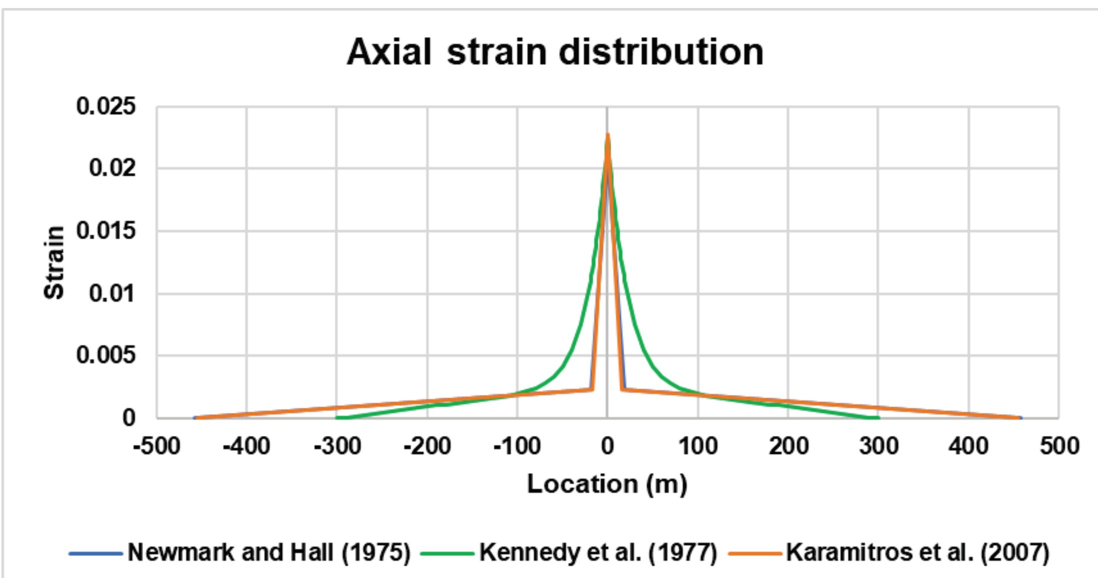

Figure 72: Axial strain distribution for a given case from different analytical solutions

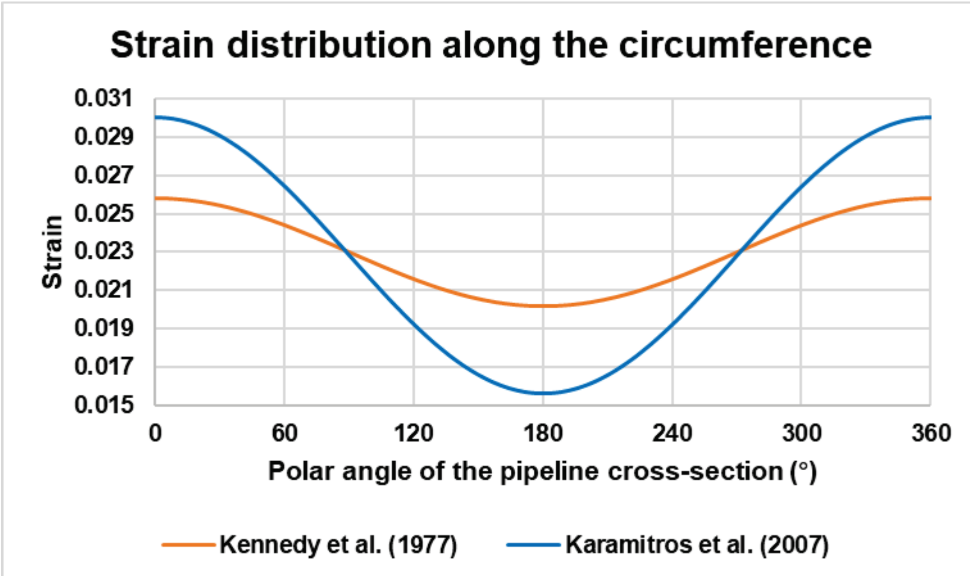

Figure 73: Strain distribution along the circumference for a given case

The Newmark & Hall (1975) method shows that the pipe length over which elastic strain develops is 439.1 m and the length over which plastic strain develops is 18.2 m, which makes the effective unanchored length become 457.3 m. The maximum tensile strain is 0.021, whereas the average tensile strain used to judge whether the pipeline is safe is 0.0015. The Kennedy et al. (1977) method, on the other hand, does not include the unanchored length calculation. The users need to assume the anchor point by themselves. However, for the given situation, if the unanchored length from the Newmark & Hall (1975) method is used, a convergence issue would occur. Therefore, the anchor point is assumed to be 300 m away from the fault trace on both sides. Under this condition, this method will give a curved part with a length of 19.6 m and a straight part with a length of 280.4 m. The maximum axial strain estimated from this method is 0.023. Kennedy et al. assumed a constant curvature part for the center region and therefore the bending strain remains the same. The bending strain is 0.0028. The Karamitros et al. (2007) method uses a pipeline curved length of 12.5 m. The region in which plastic axial strain develops is 16.3 m. The unanchored pipeline length calculated is 455.3 m. The maximum axial strain calculated from this method (at the location where the pipeline intersects with the fault trace) is 0.0228 and the bending strain is 0.0072. The maximum bending strain location happens at 102 m away from the fault trace.

In summary, for this hypothetical case, the methods by Newmark & Hall (1975) and Karamitros et al. (2007) estimate a similar value of unanchored length which is around 455 m. Both Newmark and Hall (1975) and Karamitros et al. (2007) use bi-linear stress-strain model to represent the pipeline material behavior, whereas Kennedy et al. (1977) use Ramberg-Osgood stress-strain model. Although all three methods provide a similar maximum tensile strain value (around 0.022), Newmark & Hall (1975) and Karamitros et al. (2007) show similar strain distribution, but Kennedy et al. (1977) gives a different profile. This is because of the differences in the unanchored length assumption and the material model.

At the early stage of fault movement (e.g. 0.3 m), the pipeline strains are relatively small (less than 100 $\mu\varepsilon$) even for the section close to the fault as shown in Figure 74 and Figure 75. However, it is argued in this study that a typical precision of the fiber optic strain sensor is about 30 $\mu\varepsilon$ and hence the expected strain level even at small fault movement is within the measurable range of the system. If the distributed fiber optic strain information is available for the entire pipeline, it is possible to continuously track the response of the pipeline throughout the fault movement from the early stage, so as to give early warning of possible risk of pipeline damage.

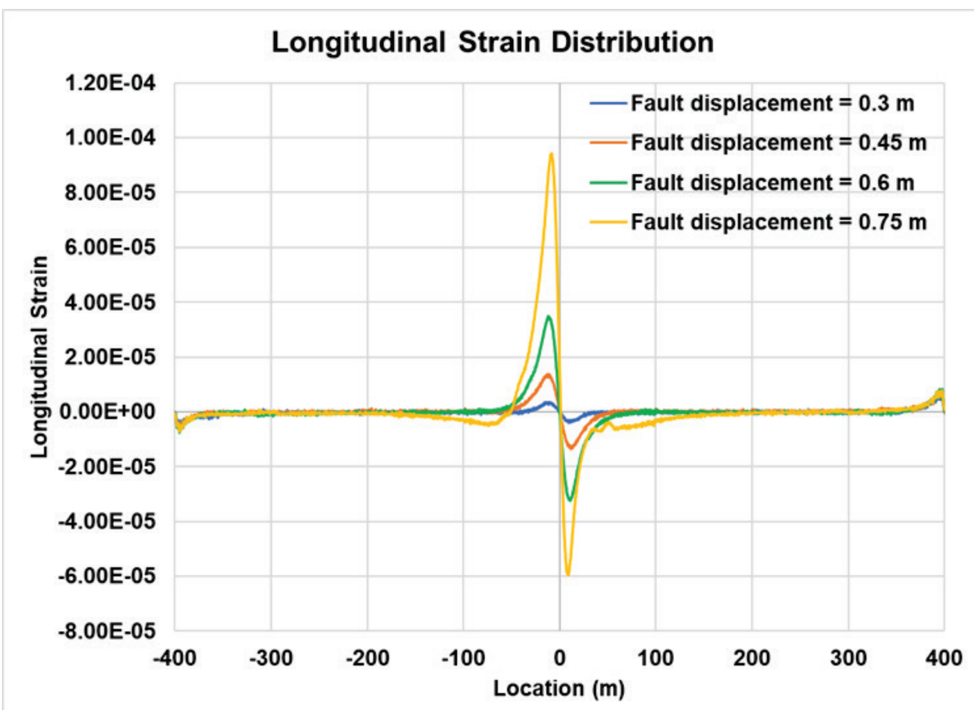

Figure 74: Longitudinal strain distribution for a given case

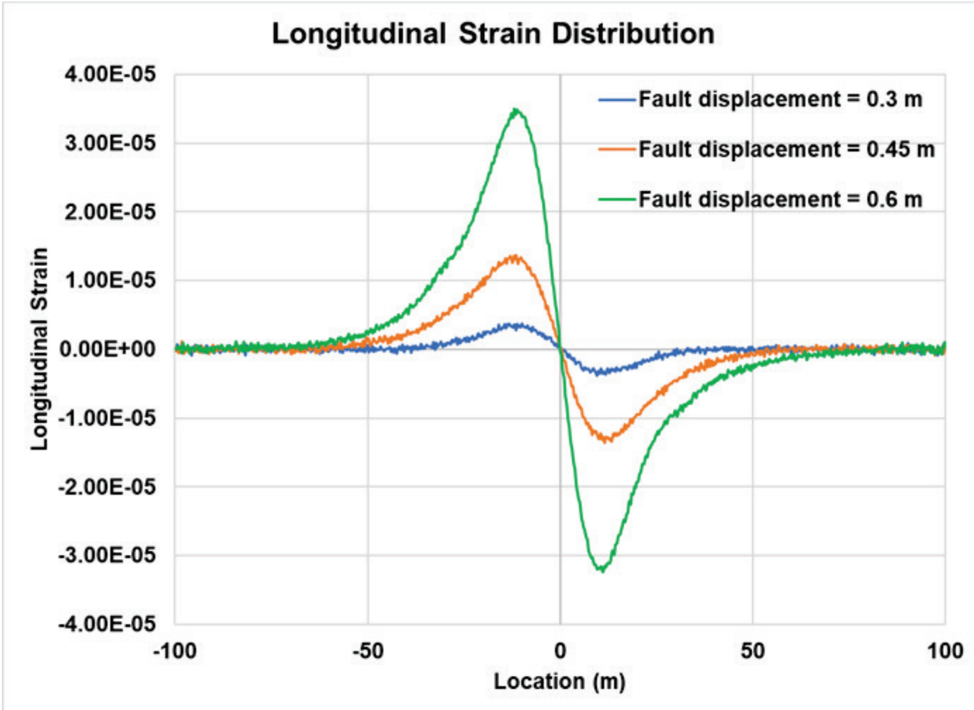

Figure 75: Longitudinal strain distribution for a given case (center 200-m region)

Different sections of the pipeline might have varying material properties due to manufacturing variations (welding), material degradation, or repairs. Variations in material properties, such as modulus of elasticity or yield strength, can influence the strain distribution. Changes in pipe geometry, such as diameter variations, wall thickness variations, or the presence of bends and fittings, can affect the strain distribution. These changes can lead to localized strain concentrations or stress raisers along the pipeline. If only strain is measured at small number of specific points, it is difficult to locate possible anomalous nature of the pipeline due to large uncertainty in the interaction of soil-pipeline crossing a fault.

Understanding the distributed strain profile along deformed pipeline is crucial for its design, as it helps engineers assess the structural integrity and performance of the pipeline. By analyzing the strain distribution, it is possible to identify areas of potential concern, such as locations with high strain concentration or excessive deformation, and make informed decisions regarding design modifications, material selection, or support systems to ensure the pipeline's safe and efficient operation.

4.4.4 Task 5.4: Simulations of Generic Fault rupture Cases

In this study, numerical simulation using the finite element method is chosen to examine the response of a gas pipeline to large ground deformation, which can then be used to assess the DSS data. In the previous study, most of the numerical simulation research focused on simplified models given the modeling cost and computation time. The soil is often simplified as springs that act on the pipeline. The sizes of these models are typically small. However, to restore the true situation of the pipeline and reduce the impact of the boundary on the entire analysis to the greatest extent, a 3D continuum model in which the soil and the pipeline have very large dimensions is developed in this study. The study started by simulating a pipeline response due to strike-slip fault movement.

Through DSS technology, it is possible to obtain the strain data of the pipeline on the basis of very small intervals so as to grasp the actual deformation situation of each position of the pipeline. With such high-quality data, it is possible to verify the accuracy of the existing analysis results and further improve the modeling method (e.g., material constitutive models, boundary conditions, meshing, etc.) on this basis. This helps to make the soil-pipeline interaction analysis closer to the actual situation. At the same time, numerical simulation can aid to evaluate the possible deformation or failure mechanism of the pipeline.

4.4.4.1 Finite Element Model Validation

In order to validate the finite element model under development, the outcomes of the current finite element analysis were compared with the experimental results obtained from a pipeline shearing test conducted at Cornell University. The experimental configuration, illustrated in Figure 76, involved a 10-meter-long pipeline with a diameter of 0.4 m and a burial depth of 1.2 m. The fault crossing angle was set at 65°, and the mobile section was displaced by 1.22 m.

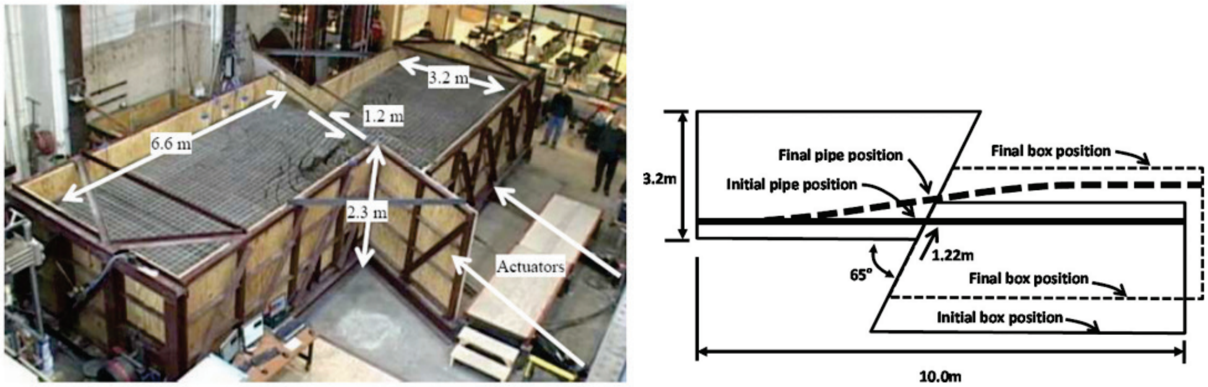

Figure 76: Experimental setup

Building upon this premise, as depicted in Figure 77, a 3D finite element model measuring 12 m by 12 m by 2 m was formulated. This model, a scaled-down version of the preceding finite element analysis, maintained similar characteristics. The soil was represented by soil elements, and a refined mesh was employed, particularly around the pipeline and fault plane. Two soil constitutive models, namely the Mohr-Coulomb Model (Terzaghi et al., 1996) and the Nor-Sand Critical State model (Jefferies, 1996; Jefferies & Been, 2006), were examined. The pipeline was simulated using shell elements, divided into 32 segments in the circumferential direction, with a finer mesh utilized for the central portion. Similar to the experiment, one-half of the soil was fully constrained, while the other half experienced applied displacement.

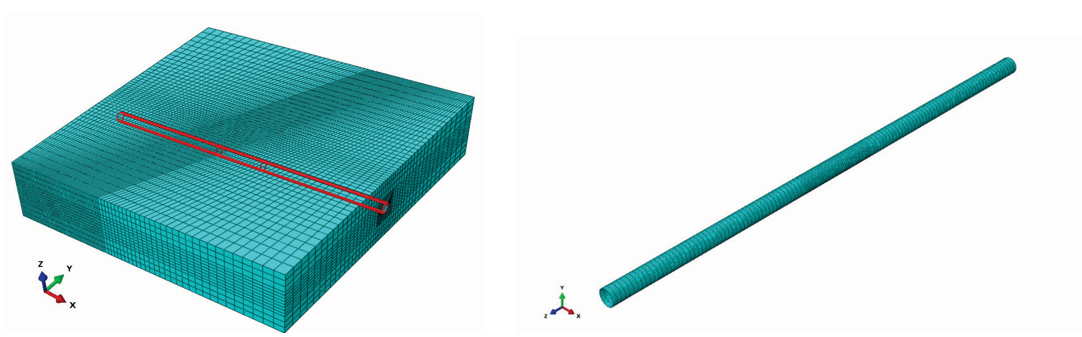

Figure 77: Finite element model for the validation

The strain distributions at displacements of 300 mm, 600 mm, and 900 mm are compared in Figure 78, Figure 79, and Figure 80, respectively. Each figure illustrates the measured strain at specific locations in the experiment alongside the strain obtained from the finite element modeling using both constitutive models. As evident from the figures, the finite element model employing the

Mohr-Coulomb model does not yield precise strain results. However, the finite element model utilizing the Nor-Sand critical state model exhibits improved performance.

For the fixed half, across all three stages, the finite element model with the Nor-Sand Critical State Model captures the actual experimental data points. The primary distinction in this half is observed near the boundary, where the finite element model displays slightly larger strain compared to the experimental data. In the moving half, especially during the initial stages with small displacements, the finite element model with the Nor-Sand Critical State Model initially fails to align with the experimental data. However, as the fault displacement increases, the strain from the finite element model aligns well with the experimental data.

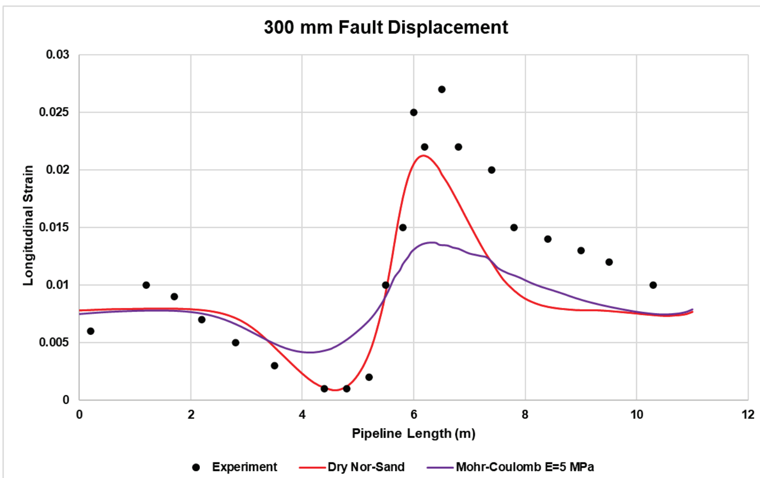

Figure 78: Strain distribution at a fault displacement of 300 mm

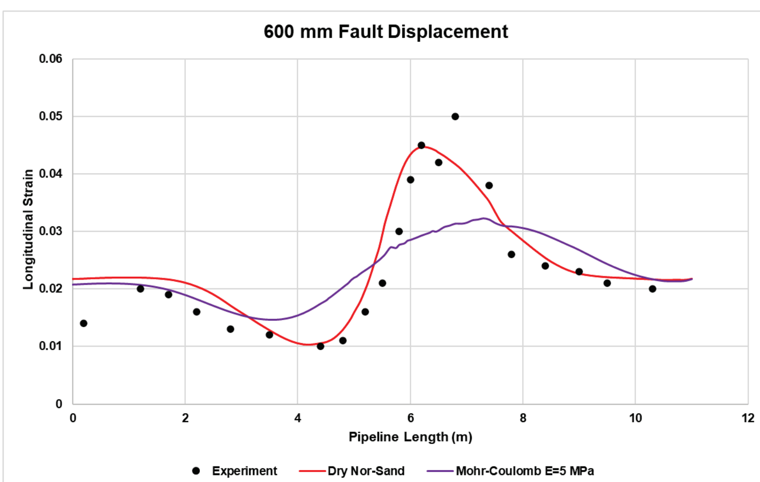

Figure 79: Strain distribution at a fault displacement of 600 mm

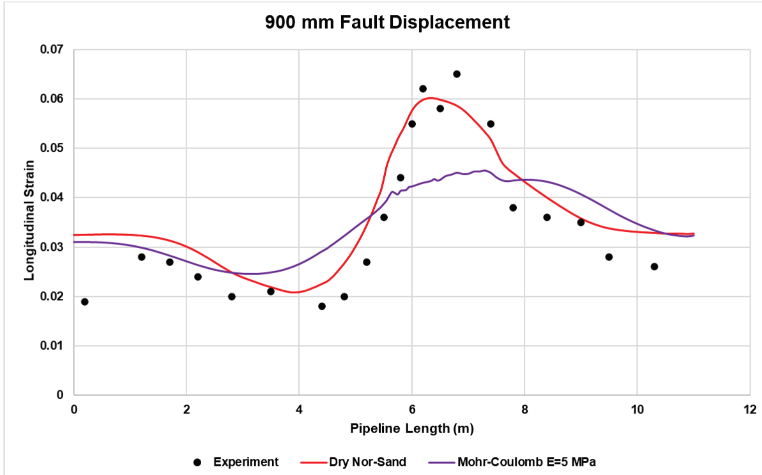

Figure 80: Strain distribution at a fault displacement of 900 mm

It is essential to acknowledge that the Nor-Sand Critical State Model cannot entirely replicate the actual soil behavior employed in the test. Consequently, even with the finite element model using the Nor-Sand Critical State Model, some disparities with the experimental data persist. Nevertheless, overall, a more advanced model proves beneficial in representing soil behavior and contributes to producing more accurate results.

4.4.4.2 Small-Scale Analysis

Utilizing the validated finite element model of soil-pipeline interaction during fault movement, various parameters concerning the fault, pipeline, and soil have been chosen for further analysis. The aim is to examine the distribution of pipeline strain under specific conditions and ultimately develop a prediction model capable of directly providing pipeline strain distribution. Initially, the study concentrates on a smaller geometry measuring 12 m by 12 m. The depth of the model was adjusted according to the diameter and burial depth of the pipeline. The pipeline material is another crucial aspect to incorporate. The validated finite element model is founded on HDPE pipe based on the physical experimental data from full-scale experiments carried out at Cornell University (O'Rourke et al., 2008). Once the model performance is verified, various steel materials commonly utilized in the gas and oil industry will be examined.

The primary parameters chosen for the strike-slip fault movement are its crossing angle and the amount of fault displacement. Initially, the study focuses on the 65° case, which was utilized in the validation model, before considering other fault crossing angles. The mesh of the soil body and the pipeline (marked in red) utilized for the analysis is shown in Figure 81. Like in the previous analysis, fine mesh is adopted around both the pipeline and the fault area. Figure 82 shows the deformed mesh at 1.2 m fault displacement.

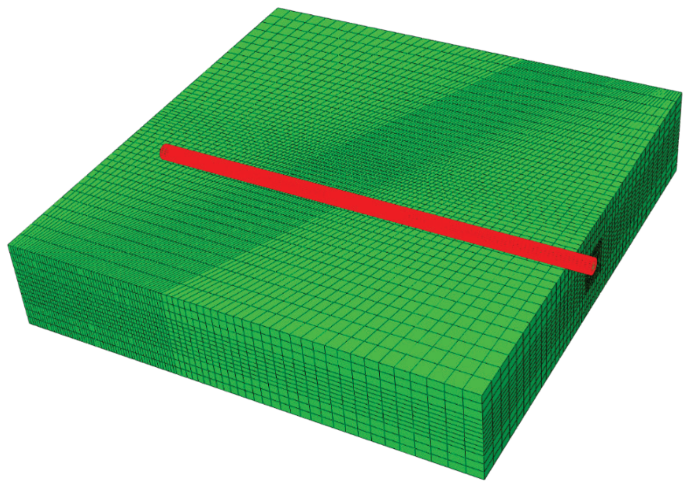

Figure 81: Mesh for analysis

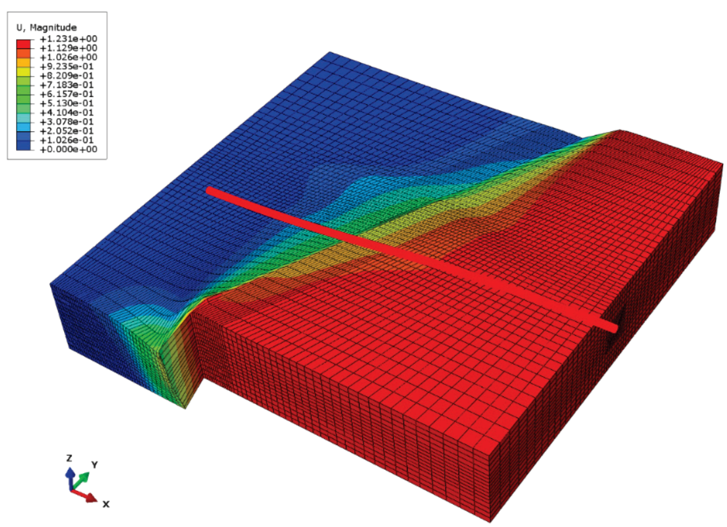

Figure 82: Deformed mesh

Figure 83 depicts the longitudinal strain distributions of a 200-mm steel pipeline with a 12-mm thickness across different fault displacement values for the 65° fault. Bending behavior is observed in the pipeline, accompanied by elongation. Additionally, as the fault movement values increase, the longitudinal strain also increases. It becomes evident that as the fault displacement rises, the elongation of the pipe along the axial direction emerges as the primary factor contributing to the increase in pipe strain, whereas the bending strain of the pipeline diminishes in significance concerning the overall longitudinal strain.

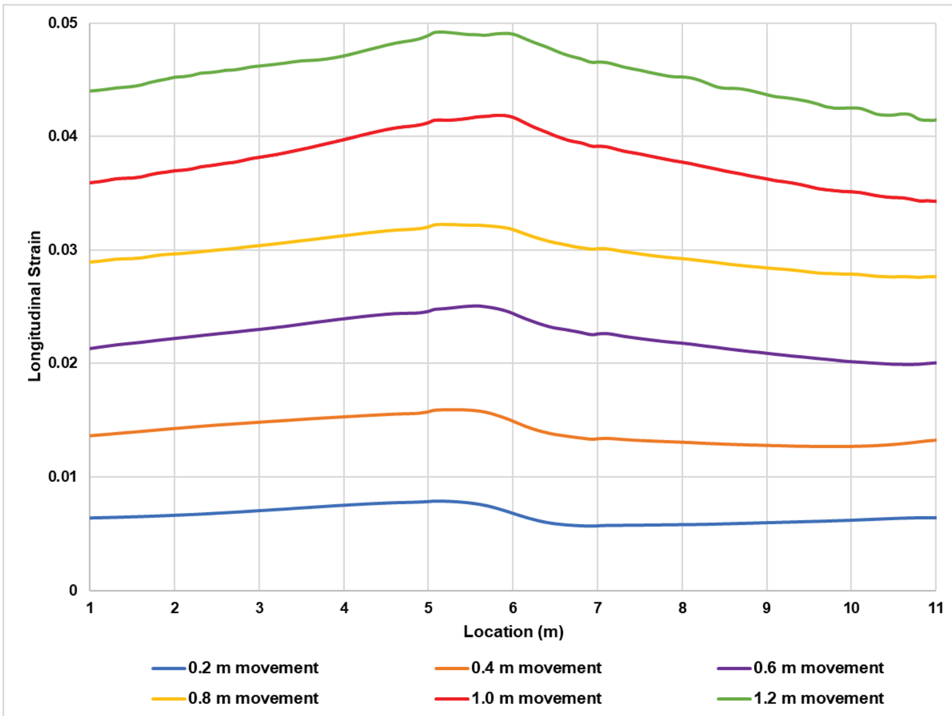

Figure 83: Strain distribution across various fault displacements

The selection of representative soil parameters is pending. While various soil constitutive models employ different soil parameters, the objective is to identify parameters that are readily accessible and widely employed in engineering practices. This approach aims to facilitate the ease of use of the future prediction model.

The pipeline diameter range has been chosen from 89 mm (3.5 inches) to 1066 mm (42 inches). A specific number of pipeline diameter falling within this range and conforming to standard sizes will be selected for the analysis, with the exact quantity to be determined. Correspondingly, the diameter-to-wall thickness ratio is set within the range of 7 to 64, adhering to a reasonable value based on engineering practice. The study focuses on the cases with shallow burial depths for the pipeline, excluding very deep burial scenarios. The range under consideration for investigation spans from 0.6 m to 1.8 m.

Figure 84 compares the longitudinal strain distribution of the 200-mm pipeline across different wall thicknesses. The solid line corresponds to the 12 mm wall thickness case, while the dashed line represents the 6 mm wall thickness. As expected, thinner walls imply less resistance to fault movement, resulting in larger strain, particularly in the vicinity of the fault plane. As the fault displacement increases, the disparity in strain within the central region also expands.

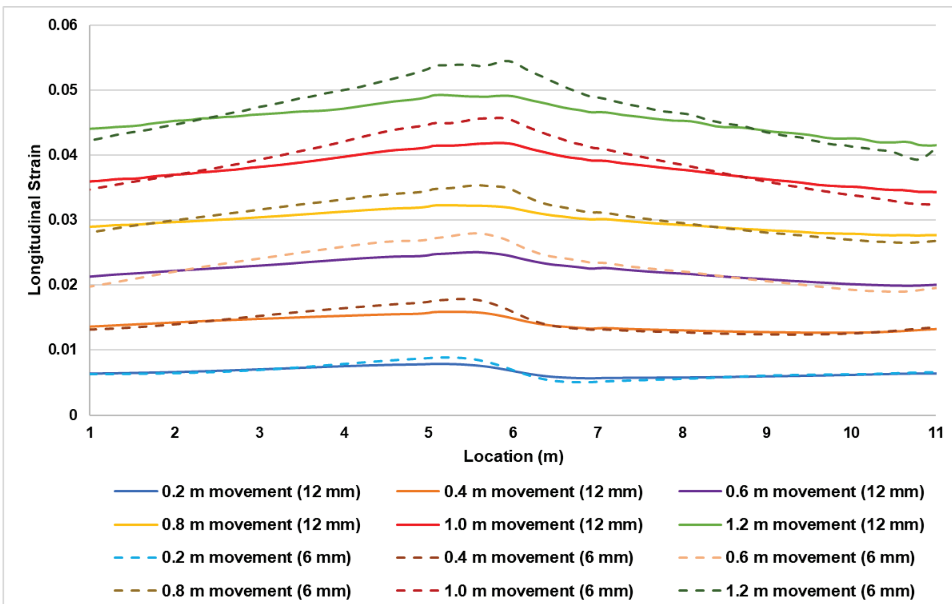

Figure 84: Strain distribution with varying wall thickness

Figure 85 presents a comparison of the strain distribution at various burial depths for a 200-mm diameter pipeline at each fault displacement value. The solid line denotes the burial depth of 1.2 m, whereas the dashed line signifies the burial depth of 1.6 m. It is evident that deeper burial depths result in larger strain and greater strain variation. When the fault displacement is small, the primary difference in strain distribution occurs in the central 4-meter region, with strains at other locations being similar. However, as the displacement increases, the region of strain difference becomes larger, ultimately leading to a distinct strain distribution across the entire pipeline.

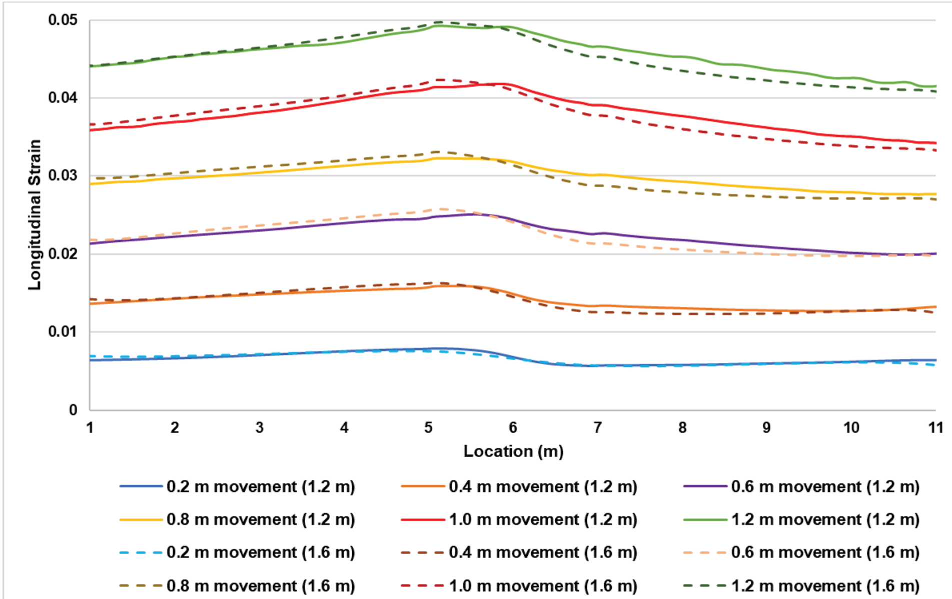

Figure 85: Strain distribution with different burial depth

4.4.4.3 Large-Scale Soil-Pipeline Interaction Analysis

Previous numerical simulations of soil-pipeline interactions have predominantly focused on small-scale cases due to limitations in computational power and lengthy computation times. Furthermore, these simulations have often relied on simplified soil-spring models. Experimental studies, typically conducted at small scales, have also been constrained by the limited length of the pipeline. However, real-world pipelines span much longer continuous lengths between fixed points than those tested in laboratories. With advancements in computational capabilities, it is now feasible to conduct large-scale soil-pipeline interaction analyses using 3D continuum models, allowing for the consideration of three-dimensional effects. Moreover, these analyses are less constrained by boundary assumptions inherent in small-scale simulations and are more representative of the conditions encountered by buried pipelines in situ. Such modeling efforts provide valuable insights into the strain distribution along continuous pipelines, offering enhanced understanding and actionable information for engineering design and decision-making processes.

4.4.4.4 Finite Element Model Description

The size of the model for the pipeline crossing the fault has changed, which is 800 m long, 400 m and 20 m high. The crossing angles between the pipeline centerline and the fault trace used for the recent analyses were 75° and 70°. In order to make the two pipeline ends reach the soil side surfaces, the total length of the pipeline became 828 m and 851 m respectively. The diameter of the pipeline was 0.6096 m (24 inches). The burial depth (from the top to the pipe centerline) was 1.6 m. The geometry of the two models is shown in Figure 86.

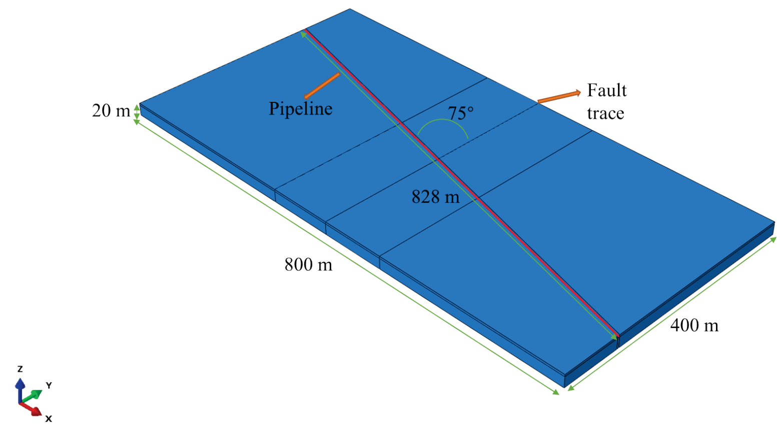

(a) 75° fault crossing angle case

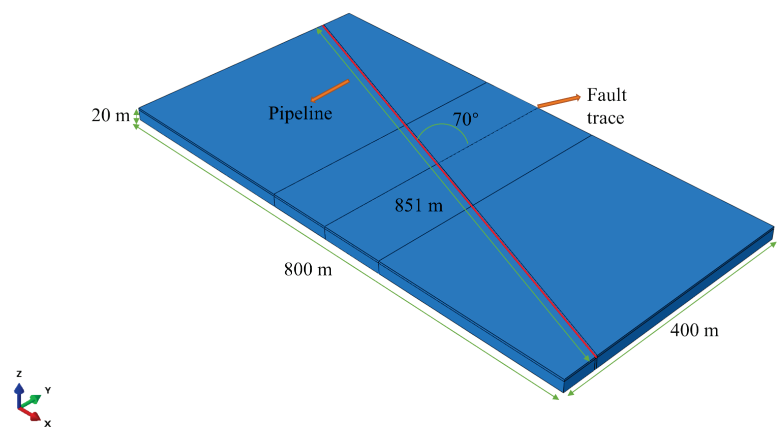

(b) 70° fault crossing angle case

Figure 86: Model geometry of large-scale analysis

In terms of the boundary conditions, the bottom of the soil body was fixed in the vertical direction. Both halves of the soil body were forced to move 1.5 m in the opposite direction to create fault displacement of up to 3 m. Lateral earth pressures changing with the depth were applied to the soil side surfaces perpendicular to the moving direction to better represent the in-situ stress field situation. Figure 87 shows the boundary conditions for the 75° fault crossing angle model.

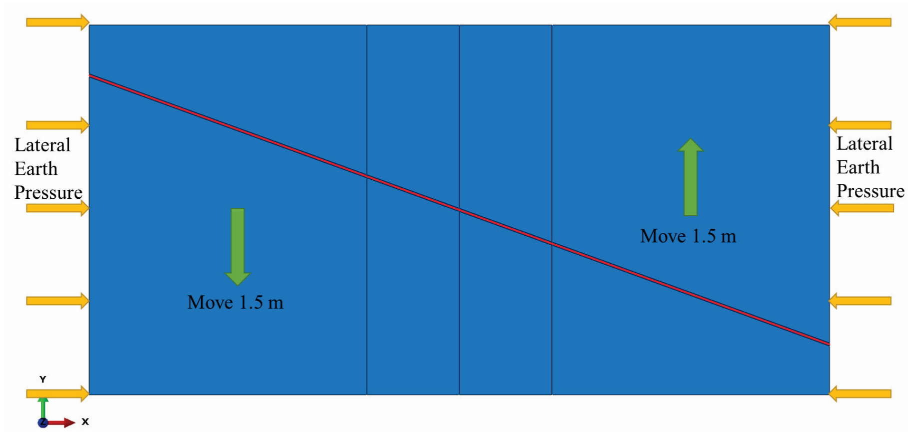

Figure 87: Schematic diagram of boundary conditions

The mesh for the pipe and the soil body has been modified to keep the meshing and elements relatively uniform in different models with different crossing angles. In the circumferential direction, the pipeline was divided into 32 parts, as in the previous models. In the longitudinal direction, the center 200-meter region had a finer mesh, and the average element size was about 0.2 m by 0.05 m. For the two end parts that were both 300 m long, they had a relatively coarser mesh, and the average element size was about 0.35 m by 0.05 m. A total of 121,600 elements were generated for the pipeline part. And the mesh for the 24-inch steel pipeline is shown in Figure 88. The element type for the pipeline was S4R, a 4-node doubly curved thin shell with reduced integration, hourglass control, and finite membrane strains. 5 thickness integration points were selected.

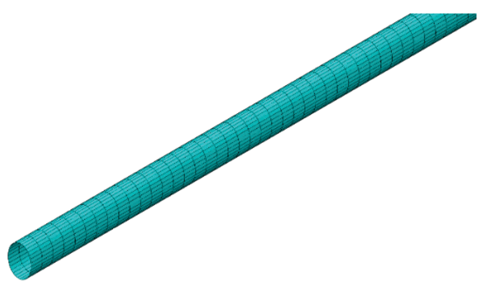

Figure 88: Mesh for the 24-inch pipeline

As shown in Figure 89, for meshing the soil body, the basic idea is to use finer mesh for the region near the fault trace and the pipeline. Therefore, in the center 200-meter region, the element length was around 0.5 m. For the other parts away from the fault trace, the average element length was around 2.5 m. Looking at the cross section, the elements surrounding the pipeline had an average size of 0.25 m by 0.25 m. A total of 5,399,040 elements were generated for the soil part in the 75° model, whereas a total of 5,422,240 elements were generated for the soil part in the 70° model. The element type for soil was C3D8R, an 8-node linear brick with reduced integration and hourglass control.

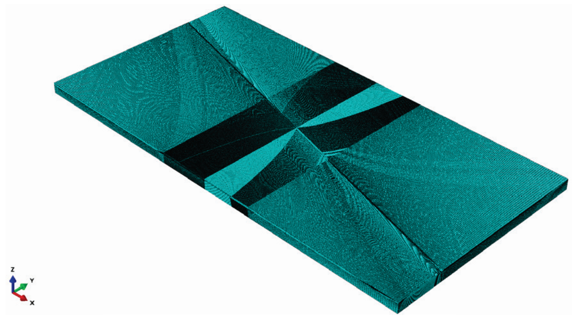

Figure 89: Mesh for soil body (75° fault crossing angle model)

The pipeline material was assumed to be API 5L X52, commonly used in the gas pipeline industry. Its behavior was represented by a piecewise-linear stress versus an engineering strain curve based upon a generic Ramberg-Osgood formulation ($\varepsilon = \frac{\sigma}{E}(1 + \frac{n}{1+r}(\frac{\sigma}{\sigma_y})^r)$). Its yield stress ($\sigma_y$) was 359 MPa. For API 5L X52, n was 9 and r was 10. The Young's Modulus (E) was assumed to be 200 GPa, whereas the Poisson's Ratio was set to be 0.3. Its density was 7.85 g/cm^3.

For the soil-pipeline interaction, the contact in the normal direction was set as hard contact, which means there was no overclosure taken into account. In the tangential direction, different friction coefficients between soil and pipeline were used to study the effect since the friction coefficient will depend on the coating. Therefore, the values of 0.3, 0.4, and 0.5 were used.

For the scenarios involving fault crossing angles of 75° and 70°, the Mohr-Coulomb Model was employed. The soil type was considered to be sand, with a total unit weight of 18 kN/m^3. The Young's Modulus was specified as 4 MPa, while the Poisson's Ratio was set at 0.3. In terms of plasticity, an internal friction angle of 37° and a dilation angle of 6° were utilized. Furthermore, a lateral coefficient of 0.4 was applied to establish the initial geostatic conditions for determining the lateral earth pressure.

4.4.4.5 Results

The computed lateral displacement profiles are illustrated in Figure 90 and Figure 91. In Figure

90, representing the 75° case, noticeable lateral displacement changes, denoted by the curved section in the plot, occur consistently across all fault displacement stages within the region spanning from Location -25 m to Location +25 m. This segment extends approximately 50 m in length, constituting approximately 1/16 of the total pipeline length. Similarly, Figure 91 depicts the lateral displacement profiles for the 70-degree case, revealing significant lateral displacement changes within the range from Location -20 m to Location +20 m. This portion spans approximately 40 m in length, equivalent to approximately 1/20 of the total pipeline length. The remainder of the pipeline moves in conjunction with the soil.

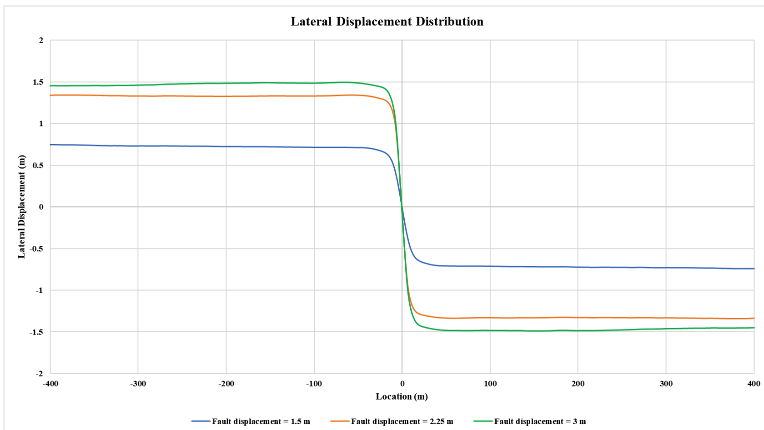

Figure 90: Lateral displacement distribution of the 24-inch pipeline (75° case)

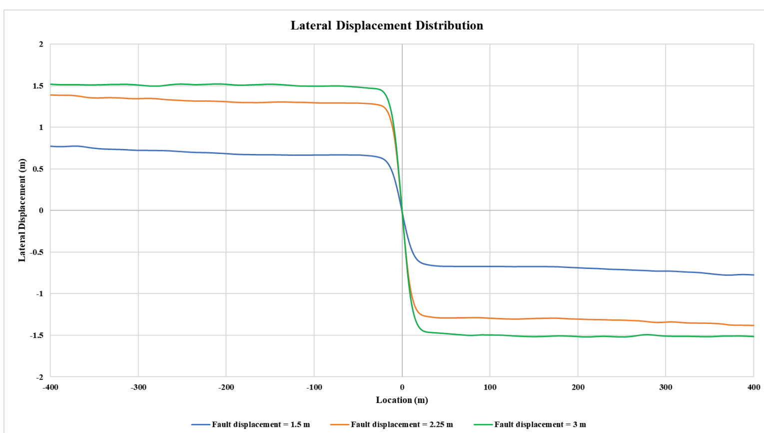

Figure 91: Lateral displacement distribution of the 24-inch pipeline (70° case)

The longitudinal strain distributions along one side of the spring line of the 24-inch pipeline at various fault displacement stages are depicted in Figure 92 and Figure 93. These plots hold significant importance for the distributed fiber optic strain monitoring project, as the monitored distributed strain data will be compared to the computed values. In the case of the 75° fault angle, the center 50-meter region exhibits noticeable strain changes during fault movement, correlating with the lateral displacement distribution previously discussed. Despite substantial fault displacement, most of the pipeline predominantly demonstrates compressive strain, with only a small portion experiencing localized tensile strains. Conversely, for the 70° fault angle, when the fault displacement reaches 1.5 m, the majority of the pipeline remains under compression. However, at a fault movement of 2.25 m, most sections of the pipeline exhibit strains close to 0. As the fault displacement continues to increase, the elongation behavior of the pipeline increasingly dominates the longitudinal strain, resulting in compression primarily occurring in a small segment of the pipeline. This contrasts with the observations from the 75° case.

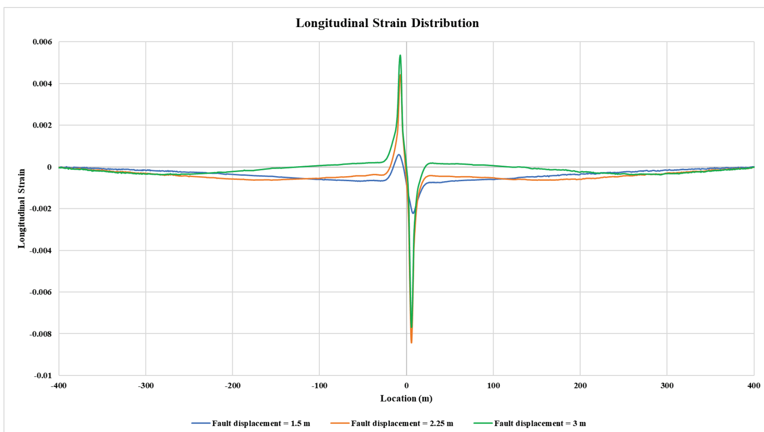

Figure 92: Longitudinal strain distribution of the 24-inch pipeline (75° case)

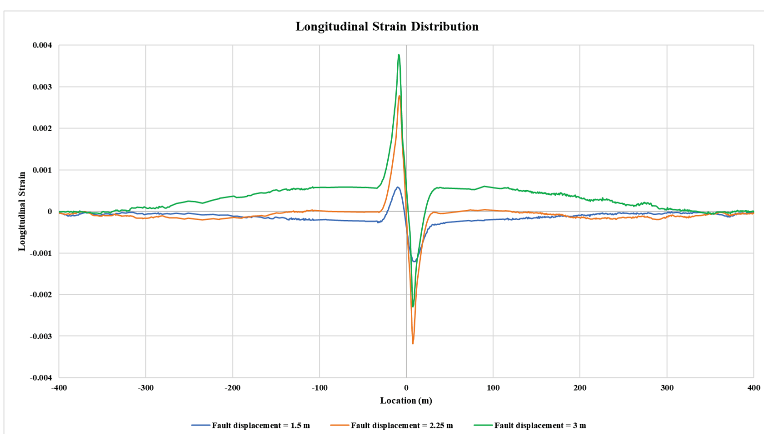

Figure 93: Longitudinal strain distribution of the 24-inch pipeline (70° case)

In the case of cohesionless material like sand, the longitudinal resistance to the pipe movement is due to friction interaction at the soil-pipe interface as a function of the interface angle of friction between pipe and soil and of the normal pressure. The interface angle of friction between pipe and soil is directly proportional to the internal friction angle, according to a coating-dependent factor $f \leq 1$. Suppose the outer surface of the pipeline is very rough. In that case, slippage occurs at the soil-pipeline interface, directly beyond the soil-pipeline interface, and effective friction angle δ is equal to the soil friction angle ϕ $(f = 1)$. Otherwise, if the external pipe surface is smooth, the slippage occurs at the soil-pipeline interface with an effective friction angle δ less than the soil friction angle ϕ $(f < 1)$. Table 5 lists the values of f reported in the ALA 2001 guidelines.

Table 5: Friction factor f for various external coatings (ALA 2001)

Pipe Coating	Friction factor f
Concrete	1.0
Coal Tar Coating	0.9
Rough Steel	0.8
Smooth Steel	0.7
Epoxy Coated Polyethylene	0.6

Different friction coefficients (including 0.3, 0.4, and 0.5) are used in this study to examine the effect on pipeline strain distribution. The longitudinal strain distributions along one of the spring lines of the 24-inch pipeline with different soil-pipeline friction coefficients are shown in Figure 94 when the fault displacement is 3 m. As the friction coefficient changes from 0.5 to 0.3, the longitudinal strain distribution does not exhibit a noticeable change. Even for the center 70-meter region where large strains are developing, their distributions are similar. Only peak tensile and compressive strains are slightly different.

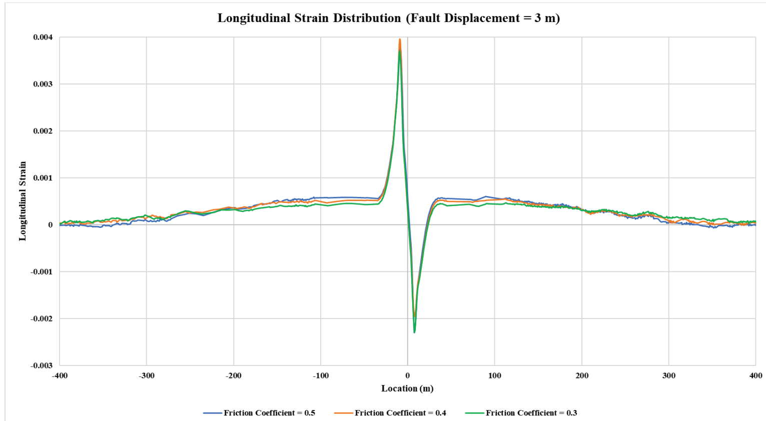

Figure 94: Longitudinal strain distribution for different friction coefficients (fault displacement = 3 m)

It is noted that the actual friction coefficient may have a wider range compared to the range examined in these simulations. For example, when the soil friction angle ϕ is 37°, with the coating coefficient f changing from 0.6 to 1.0, the corresponding friction coefficient which equals to $\tan f\phi$ will change from 0.4 to 0.7. Therefore, more simulations (e.g., 0.5 to 0.7) will be conducted to determine the effect resulting from the different friction coefficients.

4.4.4.6 Comparison of Different Constitutive Models

Afterwards, a fault crossing angle of 90° case was investigated to compare the results obtained using different soil constitutive models, namely the Mohr-Coulomb Model and the Nor-Sand Critical State Model. The soil parameters used in the finite element analysis using the Nor-Sand Model are shown in Table 6.

Table 6: Soil parameters in the Nor-Sand Model

Parameter	Value
Critical stress ratio in triaxial compression	1.39
Maximum void ratio	0.705
Minimum void ratio	0.393
Initial void ratio	0.548
Value of N in Nova's flow rule	0.2
Hardening modulus	400
Shear modulus multiplier	1200
Pressure exponent	0.5

Poisson's ratio	0.35
Maximum dilation coefficient	3.9

Figure 95 illustrates the various shapes of the deformed pipeline at different stages of fault movement, based on the given Nor-Sand Model parameters. As depicted in the figure, the middle segment of the pipeline undergoes progressive deformation in response to the growing fault displacement.

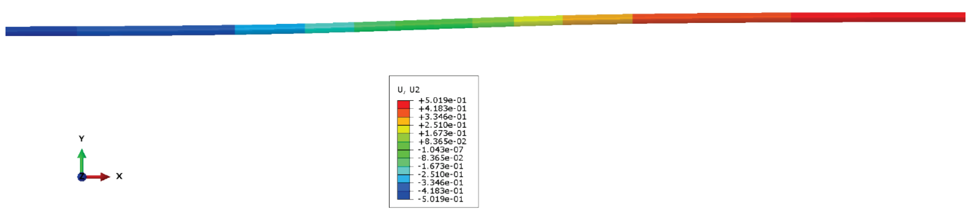

(a)

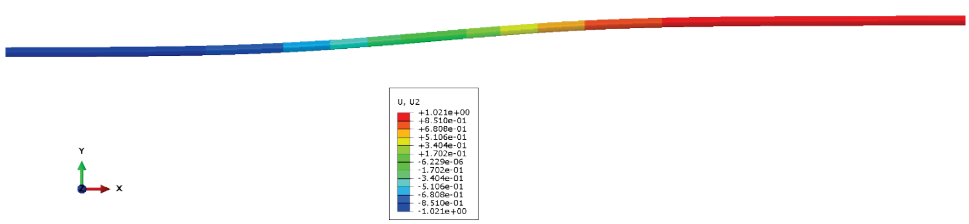

(b)

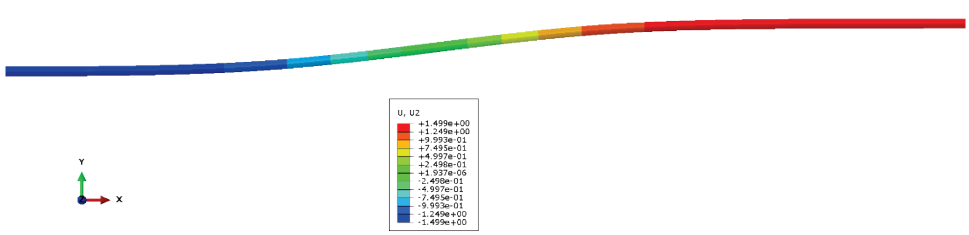

(c)

Figure 95: Deformed pipeline shapes at different fault movement stages: (a) 1 m; (b) 2 m; (c) 3m (90° case with Nor-Sand Model)

Figure 96 shows the lateral displacement patterns of the pipeline at various stages of fault movement. In the majority of pipeline sections, the lateral displacement corresponds directly to the magnitude of the applied soil displacement, with values typically ranging from 0.5 m to 1.5 m. As shown in Figure 97, it can be observed that throughout all stages of fault displacement, a distinct change in lateral displacement occurs at a specific region depicted as the curved segment on the plot. This region spans from Location -20 m to Location +20 m, including a length of approximately 40 m. Notably, this range represents approximately 1/20 of the overall length of the pipeline.

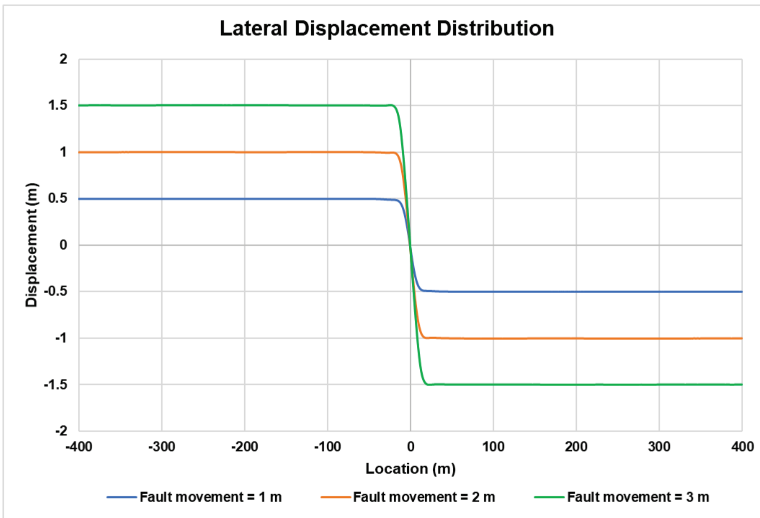

Figure 96: Lateral displacement distribution of pipeline (90° case with Nor-Sand Model)

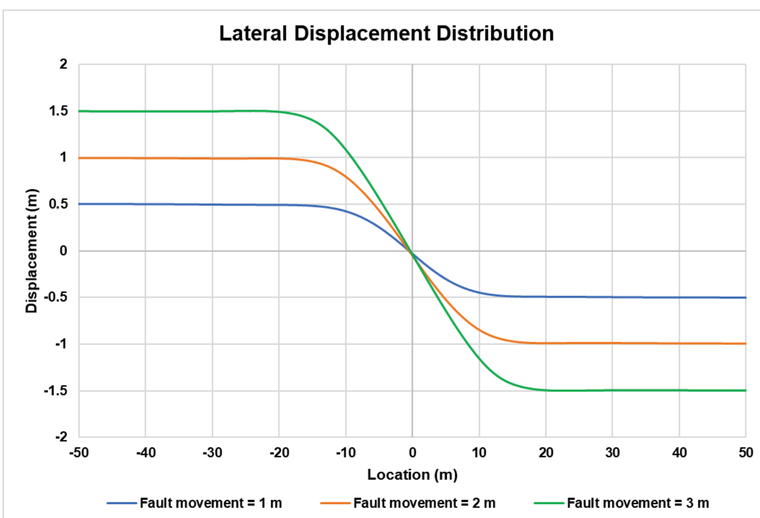

Figure 97: Lateral displacement distribution of pipeline in the center 100-m area (90° case with Nor-Sand Model)

Figure 98 shows the longitudinal strain distributions (at one of the spring lines) observed at various stages of fault movement. The axial elongation effect of the pipeline becomes increasingly prominent as fault displacement increases, resulting in predominantly tensile strain in most sections of the pipeline. The strain value for the majority of the pipe remains below 0.001. At a distance of 25 m from the fault plane, there is a noticeable and quick change in the strain of the pipeline. It is noteworthy that the locations of the highest tensile and compressive strains undergo direct alterations during fault displacement. The individuals progressively move closer to the fault plane. When a displacement of 1 m occurs, the location of maximum tensile longitudinal strain and maximum compressive longitudinal strain can be observed approximately 7 m away from the fault plane. When the displacement reaches a magnitude of 2 m, the locations of the maximum tensile longitudinal strain and the maximum compressive longitudinal strain undergo a shift, moving to approximately 10 m away from the fault plane. When the displacement reaches a magnitude of 3 m, the locations of the highest tensile longitudinal strain and the highest compressive strain shift to approximately 12.5 m from the fault plane.

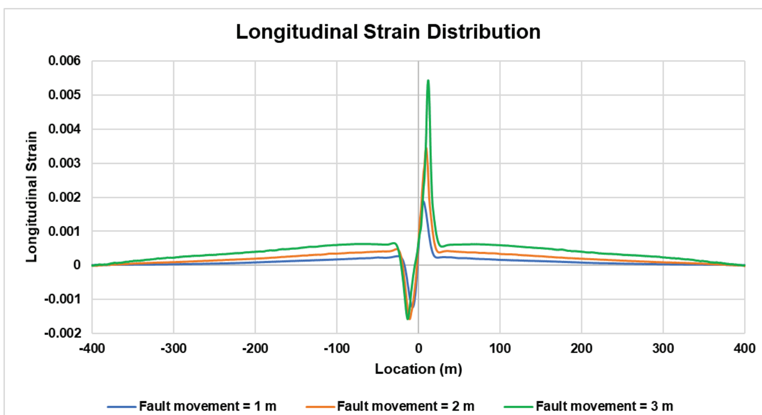

Figure 98: Longitudinal strain distribution of the pipeline (90° case with Nor-Sand Model)

The bending strain can be determined by analyzing the longitudinal strain at the spring lines situated on both sides of the pipeline. Figure 99 illustrates the distribution of the bending strain along the pipeline. Throughout most of the pipeline, the magnitude of the bending strain is nearly negligible. In a similar vein, substantial bending strains arise at a distance of 25 m from the fault plane. The observed maximum bending strain is around 0.003. Additionally, there is a shift in the location of the maximum tensile and compressive bending strain. The locations observed at various stages of fault displacement exhibit similarities to the locations of the highest longitudinal strain.

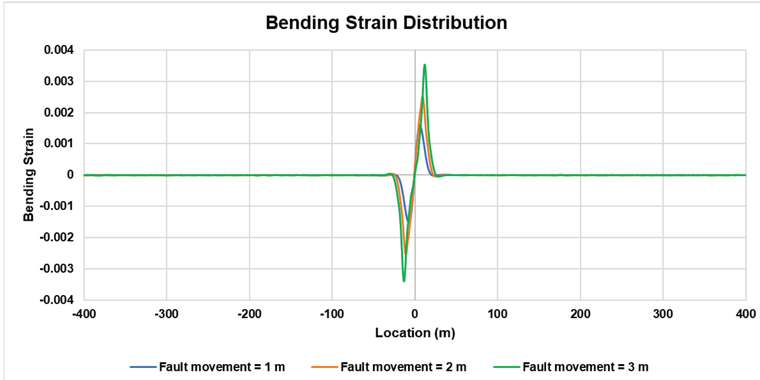

Figure 99: Bending strain distribution of the pipeline (90° case with Nor-Sand Model)

The calculation of axial strain, which is the strain resulting from the elongation of a pipe, involves subtracting the bending strain from the longitudinal strain. The axial strain distribution exhibits a high degree of symmetry in relation to the fault plane, as illustrated in Figure 100. The axial strain value increases as the proximity to the fault plane increases. Simultaneously, in the scenario where the intersection angle is 90°, the magnitude of the axial strain is relatively small, and its influence on the longitudinal strain is less significant compared to the bending strain. At various stages of fault displacement, two distinct locations will exhibit the highest axial strain values, namely, the location of maximum tensile longitudinal strain and the location of maximum compressive longitudinal strain.

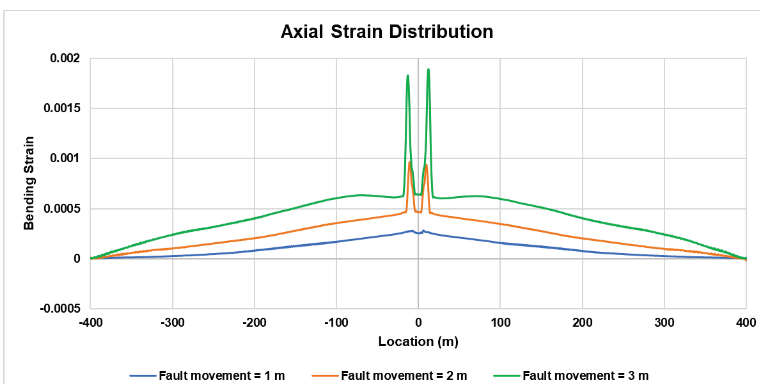

Figure 100: Axial strain distribution of the pipeline (90° case with Nor-Sand Model)

The longitudinal strain distributions, bending strain distributions and axial strain distributions are then compared with the results from previous Mohr-Coulomb Model.

In contrast, it can be observed that during all stages of fault displacement, the Nor-Sand Model demonstrates higher levels of bending strain and axial strain, consequently resulting in more longitudinal strain as well. Additionally, the locations of maximum strain exhibit modest variations. The Nor-Sand Model yields a maximum strain position that is approximately 1.5-2 m further from the fault plane compared to the position determined by the Mohr-Coulomb Model. The comparisons of the longitudinal strain, bending strain and axial strain between Nor-Sand Model and Mohr-Coulomb Model at a fault displacement of 1 m are shown in Figure 101, Figure 102 and Figure 103 respectively..

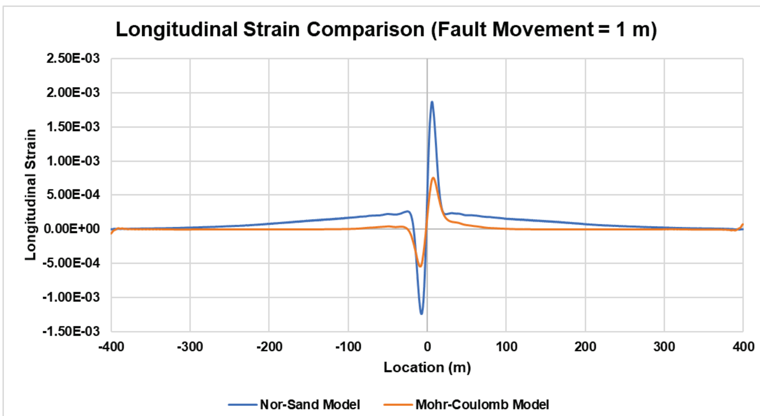

Figure 101: Longitudinal strain distribution comparison at a fault movement of 1 m (90° case)

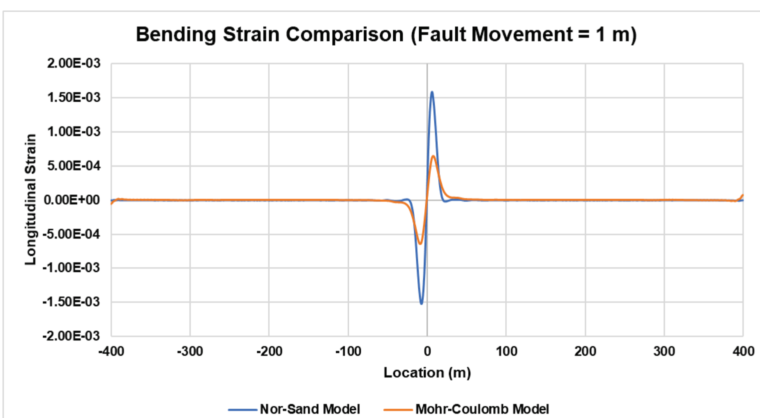

Figure 102: Bending strain distribution comparison at a fault movement of 1 m (90° case)

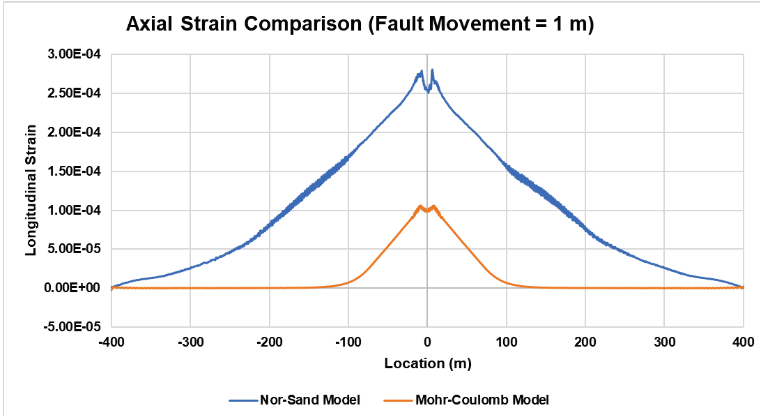

Figure 103: Axial strain distribution comparison at a fault movement of 1 m (90° case)

The comparisons of the longitudinal strain, bending strain and axial strain between Nor-Sand Model and Mohr-Coulomb Model at a fault displacement of 3 m are shown in Figure 104, Figure 105 and Figure 106 respectively.

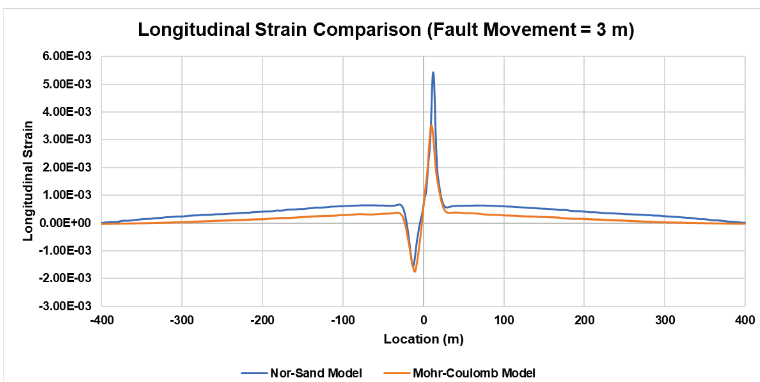

Figure 104: Longitudinal strain distribution comparison at a fault movement of 3 m (90° case)

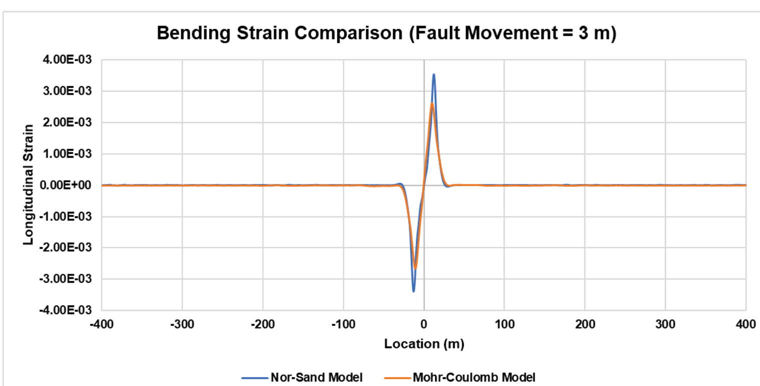

Figure 105: Bending strain distribution comparison at a fault movement of 3 m (90° case)

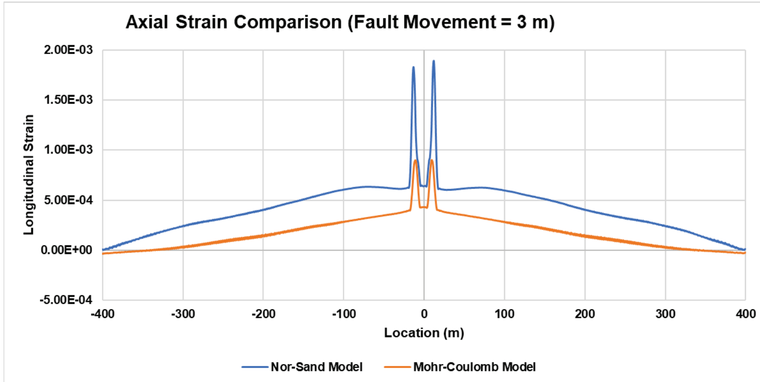

Figure 106: Axial strain distribution comparison at a fault movement of 3 m (90° case)

For all three strains, it is shown that regions with higher strain values exhibit a correspondingly substantial difference in the strain values obtained from the two models. In a region characterized by low strain values, the difference between the strain values obtained from the two models is comparatively insignificant. The Nor-Sand Model consistently produces a bending strain value that is approximately 1000 $\mu\varepsilon$ higher than the bending strain value obtained using the Mohr-Coulomb Model. As the magnitude of fault displacement rises, there is a corresponding increase in the difference of axial strain. In the majority of pipeline regions, the Nor-Sand Model generates an axial strain that is roughly 90 $\mu\varepsilon$ higher than the axial strain obtained by the Mohr-Coulomb Model, given a fault displacement of 1 m. When the fault displacement reaches a magnitude of 3 m, the axial strain calculated using the Nor-Sand Model exhibits an increase of around 250 $\mu\varepsilon$ compared to the axial strain calculated using the Mohr-Coulomb Model.

The observed disparity in strain outcomes suggests that the utilization of a more sophisticated soil constitutive model leads to a more intricate plastic deformation mechanism of the soil during fault displacement. Consequently, the plastic strain experienced by the soil is amplified, thereby exerting a more substantial influence on the pipeline.

4.5 Commercialization plan

4.5.1 Smart Infrastructure market

In recent years, the Internet of Things (IoT) has brought new technologies related to sensors and communication, integrating them into various business sectors. These emerging technologies include distributed fiber optics sensing, wireless sensor networks, low power miniature sensors, energy harvesting for continuous monitoring, robotic inspections, satellite images, A.I. and machine learning, digital twin technologies, etc. These technologies, along with the methodologies that stem from them, have the potential to enhance the resilience of infrastructure systems and optimize their performance throughout their operational life, while also reducing the need for human resources in the field and improving workforce safety (Soga and Schooling, 2016; Soga, 2023).

The current global infrastructure investment is about $2.8 trillion per year, and it is expected to grow to $3.5-4.5 trillion per year by 2040 (Global Infrastructure Hub, 2021). The $1.2 trillion federal infrastructure bill is expected to boost the U.S. infrastructure industry over the next decade. Despite this, the industry's annual productivity growth has only been 1% over the past 20 years (McKinsey Global Institute, 2017). However, digitization is currently transforming the industry to increase its productivity. Specific actions being taken include reshaping regulation, rethinking design, improving procurement and supply chain, reskilling workers, and using technology and innovation. Our success will be part of this digital transformation happening in our industry. We identify our market as the infrastructure sensing market, which is expanding as part of smart cities and infrastructure initiatives.

The current global market size of Structural Health Monitoring is about $2.0 billion, with a high CAGR value of 14% (e.g., Marketsandmarkets, 2022). The industry segments include security, railways, roads, asset condition monitoring, power systems, and geophysics. We participated in the national I-Corps program organized by the National Science Foundation to explore opportunities for a new low-cost distributed fiber optic sensor technology that reduces reading time and provides dynamic detection capability for strain or temperature measurements (National Science Foundation Award #1931704, I-Corps: Dynamic Distributed Fiber Optic Sensor System). We examined the commercial opportunities for this new technology and promoted it as part of engineering design and decision-making processes.

4.5.2 Market demand on DFOS

Our I-Corps team conducted interviews with 104 potential clients, stakeholders, and key business adopters to gain a deeper understanding of the monitoring needs and current areas for improvement within the marketplace. Additionally, we attended I-Corps training sessions. Initially, we believed that the lack of data was a major challenge for engineers and asset managers, and that more data would provide more value. However, through the interviews and I-Corps exercises, we discovered that more data is not always better, especially when it is unclear how to use it. Currently, the infrastructure is designed to minimize risk, so there is little motivation to take risks. Our project focused on customer discovery, linking customer segments to those who bear the risk. We found that the ecosystem is complex, as the owners and funders of an infrastructure asset must interact with numerous organizations, including design engineers, regulators, inspectors, construction contractors, instrumentation and monitoring contractors, and asset managers/concessionaires.

In interviews and during the I-Corps evaluation exercise, it was discovered that multiple agencies are interested in teaming up with the commercialization of this DFOS technology. The evaluation also highlighted the need for more deployment and education to raise awareness about the technology. Subsequently, the team has been working on developing the technology in partnership with both public and private agencies. For instance, in a recently completed NSF project (Award # 1741042, Deformation Induced Soil Fracturing - Multi-Scale Multi-Physics Mechanism and Early Detection), we collaborated with the USACE Sacramento Division to install the DFOS sensor system in a cement-bentonite seepage cutoff wall during the retrofit construction of a river levee in Sacramento, CA. The primary goal is to monitor the long-term performance of the levee, particularly how it is affected by seasonal changes in the river level.

Our experience with these organizations has helped us understand that our advantage lies in our ability to provide a low-cost technology solution supported by industry knowledge of infrastructure and construction processes. By collaborating directly with industry owners who embrace the concept of smart infrastructure, we are developing engineering decision methodologies and tools that will make use of distributed sensing data. The ultimate goal of this research proposal is to significantly enhance our capability to predict and manage the life expectancy of large infrastructure by actively monitoring operational processes. We believe that the DFOS technology will play a significant role in achieving this due to its unique characteristics (distributed, inexpensive, and long-life).

4.5.3 Plan

In September 2023, we received a new commercialization project called "Long-range Dynamic Distributed Strain Sensing System for Smart Infrastructure Monitoring" from the Partnerships for Innovation (PFI) program of the US National Science Foundation. Our DFOS system design was granted a U.S. Patent US10677616B2 in June 2022, under the administration of UC Berkeley's Office of Intellectual Property and Industry Research Alliances (IPIRA). Currently, we are using custom, hand-made prototypes that cannot be mass-produced efficiently. In this PFI project, our goal is to develop a design that can be mass-produced and has a commercial-quality user interface software by the end of the award period. The project consists of three work packages: (a) development of digitization hardware for a low-cost, mass production system, (b) integration of a cloud-based data processing system for more efficient data acquisition and interpretation, and (c) demonstration of an online digital twin model for real-time engineering analysis.

During the project, we and our collaborators realized that the benefits can only be assessed when the owner regularly reviews the data and evaluates its quality to improve the reliability of their risk assessment. While there is a sprint of monitoring infrastructure against ground hazards, the value can only be accurately assessed once we have several years of data. We have now secured funding for a new project from the California Energy Commission, allowing us to continue monitoring this site for the next three years. Following this, we will be able to conduct a proper cost-benefit analysis.

We are planning to organize a series of workshops to fine-tune the application domain of the innovative DFOS technology. The fieldwork studies will involve owners, operators, designers, and engineers. The engagement workshops will aim to identify stakeholder interests and questions related to the work packages associated with each field study. Concurrently, research steering workshops will be held in the form of sandpits with research partners to compare tools and develop dissemination activities. Comparing different analysis tools and paradigms will provide new perspectives on framing the problem. By combining curiosity-driven and outcome-driven approaches, we aim to deliver scientific benefits and enhance engagement.

In order to commercialize innovations effectively, it is essential to cultivate a workforce capable of implementing these advancements. We plan to create best practice guidelines and training programs to support the full realization of the potential of new technologies. Providing training to understand the benefits and opportunities that new technologies offer is crucial for changing traditional mindsets. Recognizing the significant differences between innovation leaders and followers in the construction and infrastructure sector, we plan to offer various courses at different levels. For example, we will conduct courses for 'training of trainers' for new technologies, which will enable the dissemination of innovation to companies that typically adhere strictly to standards and norms in their business. Additionally, we will organize executive courses to cultivate new young leaders with diverse perspectives and capabilities. The objective is to equip the future industry leaders with the latest technical and managerial skills, thereby enhancing the performance, efficiency, and sustainability of the construction sector while fostering innovation and the adoption of new technologies.

5 CONCLUSIONS

The steel pipe four-point bending experiment demonstrated that the selected fiber optic sensor, which features a robust protective layer and high accuracy, combined with the proposed attachment method—initially using an appropriate adhesive, followed by wax tape, and finally an outer wrap—ensured excellent deformation coordination with the monitored pipeline. This setup allowed the fiber optic sensor to capture the complete strain distribution at all locations during the loading process without damaging the pipeline. Subsequent finite element modeling, incorporating improved boundary conditions, produced similar strain distribution patterns at each loading step, thereby validating the experimental data from distributed fiber optic sensing.

Using the tested installation method and fiber optic sensor type, the project successfully installed distributed fiber optic strain sensors on a replaced steel gas pipeline. With these sensors installed at three locations (the crown and two sides), it was possible to monitor strain changes in the pipeline since August 2023. Precision error analysis indicated an error margin of less than 20 $\mu\varepsilon$. In addition, by utilizing the data obtained from a fiber optic temperature sensor installed in the trench, it was possible to observe minor monthly changes in strain (usually less than 100 $\mu\varepsilon$). These changes corresponded to the thermal expansion and contraction of the steel caused by temperature fluctuations throughout the monitoring period. The noted variations in strain were attributed to the substantial rains experienced in January and February of 2024.

The numerical simulation of the field conditions provided a strain distribution profile of the pipeline that is expected under imposed fault movement, which in turn aided in identifying the most vulnerable locations. Over the monitoring period, which has been less than one year, the total fault movement observed was significantly less than the design value, resulting in no severe strain changes observed along the pipeline.

Utilizing the test data-validated finite element model, both small-scale and large-scale soil-pipeline interaction simulations were conducted. The 3D continuum finite element modeling revealed that the peak strain location shifts with increasing fault displacement. Also the large-scale simulation indicated that, for a long continuous pipeline, the affected and curved region during fault displacement could extend to a considerable length, such as the central 50-meter section. These findings are important when examining the distributed strain profiles obtained in the field.

Employing a more advanced and comprehensive soil constitutive model, such as the Nor-Sand Model, in the finite element modeling of soil-pipeline interaction, yielded results that more closely align with experimental data. Additionally, such advanced modeling produced larger longitudinal, bending, and axial strain values compared to preliminary models, offering a more accurate representation of the pipeline's behavior under various loading conditions. These findings are useful when interpreting the distributed strain profiles obtained from the distributed fiber optic strain measurement system deployed in this study.

6 FUTURE WORK

6.1 Improvement of Fiber Optic Sensor Attachment Method

The current fiber optic cable attachment method is complex, involving multiple steps and utilizing adhesive materials with relatively high costs and long curing times. To improve efficiency and reduce installation time and labor, it is necessary to develop alternative adhesive materials that are cost-effective and require shorter curing times while maintaining strong attachment performance to ensure proper deformation coordination between the fiber optic cables and the pipeline. Such a task will aim to develop a simpler and more efficient attachment method. Laboratory tests and field deployments will be necessary to validate the performance of these alternative materials and attachment methods, ensuring their suitability for real-world applications.

Since any new technology can generate new hazards, the materials and methods used must be carefully selected and rigorously tested to guarantee that they do not compromise the integrity or functionality of the pipeline. This includes assessing factors such as chemical compatibility, mechanical stability, and long-term durability to minimize any risk of damage or degradation to the pipeline structure. By prioritizing pipeline safety in the development and deployment of improved attachment methods, it becomes possible to enhance monitoring capabilities while maintaining the integrity and reliability of the infrastructure.

6.2 Pipeline Real-Time Monitoring

Currently the field data acquisition for the pipeline is conducted regularly by the UCB team. This involves periodic visits to the site, typically on a monthly basis, to collect data on various parameters such as strain and temperature. While this approach provides valuable insights into the condition of the pipeline, it has several limitations, including the time and labor required for each site visit and the potential for not providing a real-time warning of residual strain development immediately after a geohazard event. Real-time monitoring saves time, reduces labor costs, and minimizes the risks associated with frequent travel to potentially remote or hazardous locations.

The next step in advancing our pipeline monitoring strategy is to develop and implement a real-time monitoring system. Such system will enable continuous data collection and transmission from the pipeline to a central monitoring station, thus providing immediate access to current conditions without the need for manual data collection. The core of this initiative involves the development of an accurate and low-power-cost Brillouin Optical Time Domain Reflectometry (BOTDR) analyzer. This development process encompasses several critical stages: (i) Conceptual Design, which defines the system's technical specifications and overall architecture; (ii) Component Selection and Prototyping, which involves selecting high-quality optical and electronic components and creating a prototype to test system interactions and performance; (iii) Optical System Integration, which ensures precise alignment and minimal optical loss; (iv) Signal Processing and Data Acquisition, which includes developing high-speed Analog-to-Digital Converters (ADCs) and Digital Signal Processing (DSP) units for real-time data analysis; (v) Software Development, which focuses on creating control software and data visualization tools; (vi) Calibration and Testing, which ensures the system's accuracy and reliability under various conditions; and (vii) Field Deployment and Feedback, which involves deploying the system in real-world environments and refining it based on practical insights.

The BOTDR analyzer currently developed at UC Berkeley can capture strain data within short data acquisition of less than one minute. During the site visit, it was possible to acquire the data within a short time, as potential for real time monitoring. However, it was not possible to showcase the real time monitoring capability because of the lack of continuous power supply. A key consideration for the current site is establishing a stable power supply for the BOTDR analyzer that does not harm the surrounding plants or animals. Potential solutions include utilizing renewable energy sources such as solar or wind power, deploying fuel cells, or designing a system with low power consumption to ensure sustainability and minimal environmental impact.

6.3 Improvement of Finite Element Modeling for Soil-Pipeline Interaction Analysis

While some finite element modeling analyses have incorporated advanced soil constitutive models, it is notable that certain simplifications are often implemented to align with the practical needs of engineering applications. There is an opportunity to leverage recently developed, more sophisticated soil constitutive models to enhance the accuracy of soil-pipeline interaction simulations. By adopting these advanced models, which offer a more comprehensive representation of soil behavior, it is possible to achieve a deeper understanding of the complex dynamics at play and improve the fidelity of our simulations.

In order to streamline computational processes and save time, pipeline FE model is often represented using shell elements. However, with advancements in computing power, there is a growing opportunity to employ solid elements to model pipelines more accurately and closely mimic real-world scenarios. By transitioning from shell to solid elements, FEM analysis can capture finer details and complexities of the pipeline's geometry and behavior, yielding results that are more representative of actual conditions. This evolution in modeling approach not only enhances the accuracy and reliability of simulations but also enables engineers to gain deeper insights into pipeline performance and behavior under various loading conditions.

7 LESSONS LEARNED

Ideally, minimizing splicing work leads to more accurate results for distributed fiber optic sensing data. The original plan was to install all the cables on the pipeline first and then bury them in the trench. However, during the pipeline replacement process, the procedures for excavating trenches, welding pipeline sections, and burying and installing pipeline segments frequently changed. Consequently, the amount of splicing work also increased. Additionally, the cable end used for reading was located on a slope, complicating the setup of the analyzer. Due to changes in the pipeline installation plan, the initially prepared fiber optic cables were not long enough to complete the installation, necessitating multiple trips back to retrieve additional cables to meet the length requirements.

During the backfilling process, the buried cable was damaged, but this issue was not observed until the entire backfilling process was completed. Consequently, considerable time was spent locating the damaged point and excavating again to fix it. To prevent such problems in future installations, it is essential to continuously monitor the cable's status throughout the construction activities rather than only checking at the end. This proactive approach would allow for the immediate detection and precise location of any damage to the fiber optic sensors, enabling quick fixes and significantly reducing the time and labor required to address the issue. Continuous monitoring during installation ensures that any damage can be identified and rectified promptly, enhancing the efficiency and reliability of the installation process.

8 REFERENCES

[1] ALA. (2005). Guidelines for the Design of Buried Steel Pipe. American Lifelines Alliance, a Partnership between FEMA and ASCE.

[2] American Society of Civil Engineers. Committee on Gas, & Liquid Fuel Lifelines. (1984). Guidelines for the Seismic Design of Oil and Gas Pipeline Systems. American Society of Civil Engineers.

[3] Audibert, J. M., & Nyman, K. J. (1977). Soil restraint against horizontal motion of pipes. Journal of the Geotechnical Engineering Division, 103(10), 1119-1142.

[4] Bao, X., & Chen, L. (2012). Recent progress in distributed fiber optic sensors. sensors, 12(7), 8601-8639.

[5] Bryden, P., El Naggar, H., & Valsangkar, A. (2015). Soil-structure interaction of very flexible pipes: Centrifuge and numerical investigations. International Journal of Geomechanics, 15(6), 04014091.

[6] Cheong, T. P., Soga, K., & Robert, D. J. (2011). 3D FE analyses of buried pipeline with elbows subjected to lateral loading. Journal of geotechnical and geoenvironmental engineering, 137(10), 939-948.

[7] Dakin, J. P., Pratt, D. J., Bibby, G. W., & Ross, J. N. (1985). Distributed optical fibre Raman temperature sensor using a semiconductor light source and detector. Electronics letters, 13(21), 569-570.

[8] Dickin, E. A. (1988, April). Stress-displacement of buried plates and pipes. In Proceedings of the International Conference on Geotechnical Centrifuge Modeling (Centrifuge 88), Paris, France (pp. 25-27).

[9] Fern, E. J., Robert, D. J., & Soga, K. (2016). Modeling the stress-dilatancy relationship of unsaturated silica sand in triaxial compression tests. Journal of Geotechnical and Geoenvironmental Engineering, 142(11), 04016055.

[10] Global Infrastructure Hub (2021). https://outlook.gihub.org/

[11] Hansen, J. B. (1961). The ultimate resistance of rigid piles against transversal forces. Bulletin 12, Danish Geotech. Institute, 1-9.

[12] Jefferies, M. G. (1993). Nor-Sand: a simle critical state model for sand. Géotechnique, 43(1), 91-103.

[13] Jefferies, M., & Been, K. (2015). Soil liquefaction: a critical state approach. CRC press.

[14] Karamitros, D. K., Bouckovalas, G. D., & Kouretzis, G. P. (2007). Stress analysis of buried steel pipelines at strike-slip fault crossings. Soil Dynamics and Earthquake Engineering, 27(3), 200-211.

[15] Kennedy, R. P., Williamson, R. A., & Chow, A. M. (1977). Fault movement effects

on buried oil pipeline. Transportation Engineering Journal of ASCE, 103(5), 617-633.

[16] Koseki, J., Matsuo, O., & Tanaka, S. (1998). Uplift of sewer pipes caused by earthquake-induced liquefaction of surrounding soil. Soils and foundations, 38(3), 75-87.

[17] Li, B., Luo, L., Yu, Y., Soga, K., & Yan, J. (2017). Dynamic strain measurement using small gain stimulated Brillouin scattering in STFT-BOTDR. IEEE Sensors Journal, 17(9), 2718-2724.

[18] Liu, M., Wang, Y. Y., & Yu, Z. (2008, July). Response of pipelines under fault crossing. In ISOPE International Ocean and Polar Engineering Conference (pp. ISOPE-I). ISOPE.

[19] Luo, L., Li, B., Yu, Y., Xu, X., Soga, K., & Yan, J. (2016). Time and frequency localized pulse shape for resolution enhancement in STFT-BOTDR. Journal of Sensors, 2016.

[20] Luo, L., Sekiya, H., & Soga, K. (2019). Dynamic distributed fiber optic strain sensing on movement detection. IEEE Sensors Journal, 19(14), 5639-5644.

[21] Marktsandmarkets (2022) https://www.marketsandmarkets.com/Market-Reports/structural-health-monitoring-market-101431220.html

[22] McKinsey Global Institute (2017). Reinventing construction: A route of higher productivity. 20pp.

[23] Newmark, N. M. (1975). Pipeline design to resist large fault displacement. In Proceedings of US national conference on earthquake engineering (pp. 416-425).

[24] Ohno, H., Naruse, H., Kihara, M., & Shimada, A. (2001). Industrial applications of the BOTDR optical fiber strain sensor. Optical fiber technology, 7(1), 45-64.

[25] O'Rourke, T. D., & Trautmann, C. H. (1980). Buried pipeline response to permanent earthquake ground movements. School of Civil and Environmental Engineering, Cornell University.

[26] O'Rourke, M. J., Liu, X., & Flores-Berrones, R. (1995). Steel pipe wrinkling due to longitudinal permanent ground deformation. Journal of transportation engineering, 121(5), 443-451.

[27] O'Rourke, M. J., & Liu, X. (1999). Response of buried pipelines subject to earthquake effects (pp. 80-81). New York: Mceer.

[28] O'Rourke, T. D., Jezerski, J. M., Olson, N. A., Bonneau, A. L., Palmer, M. C., Stewart, H. E., ... & Abdoun, T. (2008). Geotechnics of pipeline system response to earthquakes. In Geotechnical earthquake engineering and soil dynamics IV (pp. 1-38).

[29] Ovesen, N. K. (1964). Anchor slabs, calculation methods and model tests. Bulletin,

16, 39.

[30] Ravet, F., Borda, C., Rochat, E., & Niklès, M. (2013, July). Geohazard prevention and pipeline deformation monitoring using distributed optical fiber sensing. In ASME International Pipeline Geotechnical Conference (Vol. 55775, p. V001T04A001). American Society of Mechanical Engineers.

[31] Rowe, R. K., & Davis, E. H. (1982). The behaviour of anchor plates in sand. Geotechnique, 32(1), 25-41.

[32] Robert, D. J., Soga, K., & O'Rourke, T. D. (2016). Pipelines subjected to fault movement in dry and unsaturated soils. International Journal of Geomechanics, 16(5), C4016001.

[33] Robert, D. J., Soga, K., O'Rourke, T. D., & Sakanoue, T. (2016). Lateral load-displacement behavior of pipelines in unsaturated sands. Journal of Geotechnical and Geoenvironmental Engineering, 142(11), 04016060.

[34] Soga, K. (2023) "Smart Infrastructure for Smart Cities," The Bridge, National Academy of Engineering, Vol. 53, No.1, Spring 2023, pp. 22-29

[35] Soga, K., Kechavarzi, C., Pelecanos, L., de Battista, N., Williamson, M., Gue, C. Y., ... & Elshafie, M. (2017). Fiber-Optic Underground Sensor Networks: Distributed Fiber-Optic Strain Sensing for Monitoring Underground Structures-Tunnels Case Studies. In Underground Sensing: Monitoring and Hazard Detection for Environment and Infrastructure (pp. 287-321). Elsevier.

[36] Soga, K. and Schooling, J. (2016). "Infrastructure sensing," Interface focus, 6(4), p.20160023.

[37] Soga, K., & Luo, L. (2018). Distributed fiber optics sensors for civil engineering infrastructure sensing. Journal of Structural Integrity and Maintenance, 3(1), 1-21.

[38] Takada, S., Hassani, N., & Fukuda, K. (2001). A new proposal for simplified design of buried steel pipes crossing active faults. Earthquake engineering & structural dynamics, 30(8), 1243-1257.

[39] Terzaghi, K., Peck, R. B., & Mesri, G. (1996). Soil mechanics in engineering practice. John wiley & sons.

[40] Trautmann, C. H. (1983). Behavior of pipe in dry sand under lateral and uplift loading. Cornell University.

[41] Trautmann, C. H., & O'Rourke, T. D. (1985). Lateral force-displacement response of buried pipe. Journal of Geotechnical Engineering, 111(9), 1077-1092.

[42] Trifonov, O. V., & Cherniy, V. P. (2010). A semi-analytical approach to a nonlinear stress–strain analysis of buried steel pipelines crossing active faults. Soil Dynamics and Earthquake Engineering, 30(11), 1298-1308.

[43] Trifonov, O. V., & Cherniy, V. P. (2012). Elastoplastic stress–strain analysis of

buried steel pipelines subjected to fault displacements with account for service loads. Soil Dynamics and Earthquake Engineering, 33(1), 54-62.

[44] Yimsiri, S., Soga, K., Yoshizaki, K., Dasari, G. R., & O'Rourke, T. D. (2004). Lateral and upward soil-pipeline interactions in sand for deep embedment conditions. Journal of geotechnical and geoenvironmental engineering, 130(8), 830-842.

[45] Yu, Y., Luo, L., Li, B., Soga, K., & Yan, J. (2016). Frequency resolution quantification of Brillouin-distributed optical fiber sensors. IEEE Photonics Technology Letters, 28(21), 2367-2370.

[46] Yu, Y., Luo, L., Li, B., Soga, K., & Yan, J. (2017). Quadratic time-frequency transforms-based Brillouin optical time-domain reflectometry. IEEE Sensors Journal, 17(20), 6622-6626.

[47] Vazouras, P., Karamanos, S. A., & Dakoulas, P. (2010). Finite element analysis of buried steel pipelines under strike-slip fault displacements. Soil Dynamics and Earthquake Engineering, 30(11), 1361-1376.

[48] Vazouras, P., Karamanos, S. A., & Dakoulas, P. (2012). Mechanical behavior of buried steel pipes crossing active strike-slip faults. Soil Dynamics and Earthquake Engineering, 41, 164-180.

[49] Vazouras, P., Dakoulas, P., & Karamanos, S. A. (2015). Pipe–soil interaction and pipeline performance under strike–slip fault movements. Soil Dynamics and Earthquake Engineering, 72, 48-65.

[50] Wham, B. P., Argyrou, C., O'Rourke, T. D., Stewart, H. E., & Bond, T. K. (2017). PVCO pipeline performance under large ground deformation. Journal of Pressure Vessel Technology, 139(1), 011702.

[51] Wham, B. P., Berger, B. A., O'Rourke, T. D., Pariya-Ekkasut, C., & Stewart, H. E. (2017). Performance evaluation of Bionax SR PVCO pipeline with extended bell joints under earthquake-induced ground deformation. Geotechnical Lifelines Large-Scale Testing Facility. https://lifelines. cee. cornell. edu/projects/Last accessed September, 18, 2018.

[52] Zhang, Z., & Bao, X. (2008). Distributed optical fiber vibration sensor based on spectrum analysis of Polarization-OTDR system. Optics express, 16(14), 10240-10247.